EFFECTS OF CaO AND ZrO_2 ADDITION ON METHANE STEAM–REFORMING OF Ni/Al_2O_3 CATALYST

Mr. Kowit Lertwittayanon

A Dissertation Submitted in Partial Fulfillment of the Requirements
for the Degree of Doctor of Philosophy Program in Materials Science
Department of Materials Science
Faculty of Science
Chulalongkorn University
Academic Year 2010

ผลของการเติมแคลเซียและเซอร์โคเนียต่อการรีฟอร์มมีเทนด้วยไอน้ำของตัวเร่งปฏิกิริยานิกเกิล/อะลูมินา

นายโกวิท เลิศวิทยานนท์

วิทยานิพนธ์นี้เป็นส่วนหนึ่งของการศึกษาตามหลักสูตรปริญญาวิทยาศาสตรดุษฎีบัณฑิต
สาขาวิชาวัสดุศาสตร์ ภาควิชาวัสดุศาสตร์
คณะวิทยาศาสตร์ จุฬาลงกรณ์มหาวิทยาลัย
ปีการศึกษา 2553

Thesis Title	Effects of CaO and ZrO_2 addition on methane steam–reforming of Ni/Al_2O_3 catalyst
By	Mr. Kowit Lertwittayanon
Field of Study	Materials Science
Thesis Advisor	Assistant Professor Thanakorn Wasanapiarnpong, D.Eng.
Thesis Co-advisor	Duangduen Atong, Ph.D.
Thesis Co-advisor	Assistant Professor Viboon Sricharoenchaikul, Ph.D.

Accepted by the Faculty of Science, Chulalongkorn University in Partial Fulfillment of the Requirements for the Doctoral Degree

……...Dean of the Faculty of Science
(Professor Supot Hannongbua, Dr.rer.nat.)

THESIS COMMITTEE

……... Chairman
(Assistant Professor Sirithan Jiemsirilers, Ph.D.)

…… Thesis Advisor
(Assistant Professor Thanakorn Wasanapiarnpong, D.Eng.)

……. Thesis Co-advisor
(Duangduen Atong, Ph.D.)

……. Thesis Co-advisor
(Assistant Professor Viboon Sricharoenchaikul, Ph.D.)

……. Examiner
(Rojana Pornprasertsuk, Ph.D.)

……. External Examiner

(Professor Shigetaka Wada, Dr.Eng.)

……. External Examiner
(Pavadee Aungkavattana, Ph.D.)

โกวิท เลิศวิทยานนท์ : ผลของการเติมแคลเซียและเซอร์โคเนียต่อการรีฟอร์มมีเทนด้วยไอน้ำของตัวเร่งปฏิกิริยานิกเกิล/อะลูมินา. (EFFECTS OF CaO AND ZrO_2 ADDITION ON METHANE STEAM–REFORMING OF Ni/Al_2O_3 CATALYST) อ. ที่ปรึกษาวิทยานิพนธ์หลัก : ผศ.ดร. ธนากร วาสนาเพียรพงศ์, อ. ที่ปรึกษาวิทยานิพนธ์ร่วม : ดร. ดวงเดือน อาจองค์ และ ผศ.ดร. วิบูลย์ ศรีเจริญชัยกุล, 92 หน้า.

การรีฟอร์มมีเทนด้วยไอน้ำเป็นกระบวนการที่ถูกใช้อย่างกว้างขวางในอุตสาหกรรมสำหรับการผลิตไฮโดรเจน ตัวเร่งปฏิกิริยานิกเกิลมักถูกใช้ในกระบวนการรีฟอร์มมีเทนด้วยไอน้ำเพราะมีราคาถูกและความว่องไวของการเกิดปฏิกิริยา อย่างไรก็ตามตัวเร่งปฏิกิริยาจากนิกเกิลมีปัญหาจากการเสื่อมอย่างรวดเร็วเนื่องจากการสะสมของคาร์บอน ดังนั้นงานวิจัยนี้จึงมีวัตถุประสงค์เพื่อปรับปรุงความคงทนของตัวเร่งปฏิกิริยานิกเกิล การเติมตัวเสริม $CaO–ZrO_2$ ในตัวเร่งปฏิกิริยานิกเกิล/อะลูมินาอาจช่วยปรับปรุงความคงทนของตัวเร่งปฏิกิริยานิกเกิลได้ การศึกษานี้ได้ถูกแบ่งออกเป็น 3 ส่วนหลัก

ส่วนที่หนึ่งเป็นการศึกษาผลกระทบของอัตราส่วนโมล $CaO–ZrO_2$ (0, 0.2, 0.35, 0.45, และ 0.55) ที่มีต่อประสิทธิภาพของตัวเร่งปฏิกิริยานิกเกิล/แกมมาอะลูมินาซึ่งถูกเตรียมโดยวิธีซีเควนเชียลอิมเพรกเนชั่น ตัวเร่งปฏิกิริยาที่มี $CaO–ZrO_2$ ที่อัตราส่วนโมล 0.5 ให้ปริมาณไฮโดรเจนสูงที่สุด (H_2 yield) แม้ว่าจะมีคาร์บอนถูกสะสมอยู่บ้าง ผลลัพธ์นี้ถูกอ้างถึงอัตราส่วนโมลที่เหมาะสมซึ่งทำให้มี $CaZrO_3$ ฟอร์มตัวขึ้นมาและการฟอร์มตัวของที่ว่างของอะตอมออกซิเจนในเวลาต่อมา ตำแหน่งที่ว่างของอะตอมออกซิเจนนั้นดูดซับโมเลกุลน้ำอย่างมากซึ่งสนับสนุนให้เกิดปฏิกิริยาการทำให้คาร์บอนเป็นแก๊สและปฏิกิริยาวอเตอร์แก๊สชิฟในเวลาต่อมา

ส่วนที่สองเป็นการศึกษาวิธีเตรียมตัวเร่งปฏิกิริยานิกเกิล/แกมมาอะลูมินาซึ่งมีอัตราส่วนโมลของ CaO/ZrO_2 ที่ 0.5 โดยวิธีโคอิมเพรกเนชั่นและวิธีซีเควนเชียลอิมเพรกเนชัน ความว่องไวของการเกิดปฏิกิริยาของตัวเร่งปฏิกิริยาที่ถูกเตรียมโดยวิธีโคอิมเพรกเนชั่นมีค่าสูงและสม่ำเสมอมากกว่าวิธีซีเควนเชียลอิมเพรกเนชั่น อย่างไรก็ตามที่เวลา 30 ชั่วโมง ความว่องไวของการเกิดปฏิกิริยาของตัวเร่งปฏิกิริยาที่ถูกเตรียมโดยวิธีโคอิมเพรกเนชั่นลดลงอย่างมากเนื่องจากการปกคลุมผิวหน้าของคาร์บอน ผลลัพธ์นี้ถูกอ้างไปยังวิธีการเตรียมที่แตกต่างกันซึ่งเป็นสาเหตุให้เกิดความแตกต่างอย่างมากในสมบัติทางกายภาพและเคมีและนำไปสู่ความแตกต่างในความว่องไวของการเกิดปฏิกิริยา

ส่วนสุดท้ายเป็นการศึกษาตัวเร่งปฏิกิริยานิกเกิลที่ถูกปรับสภาพด้วย $CaO–ZrO_2$ โดยวิธีซีเควนเชียลอิมเพรกเนชั่นซึ่งใช้แอลฟาอะลูมินาเป็นตัวรองรับ เปอร์เซ็นต์น้ำหนักของ $CaO–ZrO_2$ ซึ่งมีค่าอัตราส่วนโมลคงที่ที่ 0.5 ถูกศึกษาจาก 0 ถึง 15% โดยน้ำหนัก การเติม $CaO–ZrO_2$ ที่ 15% ให้ปริมาณไฮโดรเจนสูงที่สุดและจำนวนของคาร์บอนที่ถูกสะสมเพียงเล็กน้อย ผลลัพธ์นี้ถูกอ้างไปยังจำนวนที่เหมาะสมของอนุภาค $CaZrO_3$ ที่ฟอร์มตัวขึ้นมาในขนาดของนาโนเมตรซึ่งเป็นสาเหตุให้เกิดสภาวะที่เหมาะสมสำหรับการเกิดปฏิกิริยาการรีฟอร์มมีเทนด้วยไอน้ำ

ภาควิชา วัสดุศาสตร์ ลายมือชื่อนิสิต .....

สาขาวิชา วัสดุศาสตร์ ลายมือชื่อ อ.ที่ปรึกษาวิทยานิพนธ์หลัก .....

ปีการศึกษา 2553 ลายมือชื่อ อ.ที่ปรึกษาวิทยานิพนธ์ร่วม .....

ลายมือชื่อ อ.ที่ปรึกษาวิทยานิพนธ์ร่วม .....

4973893023 : MAJOR MATERIALS SCIENCE
KEYWORDS : HYDROGEN PRODUCTION / STEAM REFORMING / NICKEL CATALYST / PEROVSKITE STRUCTURE / OXYGEN VACANCIES

KOWIT LERTWITTAYANON : EFFECTS OF CaO AND ZrO_2 ADDITION ON METHANE STEAM–REFORMING OF Ni/Al_2O_3 CATALYST. ADVISOR : ASST.PROF. THANAKORN WASANAPIARNPONG, D.Eng. CO-ADVISOR : DUANGDUEN ATONG, Ph.D., ASST.PROF. VIBOON SRICHAROENCHAIKUL, Ph.D., 92 pp.

Steam methane reforming (SMR) is a process widely used in industrial scale for H_2 production. Ni-based catalysts are generally used in SMR process since they offer low cost and high catalytic activity. However, Ni-based catalysts suffer from rapid deactivation resulting from carbon deposition. This research work focuses on the improvement to the stability of Ni catalysts. The addition of CaO–ZrO_2 promoter into Ni/Al_2O_3 catalyst was expected to improve its stability. This work is divided into three main parts.

First, effects of CaO to ZrO_2 mole ratios (0, 0.2, 0.35, 0.45, and 0.55) on the performance of Ni/γ-Al_2O_3 catalyst prepared by sequential impregnation are investigated. Ni/γ-Al_2O_3 catalyst containing CaO–ZrO_2 at 0.55 mole ratio provided the highest H_2 yield; however, it showed some amount of deposited carbon. The results were attributed to the appropriate mole ratio leading the formation of $CaZrO_3$ and then oxygen vacancies. The oxygen vacancies preferred to adsorb water molecules facilitating the reactions of carbon gasification and then water gas shift (WGSR).

Secondly, preparation methods between co-impregnation and sequential impregnation of Ni/γ-Al_2O_3 catalyst at the appropriate mole ratio (0.55) are examined. The activity of co-impregnation–prepared catalyst was higher and more consistent than that of sequential impregnation–prepared catalyst. Nevertheless, at time on stream of 30 h the activity of co-impregnation–prepared catalyst significantly dropped due to the formation of encapsulating carbon. The results were attributed to the different preparation methods leading to their significant difference in physico-chemical properties and then catalytic activity.

Finally, α-Al_2O_3 was used as supporter for preparing the (CaO–ZrO_2)-modified Ni catalyst through sequential impregnation. Loading percentage of CaO-ZrO_2 fixed at 0.5 mole ratio of CaO/ZrO_2 was varied from 0 to 15 wt%. The addition of CaO–ZrO_2 at 15 wt% indicated the highest H_2 yield and the small amount of deposited carbon. The results were attributed to the appropriate amount of formed $CaZrO_3$ nanoparticles leading to the favorable conditions for SMR reactions.

Department : Materials Science Student's Signature .....

Field of Study : Materials Science Advisor's Signature .....

Academic Year : 2010 Co-advisor's Signature .....

Co-advisor's Signature .....

ACKNOWLEDGEMENTS

I would like to express my deep and sincere gratitude to Dr. Pavadee Aungkavattana, a researcher at National Metal and Materials Technology Center (MTEC), for her understanding, and financial support obtained from her research project (Development of honeycomb ceramic catalyst for practical fuels for SOFC applications). I would like to extend my gratitude to my advisor, Assistant Prof. Dr. Thanakorn Wasanapiarnpong, and my co-advisor, Dr. Duangduen Atong and Assistant Prof. Dr. Viboon Sricharoenchaikul, for their good advices and any help to me

I must extend special gratitude to Professor Dr. Shigetaka Wada for his worthy discussion on the first part of my dissertation.

I specially thank Assistant Prof. Dr. Viboon Sricharoenchaikul for his help with setting up steam methane reforming system.

I also thank to all of staff at MTEC for every good wish, professional advice, and full support, especially for Ms. Sildara Thassanaprichayanont and Ms. Khanthima Hemra (Applied Ceramics Lab), Ms. Suphakan Kijamnajsuk and Mr. Narin Jantaping (XRD lab), Mr. Visittapong Yordsri (TEM lab), Mr. Narin Sirinantawittaya (BET lab), and Ms. Utaiwan Watcharosin (TGA lab).

I owe a debt of gratitude to Thailand Graduate Institute Science and Technology (TGIST) for financial support and MTEC for research facilities. I would like to thank Research Unit of Advanced Ceramics and Polymeric Materials, National Center of Excellence for Petroleum, Petrochemical and Advanced Material, Asian Development Bank (ADB) for financial support. Finally, I would like to express my gratitude to my family for their love, understanding and encouragement.

CONTENTS

Page

Page

Page

LIST OF TABLES

Page

LIST OF FIGURES

Page

Page

Page

Page

CHAPTER I

INTRODUCTION

At present, Ni/Al_2O_3 catalyst is widely used in industrial for H_2 production via steam reforming of methane (SMR). Nickel is the most possible metal due to its high activity and low cost compared to noble metals having high activity but high cost. For the systems of reforming, SMR offers high hydrogen concentration (70–80%) compared to partial oxidation and auto-thermal reforming (40–50%) on a dry basis. However, there are still a certain challenges for this system, such as the improvement of reforming efficiency and the production of more durable catalyst. Therefore, this research focuses on the improvement of catalyst stability while the activity is still high. In order to improve either activity/selectivity or stability, promoters are usually added to the catalyst in small amount. From literature reviews, we found that CaO and ZrO_2 are interesting promoters because with an appropriate amount, they can improve both activity and stability of Ni/Al_2O_3 catalyst in SMR. The synergy effect of CaO–ZrO_2 composite is possible to make $Ni/CaO–ZrO_2/Al_2O_3$ catalyst with high performance in steam methane reforming. The appropriate composition and preparation of CaO with ZrO_2 in $Ni/CaO–ZrO_2/Al_2O_3$ catalyst likely provide good surface structure and properties for catalytic activity in steam methane reforming.

The assumption about improving the catalytic performance of Ni/Al_2O_3 catalyst is concerned with adding CaO-ZrO_2 as promoter into the catalyst in order to obtain appropriate surface structure and excellent properties for steam methane reforming. An interaction between CaO and ZrO_2 is likely to make the synergetic effect of CaO–ZrO_2 composite. Due to the low acidity and high thermal stability of

CaO with the capability of oxidizing deposited carbon of ZrO_2 in steam reforming, their synergy effect might improve the catalyst performance [1–4]. The composite is expected to enhance the dispersion of Ni active phase and the metal-support interaction, etc. In addition, this work will also study the effect of catalyst preparation process which influences the surface structure of catalyst, on the catalytic performance because they.

The objectives of this research are as follows:

1. Establish a SMR system

2. Develop a catalyst which has both high activity and stability in the SMR process.

This work firstly focused on improving the stability of the nickel catalysts in SMR by the coke gasification, we prepared and characterized nickel catalyst supported on γ-Al_2O_3 modified by CaO-ZrO_2. CaO and ZrO_2 were used as promoter; therefore, the total amount of CaO-ZrO_2 in the nickel catalyst was to only 5% by weight. γ-Al_2O_3 was used as support to obtain the Ni catalysts with high specific surface area. The effects of γ-Al_2O_3 support modified by different molar ratios of CaO/ZrO_2 on catalytic activity and stability of the Ni catalysts were studied. The Ni/CaO-ZrO_2/γ-Al_2O_3 catalysts were prepared by sequential impregnation method and tested in the SMR system at steam/carbon ratio (S/C ratio) of 1 and reaction temperature of 600°C.

Secondly, the variation of CaO/ZrO_2 mole ratios between 0 and 0.55 in the modified Ni catalysts has various effects on the activity and stability of the modified Ni catalysts. The Ni catalyst modified with CaO-ZrO_2 at 0.55 mole ratio of CaO/ZrO_2 provided the highest H_2 yield, although it showed some amount of deposited carbon

filaments. Since the modified Ni catalyst with the optimum mole ratio of CaO/ZrO_2 prepared by sequential impregnation offers the promising results. It is noteworthy for comparing the effects of impregnation methods between co-impregnation and sequential impregnation on the performance of prepared catalysts, because the co-impregnation method is easier for the Ni catalysts preparation than the sequential-impregnation method.

Finally, since the $Ni/CaO–ZrO_2/\gamma\text{-}Al_2O_3$ catalysts prepared from our previous works did not clearly show the higher activity and stability than the unmodified Ni catalyst ($Ni/\gamma\text{-}Al_2O_3$), we used $\alpha\text{-}Al_2O_3$ as a supporter instead of $\gamma\text{-}Al_2O_3$. It is well known that $\alpha\text{-}Al_2O_3$ has not only high mechanical stability but also high thermal resistance [5]. As a result, the use of $\alpha\text{-}Al_2O_3$ as supporter of Ni catalysts is considered to be suitable for industrial SMR process since it offers (1) high attrition resistance and (2) no phase transformation during SMR at high temperature for a long time. Since $\alpha\text{-}Al_2O_3$ has low surface area ($\sim < 10$ m^2/g) [6,7], variation in loading percentage of $CaO–ZrO_2$ in $Ni/CaO–ZrO_2/\alpha\text{-}Al_2O_3$ catalysts might affect its performance in SMR.

CHAPTER II

BACKGROUND

H_2 production by SMR is an interdisciplinary research. Only the key areas are briefly explained.

2.1 Steam methane reforming

The steam reforming of methane (SMR) consists of two reversible reactions as shown in Eqs. 2.1 and 2.2.

Reforming reaction:

$$CH_4 + H_2O \leftrightarrow CO + 3H_2 \qquad \Delta H^o_{298} = +206 \text{ kJ/mol} \qquad (2.1)$$

Water Gas Shift Reaction (WGSR):

$$CO + H_2O \leftrightarrow CO_2 + H_2 \qquad \Delta H^o_{298} = -41 \text{ kJ/mol} \qquad (2.2)$$

Eq. 2.1 is the strongly endothermic reaction and Eq. 2.2 is moderately exothermic reaction. Due to its endothermic character, reforming is favored at high temperatures. Also, because reforming is accompanied by a volume expansion, it is favored at low pressures as shown in Fig. 2.1 [1]. In contrast, the exothermic shift reaction is favored at low temperatures, while unaffected by changes in pressure.

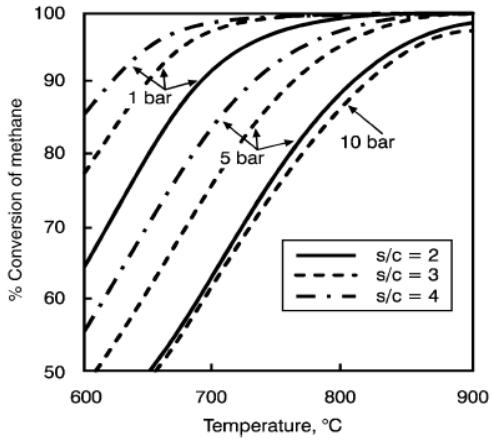

Fig. 2.1 – Equilibrium conversion against temperature, pressure and steam/carbon ratio in steam reforming of methane

The reaction rate for the disappearance of methane can be written as the following equation.

$$r_{CH_4} = \frac{X_{CH_4}}{W_{cat} / F_{CH\,4}} \qquad (2.3)$$

r = Reaction rate (mol/g_{cat} – h)

X = Conversion

W/F = Ratio of catalyst weight (g) and gas flow (mol/h)

Water gas shift reaction can occur very fast under the reforming conditions. As a result, the water gas shift equilibrium is always established during steam reforming. Steam methane reforming generally involves two catalytic functions: (1) a metal surface for dissociated adsorption of methane and (2) an oxide sites for dissociated adsorption of water. Oxide sites are generally located on the surface of a promoter or support, the latter of which also serves to maintain the stability of the well-dispersed metallic phase. Because of the severe, high-temperature reaction conditions in the steam reforming, catalyst for this process must exhibit high thermal

stability. In addition, because of the tendency towards deactivation by coke and carbon deposition, promoters and supports are needed for the enhancement of carbon gasification by steam. This requires careful selection of the metal, promoter and support functions.

SMR over supported nickel catalysts with various promoters has been provided by many researchers [2–4]. For example, alkaline earth oxides were added to reduce carbon deposition [4–5]. Effect of supports such as silica, alumina, and zirconia for nickel catalysts have been studied in steam methane reforming at low temperatures of 500 ^{o}C compared to the usual conditions of above 700 ^{o}C. Decomposition of methane on the nickel surface is believed to be the first step of the SMR process. The carbon species formed on the surface subsequently react with steam or surface oxygen species. It was shown that zirconium oxide, which can absorb water at 500 ^{o}C, is an effective support and its surface hydroxyl groups contribute significantly to the steam reforming at 500 ^{o}C [6].

The choice of catalyst support in the steam reforming is critical to its survival. Thermally stable supports of low acidity are needed to prevent deactivation by sintering and carbon deposition. The order of decreasing acidity of supports is as shown [6].

SiO_2-Al_2O_3 > SiO_2-MgO > SiO_2 > α-Al_2O_3 > TiO_2 > ZrO_2 > $MgAl_2O_4$ > CaO, MgO

Therefore, CaO, MgO, and $MgAl_2O_4$ are the most desirable supports to prevent carbon formation. The order of decreasing thermal stability of support is as shown [6].

$$ZrO_2 > MgO > CaO > BaO > Al_2O_3 > Cr_2O_3 > WO_2$$

Thus, ZrO_2, MgO, and CaO are among the most thermally stable supports; α-Al_2O_3 (not listed above) is also a highly thermally-stable support and finds application in the steam methane reforming. The support itself may also actively participate in the catalytic reaction. This can be achieved with so-called oxy-transporters, such as ZrO_2 or CeO_2, which are capable of oxidizing deposited carbon. Supports with a basic nature, such as MgO, are known to enhance the activity of steam (i.e., dissociation into reactive OH and H species) as shown in Fig. 2.2 [12].

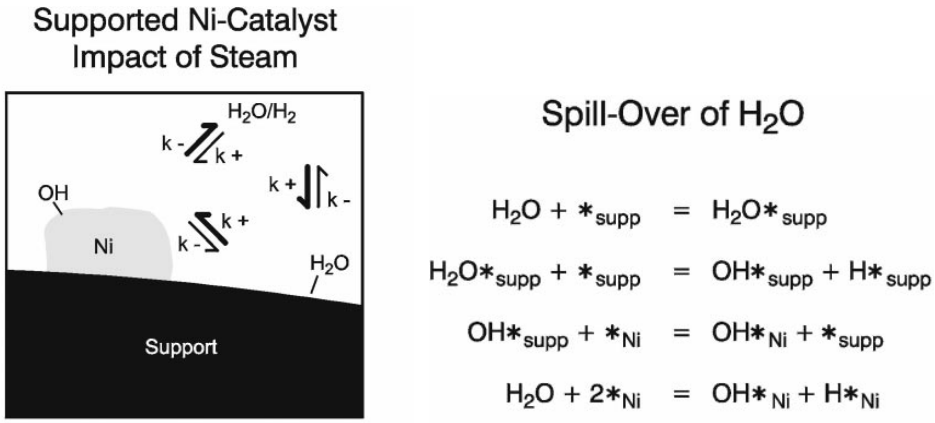

Fig. 2.2 – Spill–over of steam [12]

Fundamental studies suggest that there is a critical crystallite size for optimum performance, thus the steam reforming is apparently a structure-sensitive reaction. Steam reforming catalysts are typically formed into relatively large, dense rings, grooved cylinders, and holed cylinders. The shape and structure are designed for low-pressure drop, minimum pore diffuse limitations, and good thermal conductivity since heat transfer is critical. Table 2.1 lists compositions of some typical industrial steam-reforming nickel-containing catalysts [6].

Table 2.1 – Typical commercial steam-reforming catalysts [6]

Catalyst	Composition (wt%)[b]	Particle form/Size (mm)[c]	Bulk density (g/cm^3)	Operating temperature (^oC)
JM Katalco 23-4	17%Ni/α-Al_2O_3	10-16 x 13-20, 4-hole quadrulobe	1.1-1.2	< 850
JM Katalco 57-4	18%Ni/$CaAl_2O_4$	11-19 x 15-20, 4-hole quadrulobe	0.99	< 1,000
SC G 56	15–25% Ni/$CaAl_2O_4$	Ring, 16/6 x 16mm	0.83	600–870
TopsØe R-67-7H	12–15% Ni/$MgAl_2O_4$	16 x 11 x 3.4 to 20 x 18 x 3.4, 7-hole tablet	1.06	700–870

[a] JM = Johnson Matthey, SC = Süd Chemie Group, TopsØe = Haldor TopsØe A/S.

[b] Percentage of NiO before reduction.

[c] Ring dimensions refer to outer diameter/inner diameter x length

2.2 Catalyst deactivation in steam reforming

Carbon and coke depositions require a special attention in the steam reforming process since it leads to the deactivation and even disintegration of the catalyst. Three reactions are considered as potential sources of the deposition as shown in Eqs. 2.4–2.6:

Methane cracking: $CH_4 \leftrightarrow C + 2H_2$ (2.4)

Boudouard reaction: $2CO \leftrightarrow C + CO_2$ (2.5)

CO-reduction: $CO + H_2 \leftrightarrow C + H_2O$ (2.6)

Carbon is a product of the disproportionation of carbon monoxide into carbon dioxide and graphite as shown in Boudouard reaction, while coke is produced by decomposition or condensation of hydrocarbons on catalyst surfaces and typically consists of polymerizes heavy hydrocarbons [6].

Deposition of carbon and/or coke on a steam reforming catalyst can lead to catastrophically high rates of catalyst deactivation due to poisoning/fouling of the surface with carbonaceous species, plugging of catalyst pores, and pellet destruction. Three types of carbon have been observed in a reformer: pyrolytic, encapsulating and whisker as imaged by TEM in Fig. 2.3 [13].

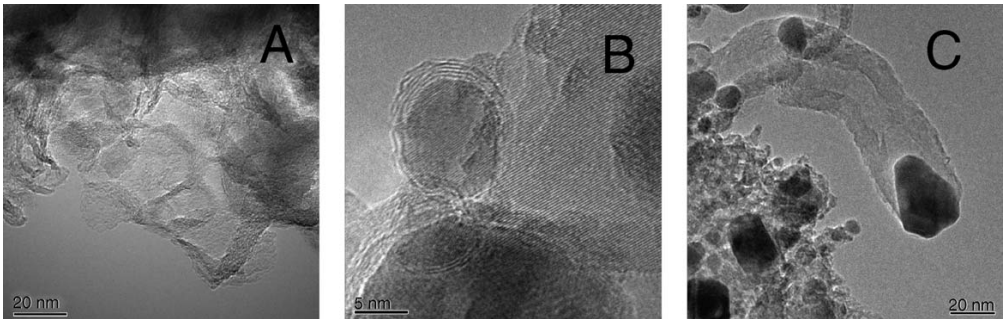

Fig. 2.3 – Electron microscopy images of pyrolytic carbon on a $MgAl_2O_4$ carrier (A), encapsulating carbon (B), and whisker carbon (C) on $Ni/MgAl_2O_4$ catalysts [13]

Pyrolytic carbon (Fig. 2.3A) is formed by the exposure of heavy hydrocarbons to high temperatures. High temperatures in the reformers may exist as a result of low activity of higher hydrocarbons for example due to sulfur poisoning or sintering of the catalyst in the colder upper parts of the reactor tubes.

Encapsulating carbon (gum) (Fig. 2.3B) consists of a thin CH_x film or a few layers of graphite covering the nickel particles. This results in the loss of activity and deactivation of the catalyst bed. The rate of gum formation is increased with

decreasing temperatures and higher final boiling point of the hydrocarbon mixture. Deactivation of a prereformer due to gum is observed as a drift of the temperature profile in the catalyst bed with no increase in the pressure drop.

Carbon whiskers, fibers, or nanotubes are the most common carbon forms observed in steam reforming. These filamenteous carbons are grown by the reaction of hydrocarbons or CO at one side of the nickel particle and nucleation of graphitic carbon as a carbon whisker on the other sides of the nickel particle, as shown in Fig. 2.3C. Although filamenteous carbon does not poison the nickel surface, it causes activity loss from plugging catalyst pores and ultimately at high level, disintegration of catalyst pellets. In those regions of the catalyst bed where pores have been plugged, the loss of catalytic activity leads to hot spots because the desired endothermic reaction (Eq. 2.1) is no longer cooling that portion of the tube. This process is self-accelerating, since rates of carbon deposition are higher in the regions of higher temperature. When the outside of tubes reach temperature sufficiently high to cause metallurgical failure, the reactor shutdown is necessary. As carbon builds up to sufficiently high level, fines formed from the pellet disintegration cause the plugging of the reactor voids and increasing the pressure drop. Again, when the pressure drop reaches uneconomic levels, the reactor must be shutdown. Nickel-catalyzed formation of carbon filaments in steam reforming is favored at high reaction temperatures and at low S/C ratios.

2.3 Surface science and mechanisms in steam methane reforming

Catalytic reactions could formally be divided into four classes as shown in Fig. 2.4 [14].

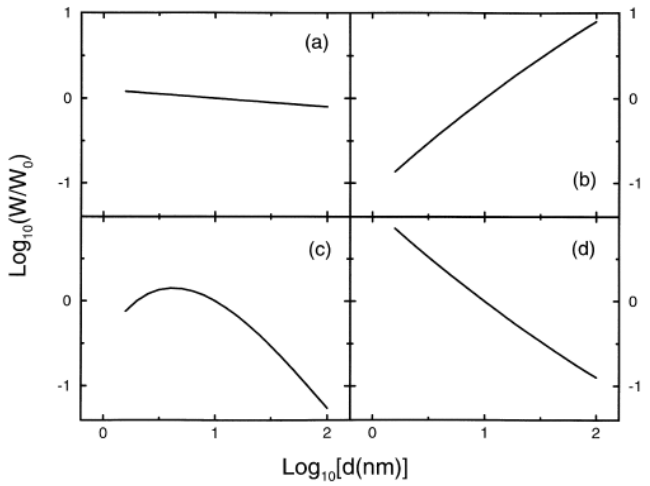

Fig. 2.4 – Typical dependencies of the reaction turnover rates *(W)* on the particle size *(d)*, W_o is the turnover rate at d = 10 nm

The turnover rates of structure-insensitive reaction (Fig. 2.4a) are nearly independent of the particle size – *(d)* (within a factor of 2). Such reaction can however be considered as exceptions at d ≤ 10nm. As a rule, catalytic reactions are structure-sensitive on this scale. In the latter case, the turnover rates may be increased (Fig. 2.4b), passed through a maximum (Fig. 2.4c), or decreased (Fig. 2.4d) with increasing particle size.

Since 1990, extensive fundamental mechanistic and kinetic studies of SMR and CO_2/dry methane reforming (CMR/DMR) have produced new reaction models that combine important features of steam and CO_2 reforming of methane. For example, a microkinetic model proposed by Aparicio [6] incorporates a 13-step sequence. The elementary steps in microkinetic model of SMR/CMR are shown below.

1. $CH_4 + 2^* \leftrightarrow {}^*CH_3 + {}^*H$
2. ${}^*CH_3 + {}^* \leftrightarrow {}^*CH_2 + {}^*H$

3. $*CH_2 + * \leftrightarrow *CH + *H$

4. $*CH + * \leftrightarrow *C + *H$

5. $H_2O + * \leftrightarrow *H_2O$

6. $*H_2O + * \leftrightarrow *OH + *H$

7. $*C + *OH \leftrightarrow **CHO$

8. $CO_2 + 2* \leftrightarrow **CO_2$

9. $**CO_2 + *H \leftrightarrow **COOH + *$

10. $**COOH + *H + 2* \leftrightarrow **CHO + *OH + 2*$

11. $**CHO + 3* \leftrightarrow **CO + *H + 2*$

12. $**CO \leftrightarrow CO + 2*$

13. $2*H \leftrightarrow H_2 + 2*$

There are, however, some aspects of the Aparicio model that must be questioned. In fact, these assumptions and predictions may be contradicted to recently observed facts that support a much simpler reaction mechanisms.

CHAPTER III

EXPERIMENTAL SECTION

3.1 Steam methane reforming system

The diagram of methane–steam reforming system is shown in Fig. 3.1.

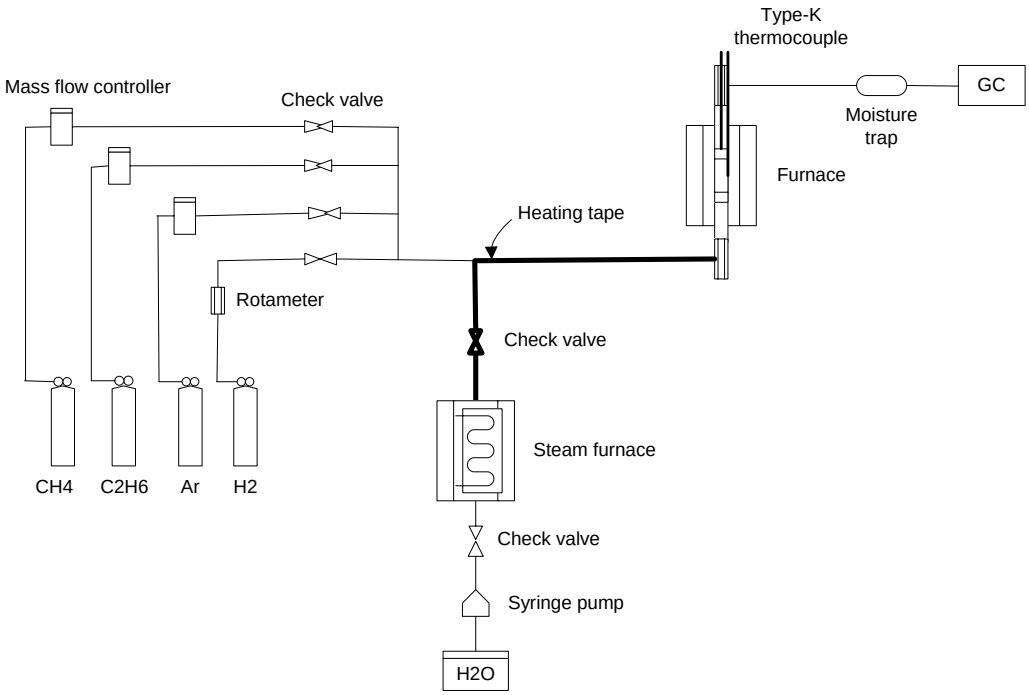

Fig. 3.1 – The diagram of steam methane reforming system

The actual system of steam methane reforming process is shown in Fig. 3.2

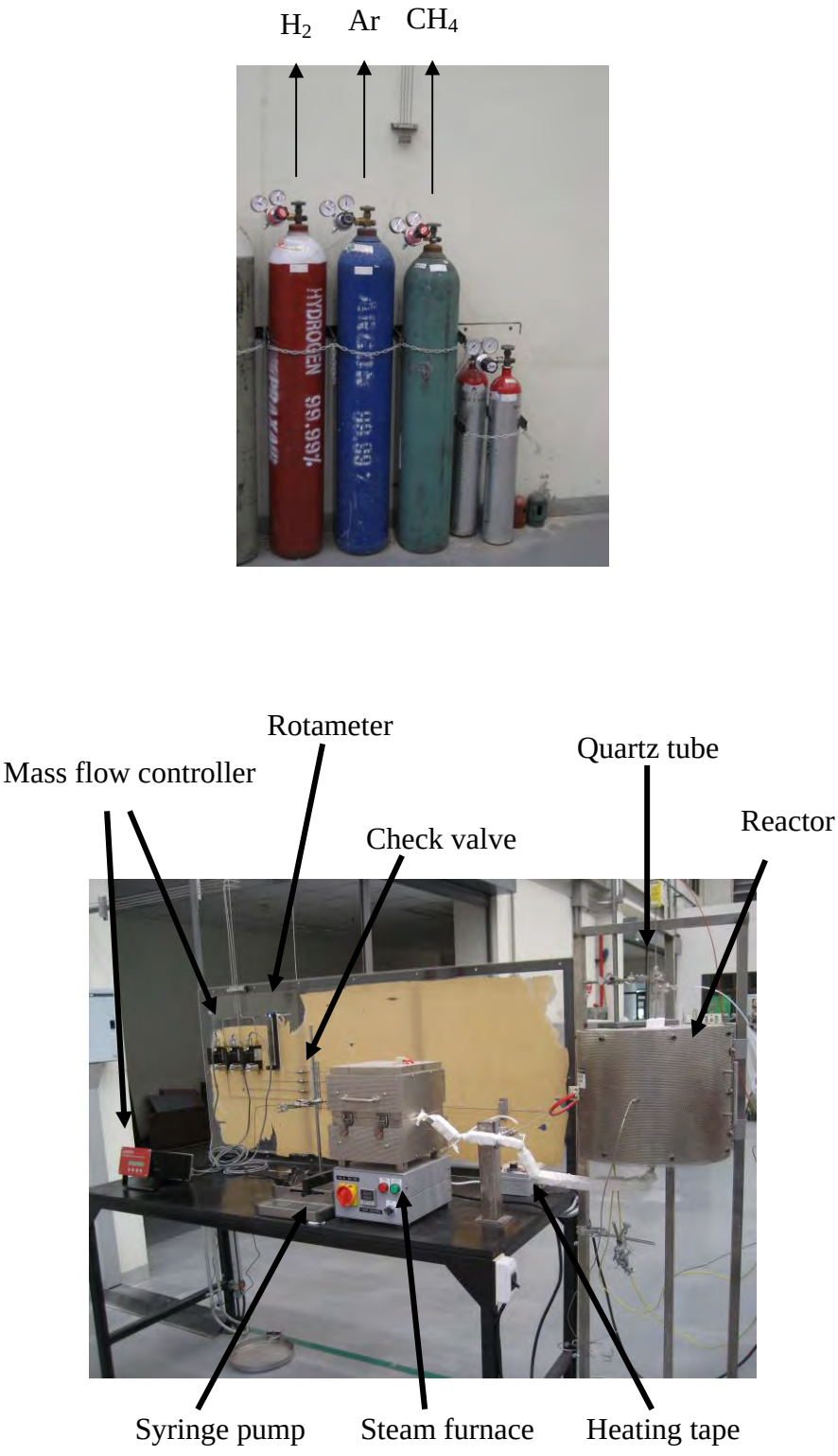

Fig. 3.2 – The actual system of methane–steam reforming

3.2 Experimental procedure for variation in the mole ratios of $CaO–ZrO_2$

3.2.1 Preparation of Ni/CaO-ZrO_2/γ-Al_2O_3 catalysts

Nickel catalysts supported on (CaO-ZrO_2)-modified γ-Al_2O_3 were prepared by the sequential impregnation method. γ-Al_2O_3 powder (132 m^2/g, Merck) was used as the support. γ-Al_2O_3 was first impregnated with the mixed solution of $Ca(NO_3)_2 \cdot 4H_2O$ (Sigma-Aldrich) and $ZrO(NO_3)_2 \cdot xH_2O$ (Sigma-Aldrich) at CaO/ZrO_2 mole ratios of 0, 0.20, 0.35, 0.45 and 0.55 before drying overnight in air at 90 °C. The dried powder was calcined at 500 °C for 1 h to modify γ-Al_2O_3 surface by ZrO_2 and CaO-ZrO_2 phases. The modified powder was then secondly impregnated with the solution of $Ni(NO_3)_2 \cdot 6H_2O$ (Merck) before drying overnight in air at 90 °C. The dried powder was finally calcined at 600 °C for 1 h to obtain the deposition of NiO on the modified γ-Al_2O_3.

All the modified Ni catalysts were prepared with a load of 10wt% nickel and 5wt% CaO-ZrO_2. The 10wt% nickel with the (CaO-ZrO_2)-modified γ-Al_2O_3 at CaO/ZrO_2 mole ratios of 0, 0.20, 0.35, 0.45 and 0.55 were referred to as NZA, N20CZA, N35CZA, N45CZA and N55CZA, respectively. The unmodified catalyst, 10%Ni/γ-Al_2O_3 was also prepared by the impregnation method for comparison to the modified Ni catalysts and referred to as NA.

3.2.2 Catalyst characterization

The chemical compositions of the prepared catalysts were determined by inductively-couple plasma mass spectrometry (ICP-OES, Perkin Elmer, PLASMA-

1000). The specific surface area and average pore diameters were examined by N_2 adsorption/desorption isotherms at liquid nitrogen temperature using Quantachrome Autosorb-1C instrument. The crystalline phases were identified by JEOL: TDX-3530 operated at 30KV and 40mA, employing Cu Kα (λ1 = 1.5405 nm). Temperature-programmed reduction (TPR) experiments were performed in a quartz tube reactor heated by an electric furnace with a ramping rate of 20°C/min. A stream of 4%H_2/Ar at a flow rate of 20ml/min was fed to 0.05 g of catalyst sample. The samples were heated up to 400°C for moisture removal and cooled down to 200°C before reduction.

After the catalytic testing, the spent catalysts were characterized by Thermogravimetric analysis (TGA) using TGA/SDTA 851^e (Mettler Toledo) instrument. The amount of carbon deposited on the spent catalysts was monitored by temperature-program oxidation (TPO). A high-resolution transmission electron microscope (HRTEM) was used to study the morphology of the deposited carbon. The samples of spent catalysts were ultrasonically dispersed in ethanol and dropped on copper grids for the HRTEM analysis.

3.2.3 Steam reforming of methane

The steam reforming of methane was carried out at atmospheric pressure in a continuous fixed-bed reactor. The quartz tube reactor with an inner diameter of 11 mm was heated in an electric furnace. The temperature was monitored by a K-type thermocouple placed above quartz wool. Before reaction, 100 mg of catalyst was loaded and reduced at 650 °C for 1 h with a stream of 10%H_2/Ar (20 ml/min). Water was completely vaporized by passing through a furnace at 300 °C. A reactant mixture was maintained at CH_4:H_2O:Ar ratio of 1:1:3 with total flow rate of 100 ml/min. The

catalytic testing was conducted at 600 °C and S/C ratio of 1 for 30 h. The reaction products were periodically sampled and analyzed using an on-line gas chromatograph (SRI Instruments, SRI-8610C) equipped with a thermal conductivity detector (TCD) and flame ionization detector (FID). Methane conversion and hydrogen yield were calculated according to the following Eqs 3.1 – 3.2 on dry basis.

$$CH_4 conversion(\%) = \left(\frac{CH_{4,in} - CH_{4,out}}{CH_{4,in}} \right) \times 100 \quad (3.1)$$

$$H_2 yield(\%) = \left[\frac{H_{2,out}}{\left(CH_{4,in} + H_2O_{in} \right) 3} \right] \times 100 \quad (3.2)$$

3.3 Experimental procedure for the comparison of preparation methods between co-impregnation and sequential impregnation

3.3.1 Preparation methods of catalyst

γ-Al_2O_3 powder (Merck) with BET (Brunauer, Emmet and Teller theory) surface area of 132 m^2/g was used as a support. $Ni(NO_3)_2 \cdot 6H_2O$ (Merck), $Ca(NO_3)_2 \cdot 4H_2O$ (Sigma-Aldrich), and $ZrO(NO_3)_2 \cdot H_2O$ (Sigma-Aldrich) were used in the catalyst preparations. The (CaO-ZrO_2)-modified Ni/γ-Al_2O_3 catalysts were prepared by the methods of co-impregnation and sequential impregnation. For the preparation method of co-impregnation, γ-Al_2O_3 powder was impregnated in the mixed solution of the nickel, calcium, and zirconium nitrate hydrate before drying overnight in air at 90 °C and then calcination at 600 °C for 1 h. The catalyst prepared by co-

impregnation method was named NCZA (CI). In the case of sequential impregnation method, γ-Al_2O_3 powder was impregnated in the mixed solution of the calcium and zirconium nitrate before drying overnight in air at 90 °C and then calcination at 850 °C for 1h. The high-temperature calcination was performed to obtain the stable structure of CaO–ZrO_2 phases. At this step, the phase of CaO–ZrO_2 being in form of $CaZrO_3$ perovskite oxide (as expected from 0.5 molar ratio of CaO/ZrO_2) would be deposited on the γ-Al_2O_3 surface. The calcined powder was subsequently impregnated in the solution of nickel nitrate before drying overnight in air at 90 °C and calcination at 600 °C for 1 h. At this step, NiO was deposited on the surface of (CaO–ZrO_2)-modified γ-Al_2O_3. The catalyst prepared by sequential impregnation method was referred to as NCZA (SI).

In addition, two other catalysts were prepared for the comparison to the (CaO–ZrO_2)-modified Ni/γ-Al_2O_3 catalysts: (1) ZrO_2-modified Ni/γ-Al_2O_3 catalyst was prepared the sequential impregnation; (2) typical Ni/γ-Al_2O_3 catalyst was prepared the wetness impregnation method. For the preparation of ZrO_2-modified Ni/γ-Al_2O_3 catalyst, γ-Al_2O_3 powder was impregnated in the solution of zirconium nitrate before drying at 90 °C and calcination at 850 °C. The calcined powder was impregnated in the solution of nickel nitrate before drying at 90 °C and calcination 600 °C (the conditions for two times of drying and calcination of ZrO_2-modified Ni/γ-Al_2O_3 catalyst are identical to that of NCZA (SI)). The ZrO_2-modified Ni/γ-Al_2O_3 catalyst was referred to as NZA (SI). The typical Ni/γ-Al_2O_3 catalyst was prepared by the wetness impregnation of γ-Al_2O_3 in the solution of nickel nitrate before drying at 90 °C and calcination at 600 °C (in the same condition as NCZA (CI)). The typical Ni/γ-Al_2O_3 catalyst was referred to as NA.

All Ni-based catalysts contained 10 wt% Ni. NCZA (CI) and NCZA (SI) were modified with 15 wt% (CaO-ZrO_2) at 0.5 mole ratio of CaO/ZrO_2. NZA (SI) was modified with 15 wt% ZrO_2.

3.3.2 Catalyst characterization

Surface area of the samples was calculated by BET method obtaining from N_2 adsorption/desorption isotherms using a Quantachrome Autosorb-1C instrument. Average pore diameter of samples was determined by BJH (Barret-Joyner-Halenda) method from desorption branch of nitrogen isotherm. Before the measurement, degassing was conducted at 200 °C for 12 h to remove possible moisture. X-ray diffraction patterns of samples were measured on a JEOL: TDX-3530 using Cu Kα radiation (1.541 Å) operated at 30 kV and 40 mA. TPR measurements were carried out in a tubular quartz reactor heated by an electric furnace with a ramping rate of 20 °C/min. The samples were heated up to 400 °C to release moisture and then cooled down to 200 °C prior to the TPR experiments. A stream of 4% H_2/Ar at a flow rate of 20ml/min was fed to 0.05 g of catalyst sample. The amount of H_2 uptake was measured with a TCD detector in a temperature range of 200 to 1000 °C. HRTEM (JEOL:JEM2010) was used to investigate the morphology of the deposited carbon and the nickel sintering on the spent catalysts. The samples of spent catalysts were ultrasonically dispersed in ethanol and dropped on carbon-coated copper grid for the HRTEM analysis. The amount of deposited carbon in the spent catalysts was determined by TGA using TGA/SDTA 851^e (Mettler Toledo) instrument. The samples of spent catalysts were heated up from 30 to 1000 °C in a stream of O_2 at a flow rate of 60 ml/min.

3.3.3 Steam reforming of methane

Steam reforming of methane was carried out under atmospheric pressure in a continuous fixed-bed quartz reactor. The tubular quartz reactor was heated by an electric furnace and reaction temperature was monitored by a K-type thermocouple placed above quartz wool. Each catalyst (100 mg) was loaded into the quartz reactor with an inner diameter of 11 mm. Before catalytic testing, the catalysts sample was reduced at 650 °C for 1h with a stream of 10% H_2/Ar (20 ml/min). Water was injected by a syringe pump and vaporized by passing through a furnace at 300 °C prior to mixing with CH_4 reactant and Ar carrier. Feed compositions were maintained at CH_4:H_2O:Ar ratio of 1:2:3 with total flow rate of 120 ml/min. The catalytic performance was tested at 800 °C and S/C ratio of 2 for 30 h. The reaction products were periodically sampled and analyzed using an on-line gas chromatograph (SRI Instruments, SRI-8610C) equipped with a TCD and FID. CH_4 conversion and H_2 yield were calculated according to the following Eqs. 3.1 and 3.3 on dry basis.

$$H_2 yield(\%) = \left[\frac{H_{2,out}}{2(2CH_{4,in} + H_2O_{in})} \right] \times 100 \qquad (3.3)$$

3.4 Experimental procedure for variation in the loading percentage of CaO–ZrO_2

3.4.1 Preparation of catalyst

Ni/CaO–ZrO_2/α-Al_2O_3 catalysts were prepared by sequential impregnation method. A commercial α-Al_2O_3 powder (AMS-9, Sumitomo Inc., Japan) with BET surface area of 7.85 m^2/g and average pore diameter of 15.96 nm was used as a support. α-Al_2O_3 powder was impregnated in the mixed solution of $Ca(NO_3)_2 \cdot 4H_2O$ (Sigma-Aldrich), and $ZrO(NO_3)_2 \cdot H_2O$ (Sigma-Aldrich) before drying overnight in air at 90 °C and then calcination at 700 °C for 1h. The calcined powder was impregnated in the solution of $Ni(NO_3)_2 \cdot 6H_2O$ (Merck) before drying overnight in air at 90 °C and then calcination at 700 °C for 1 h.

Each of the prepared catalyst consisted of 10 wt% Ni and CaO–ZrO_2 at 0.5 mole ratio of CaO/ZrO_2. The prepared catalysts were named N5(CZ)A, N10(CZ)A, and N15(CZ)A according to the variation in total amount of contained CaO–ZrO_2 at 5, 10 and 15 wt%, respectively. The unmodified catalyst (10 wt% Ni/α-Al_2O_3) was also prepared by the impregnation method for comparison with the modified Ni catalyst and named NA.

3.4.2 Catalyst characterization

X-ray diffraction measurements were carried out using a JEOL: TDX–3530 diffractometer with Cu Kα radiation (λ = 1.541 Å) generated at 30 kV and 40 mA.

The crystallite size of metallic Ni (111) based on peak broadening at 2θ = 44° in the prepared Ni catalysts were calculated using the Scherrer equation as shown in Eq. 3.4.

$$D = \frac{0.9\lambda}{\beta\cos\theta} \quad (3.4)$$

Where D is the crystallite size, λ is the X-ray wavelength, β is the full width of half maximum (FWHM) in radians, and θ is the diffraction angle. The N_2 adsorption–desorption isotherms of the prepared catalysts were measured on a Quantachrome instrument (Autosorb–1C). All the samples were evacuated at 300 °C for 12 h to release the possible moisture prior to the measurements of BET surface area. Average pore diameters were calculated from the desorption isotherms using BJH method. TPR of samples was performed in a tubular quartz reactor heating by an electric furnace with a ramping rate of 20 °C/min. The samples were heated up to 400 °C to release moisture and then cooled down to 200 °C before reduction. A stream of 4% H_2/Ar at a flow rate of 20 ml/min was fed to 50 mg of catalyst sample. The H_2 consumption was measured by a thermal conductivity detector (TCD) in a temperature range of 200–1000 °C. A JEOL JEM2010 high–resolution transmission electron microscope (HRTEM) was used to observe the deactivation of spent catalysts. TEM specimens were prepared by ultrasonic dispersion of catalyst samples in ethanol and then a drop of the suspension on carbon-coated copper grid. Temperature–programmed oxidation (TPO) analyzes of spent catalysts were carried out using a thermo-gravimetric analyzer (Mettler Toledo, TGA/SDTA 851^e) to determine the amount of coke deposited on the catalysts. The samples of spent catalysts were heated up from 30–1000 °C in a stream of O_2 at a flow rate of 60 ml/min.

3.4.3 Steam reforming of methane

Activity tests were performed in a continuous fixed–bed quartz reactor at atmospheric pressure. Catalysts sample (100 mg) was placed in the quartz reactor with an inner diameter of 11 mm. The sample was reduced by heating in a stream of 10% H_2/Ar (20 ml/min) from room temperature to 700 °C for 1 h. Feed compositions were maintained at CH_4:H_2O:Ar ratio of 1:2:3 with a total flow rate of 120 ml/min. The catalytic tests were conducted at 700 °C and S/C ratio of 2 for 10 h. A cold trap at the outlet of the reactor was used to condense any water from the reaction products. The products were periodically sampled and analyzed using an on-line gas chromatography (SRI Instruments, SRI–8610C) equipped with a TCD and FID. CH_4 conversion and H_2 yield were calculated according to the Eqs. 3.1 and 3.3 on dry basis.

CHAPTER IV

RESULTS AND DISCUSSION

4.1 Effect of variation in $CaO–ZrO_2$ molar ratio

4.1.1 Catalysts characterization

The chemical compositions of the prepared catalysts were determined by ICP-OES as shown in Table 4.1. The results confirmed that the mole ratios of CaO/ZrO_2 in the prepared catalysts were corresponding to the designed compositions.

Table 4.1 – Chemical compositions of the fresh catalysts determined by ICP-OES

Catalysts	NiO (%)	CaO (%)	ZrO_2 (%)	Al_2O_3 (%)	CaO/ZrO_2 (mole ratio)
NA	12.8	-	-	87.2	-
NZA	13.0	0	3.5	83.5	0
N20CZA	13.0	0.4	3.3	83.3	0.20
N35CZA	12.9	0.7	3.1	83.3	0.34
N45CZA	12.4	1.1	2.8	83.6	0.46
N55CZA	12.7	1.5	2.6	83.1	0.56

Fig. 4.1 shows XRD patterns of unmodified and ($CaO–ZrO_2$)-modified supports after calcination at 500 °C. All the unmodified and modified supports showed the similar amorphous characteristic of γ-Al_2O_3. In addition, the patterns of all the modified supports did not show $CaO–ZrO_2$ phases. Fig. 4.2 shows XRD patterns of Ni catalysts supported on the unmodified and modified γ-Al_2O_3 after the calcination at 600 °C. All XRD patterns showed the diffraction peaks of NiO and γ-

Al_2O_3. However, $CaO–ZrO_2$ phases still did not appear in these XRD patterns. Fig. 4.3 shows XRD patterns of Ni catalysts supported on the unmodified and modified γ-Al_2O_3 after reduction at 650 °C. All the Ni catalysts on the unmodified and modified supports showed the diffraction peaks of metallic Ni and γ-Al_2O_3. Nevertheless, XRD still could not detect $CaO–ZrO_2$ phases. The invisible phases of $CaO–ZrO_2$ may be attributed to very small amount of $CaO–ZrO_2$ in all the Ni catalysts and the crystallites of $CaO–ZrO_2$ smaller than 3–5 nm, which is below the detection limit of XRD [6].

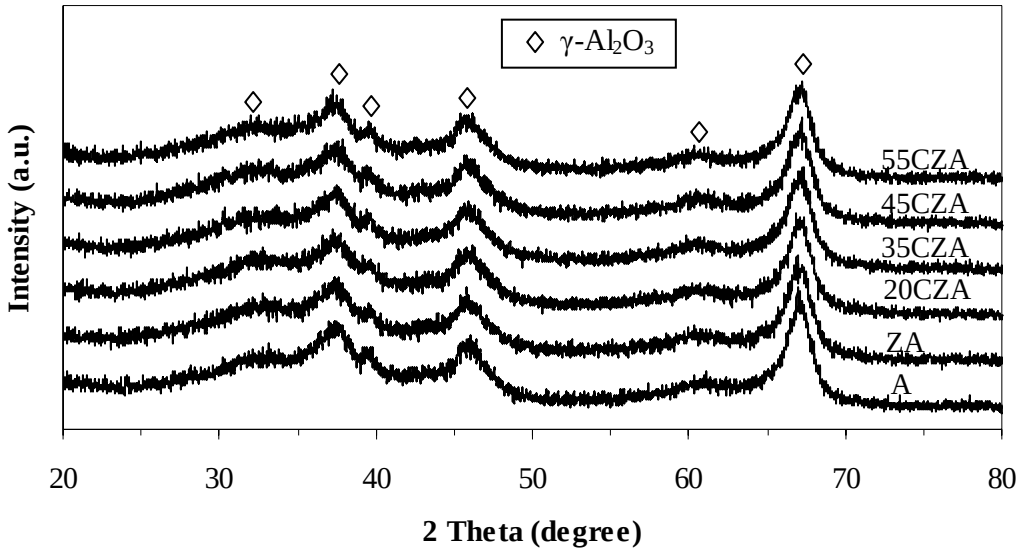

Figure 4.1 – XRD patterns of unmodified and ($CaO–ZrO_2$)-modified γ-Al_2O_3 after calcination at 500 ^oC

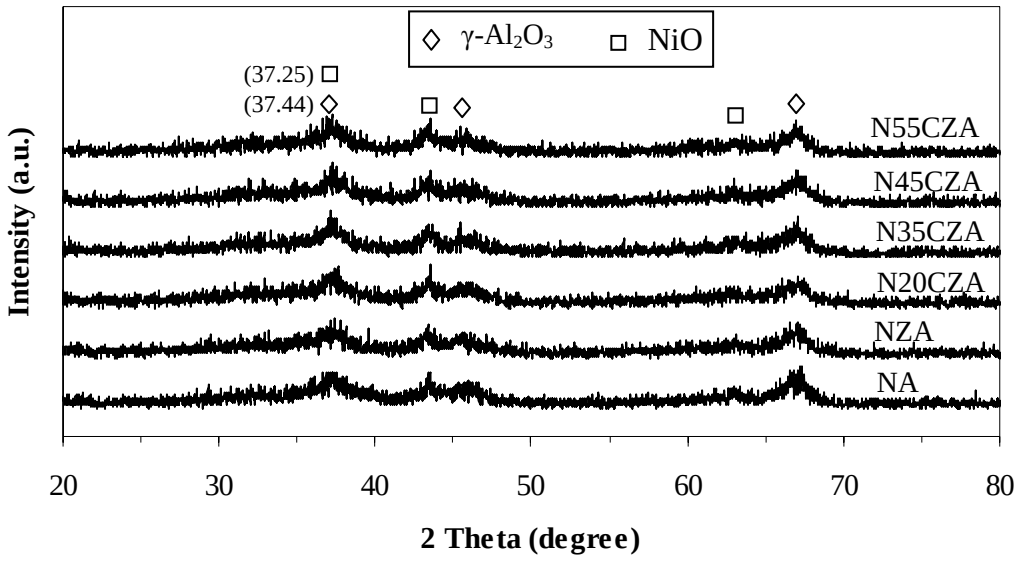

Figure 4.2 – XRD patterns of Ni catalysts supported on unmodified and ($CaO–ZrO_2$)-modified γ-Al_2O_3 after calcination at 600 ^oC

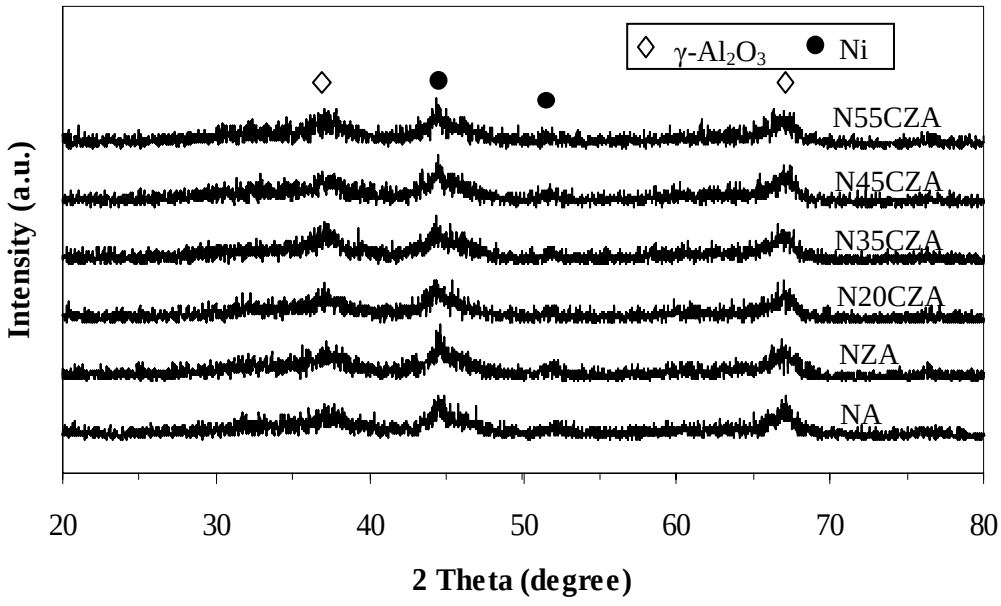

Figure 4.3 – XRD patterns of Ni catalysts supported on unmodified and ($CaO–ZrO_2$)-modified γ-Al_2O_3 after reduction at 650 ^oC

Fig. 4.4 shows BET surface area of both the supports and the calcined and reduced catalysts. There was no trend of the relationship between BET surface area and mole ratios of CaO/ZrO_2 in all the supports and Ni catalysts. The BET surface area of unmodified and modified supports was in the range from 130–150 m^2/g. The BET surface area of calcined catalysts was in the range from 95–115 m^2/g and that of reduced catalysts was in the range from 119–144 m^2/g. The results indicated that the surface area decreased when all the supports were calcined after nickel deposition, and then that of calcined catalysts increased when all the calcined catalysts were reduced in H_2 atmosphere.

After the first calcinations of the $CaO–ZrO_2$ modification of support surface, their BET surface area increased compared to the unmodified supports. This result is attributed to the occurrence of neck and pores between the nanoparticles of $CaO–ZrO_2$ after calcination at 500 °C. However after the second calcination for the deposition of NiO, the BET surface area of all the Ni catalysts decreased. These results might be because NiO was deposited inside the pores of γ-Al_2O_3, and the increase of calcination temperature to 600 °C leading to the disappearance of the neck and pores between $CaO–ZrO_2$ nanoparticles and the growth of the considerable amounts of nanoparticles [15]. The changes that occurred during this calcination process are related to solid state sintering of the $CaO–ZrO_2$ nanopartices. After reduction, the surface areas of all the Ni catalysts were increased due to the loss of the oxygen atom in NiO to form metallic Ni. The result revealed that N55CZA had the highest surface area (144 m^2/g) after reduction, which was even higher than the surface area after the calcination of its support.

Average pore diameters of all supports and reduced Ni catalysts determined by BJH method are shown in Fig. 4.5. All the average pore diameters were in a range

between mesopore (5–50 nm) and micropore (<5 nm). The largest pore diameter of γ-Al_2O_3 was at 7.4 nm; therefore, it had the lowest surface area. The pore diameter of all the modified Ni catalysts after reduction was larger than that of their supports except for N55CZA. In addition, N55CZA after reduction has the smallest pore diameter of 4.6 nm, which is in the range of micropore.

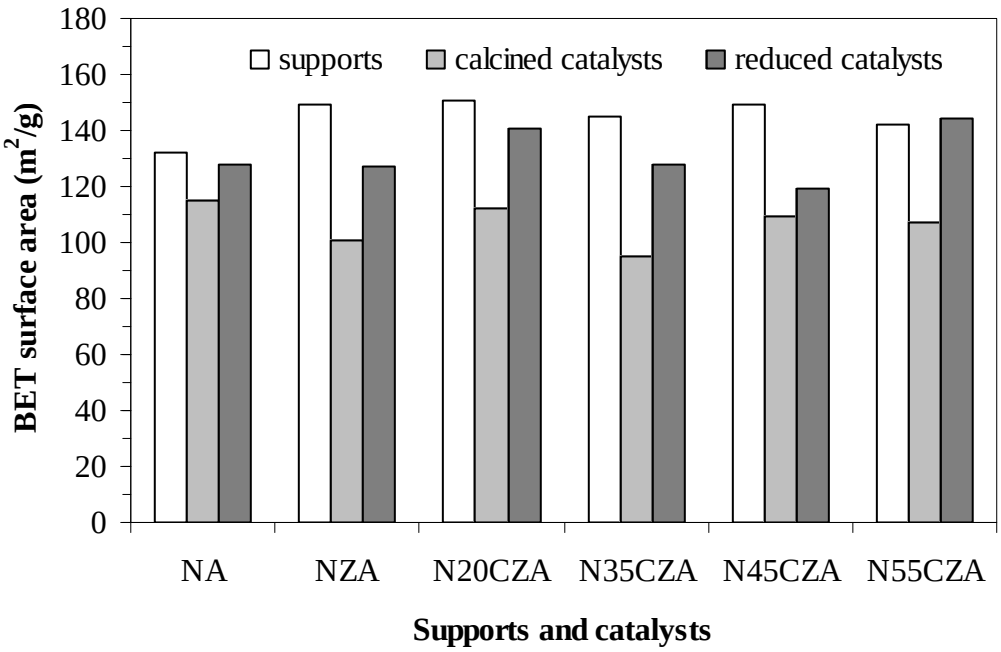

Figure 4.4 – BET surface area of both supports and Ni catalysts

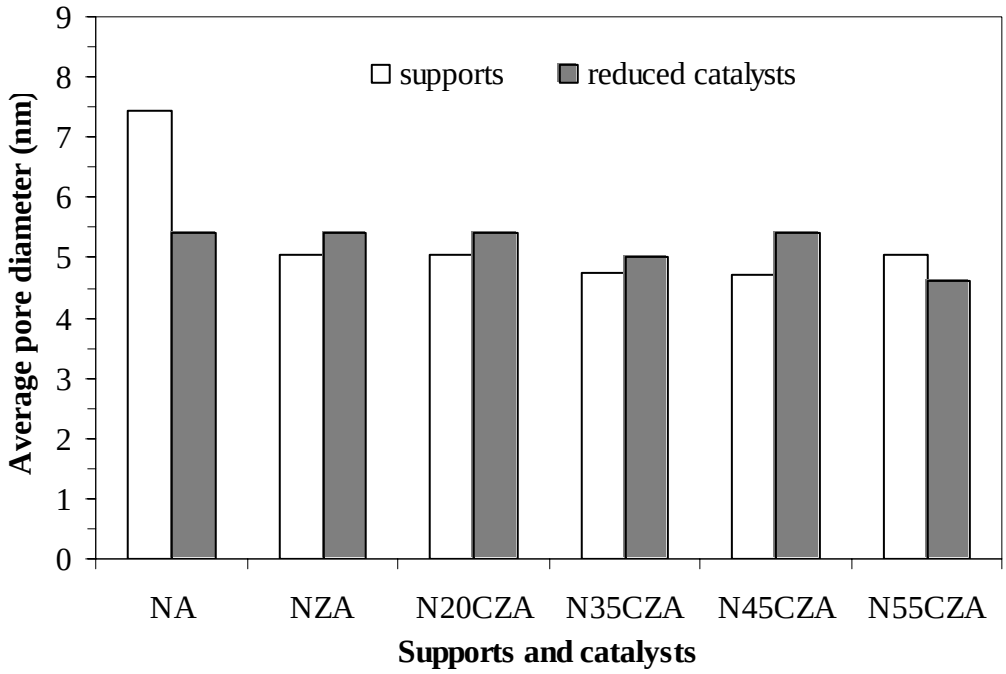

Figure 4.5 – Average pore diameter of both supports and reduced Ni catalysts

In order to identify $CaO–ZrO_2$ phases existing in the fresh catalysts, we investigated the literature on the $CaO–ZrO_2$ phases after calcination at 600 °C. The phase diagram of $CaO–ZrO_2$ in Fig. 4.6 [16] suggests that after the calcination of $CaO–ZrO_2$ at 600 °C, $CaO–ZrO_2$ phases became monoclinic solid solution ZrO_2, $CaZr_4O_9$ $CaZrO_3$, and CaO, depending on mole ratios of CaO/ZrO_2. We performed the TPR using TGA in H_2 atmosphere to monitor the reduction behavior of perovskite (ABO_3) catalysts [17]. Since $CaZrO_3$ (perovskite structure) might exist in the prepared catalysts, N35CZA, N45CZ and N55CZA, we examined all the Ni catalysts using TGA in 4%H_2/Ar at 20 ml/min. Before the examination of all the Ni catalysts in H_2 atmosphere, the Ni catalysts were heated up to 500 °C in Ar atmosphere for the release of moisture content and then cooled down to 100 °C prior to switching to H_2 atmosphere.

Fig. 4.7A shows TPR using TGA in H_2 atmosphere of all the Ni catalysts. In a temperature range of 100–150 °C, all the TGA profiles showed the same pattern due to the switch of atmosphere from Ar to H_2. All TGA profiles similarly indicated the weight loss of catalysts after reduction except for N45CZA and N55CZA, which showed the weight loss in the temperature range of approximately 580–630 °C. In the temperature range of 580–630 °C, N55CZA clearly showed the weight loss of 0.4% (Fig. 4.7B). This weight loss of N55CZA at the temperature range was low because the total amount of CaO–ZrO_2 in the catalyst was of only 5%. However, its DTA profiles supported the weight loss from the existence of endothermic peak in this temperature range (not shown here). This weight loss was attributed to the formation of oxygen vacancies in $CaZrO_3$ perovskite-type oxides — $CaZrO_{3-\delta}$ [18,19]. Therefore, the suggestion of the phase diagram and TGA results confirmed that CaO–ZrO_2 phases existed in the form of monoclinic solid solution ZrO_2 for NZA, $CaZr_4O_9$ for N20CZA, the mixed $CaZr_4O_9$ with $CaZrO_3$ for N35CZA and N45CZA, and the mixed $CaZrO_3$ with CaO for N55CZA. As a result of the significant amount of oxygen vacancies formation in N55CZA after reduction, its average pore diameter was the smallest, yielding the highest surface area after reduction. No trend in relationship between the surface area and mole ratios of CaO/ZrO_2 may be attributed to the existence of different phases of CaO–ZrO_2 in each individual Ni catalyst.

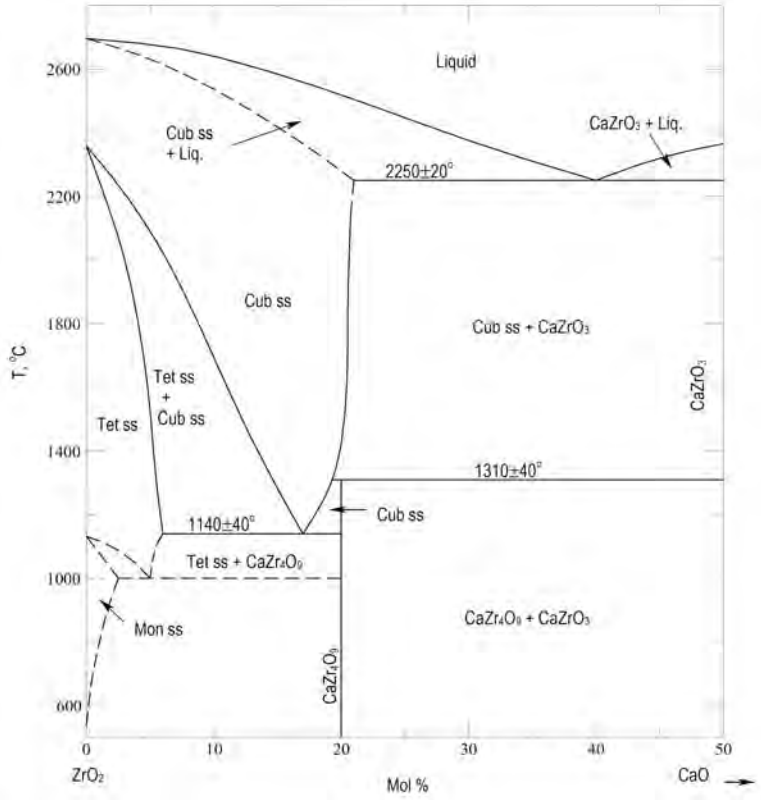

Figure 4.6 – Phase diagram of CaO–ZrO_2 [16]

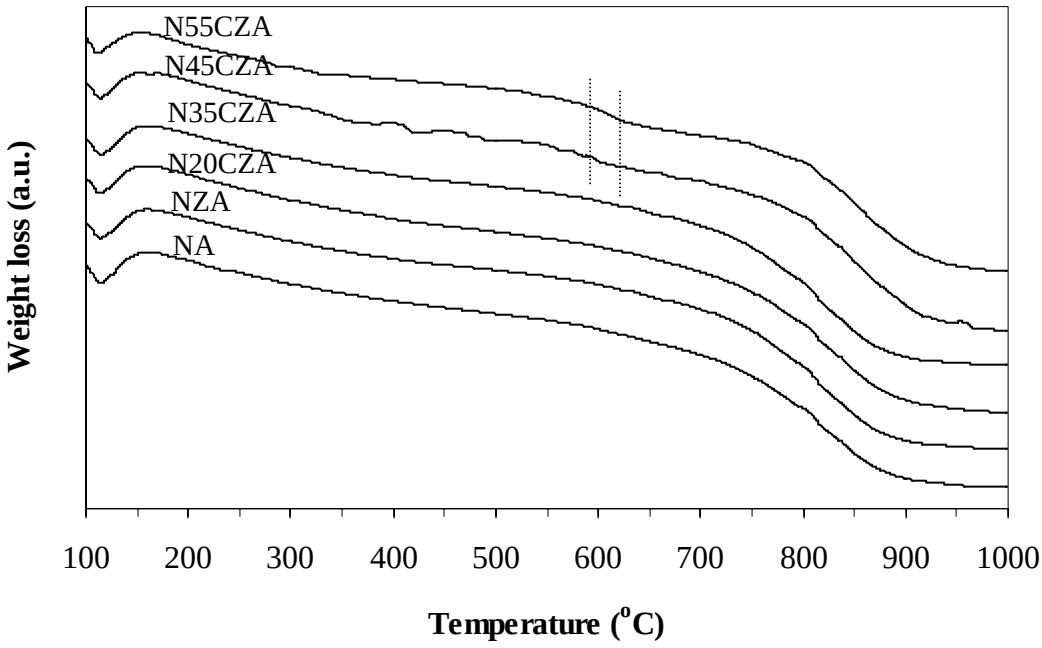

Figure 4.7A – TPR using TGA in H_2 atmosphere for unmodified and (CaO–ZrO_2)-modified Ni catalysts

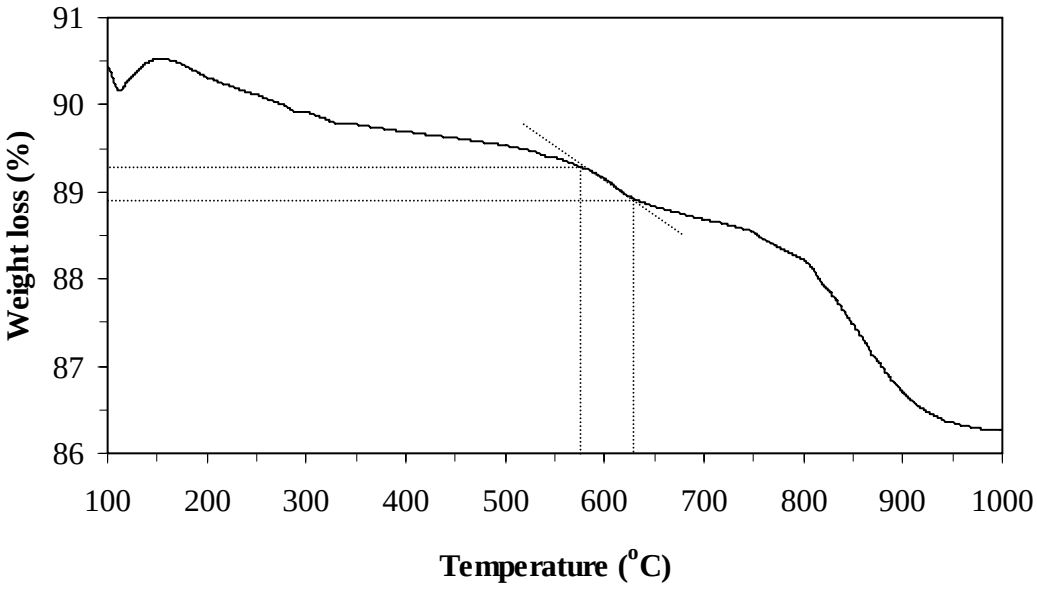

Figure 4.7B – TPR using TGA in H_2 atmosphere in more detail for N55CZA

TPR profiles of all the catalysts are displayed in Fig. 4.8. It is well known that the reduction peak of bulk NiO appears at approximately 500 °C, and that of nickel aluminate ($NiAl_2O_4$) appears at a high temperature of approximately 800 °C [20,21]. NiO specie reduced in the range of 700–770 °C might be attributed to the strong interaction between NiO and monoclinic solid solution ZrO_2 leading to a high reduction temperature. Reduction bands in the range of 570–700 °C are attributed to the reduction of $CaZrO_3$ to be $CaZrO_{3-\delta}$. It was observed that the temperature range of $CaZrO_3$ reduction using TGA in H_2 atmosphere corresponded with that using TPR. In addition, the area under peaks indicating H_2 consumption of $CaZrO_3$ increased with the increase of CaO/ZrO_2 mole ratios from 0.35 to 0.55. Thus, these results confirmed that the order of increasing $CaZrO_3$ amount in the Ni catalysts (N35CZA < N45CZA < N55CZA), corresponding with the $CaO–ZrO_2$ phase diagram. Consequently, each individual catalyst revealed the peaks of reduced species consisting of bulk NiO (470–570 °C), $CaZrO_3$ (570–700 °C), NiO on monoclinic solid solution ZrO_2 (700–770

°C), and $NiAl_2O_4$ (800–900 °C). All the Ni catalysts indicated the reduction of bulk NiO. The reduction of NiO on monoclinic solid solution ZrO_2 was shown only in NZA and that of $NiAl_2O_4$ was found in NZA and N55CZA. However, since all the catalysts were reduced at 650 °C prior to actual catalytic testing in this, only bulk Ni and $CaZrO_{3-\delta}$ existed in the Ni catalysts before steam methane reforming.

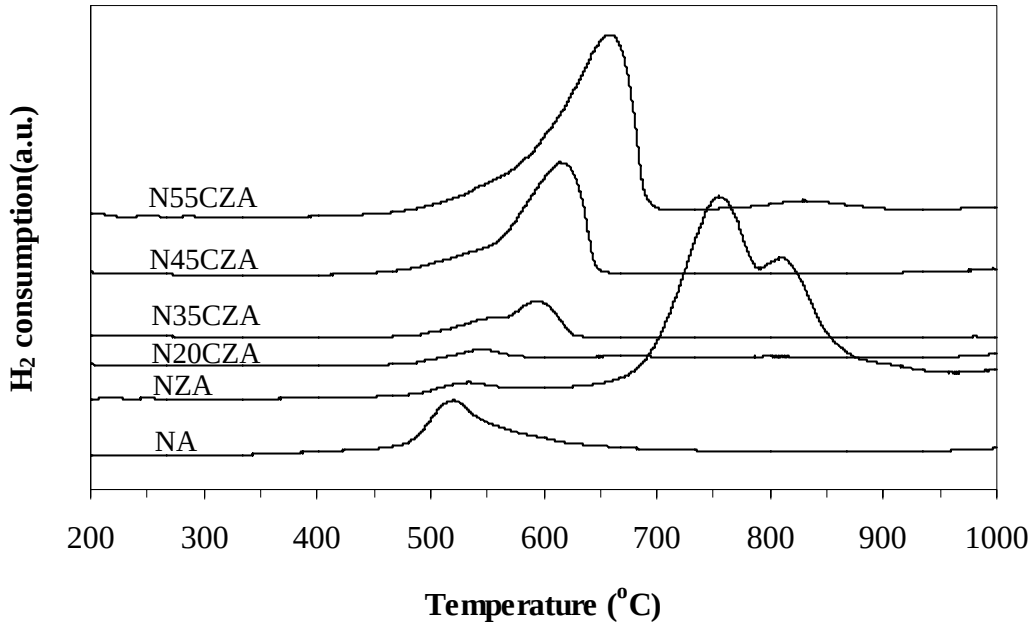

Figure 4.8 – TPR profiles of unmodified and ($CaO–ZrO_2$)-modified Ni catalysts

4.1.2 Catalytic testing and catalysts deactivation

Fig. 4.9 shows CH_4 conversion of unmodified and ($CaO–ZrO_2$)-modified Ni catalysts with respect to time on stream during steam methane reforming for 30 h at 600 °C and S/C ratio of 1. The conversion of CH_4 was classified into three ranges according to the percentage of CH_4 conversion. NA and N20CZA provided the conversion of approximately 60% whereas NZA, N45CZA and N55CZA provided

approximately 45%. However, N35CZA indicated the unstable characteristic of CH_4 conversion.

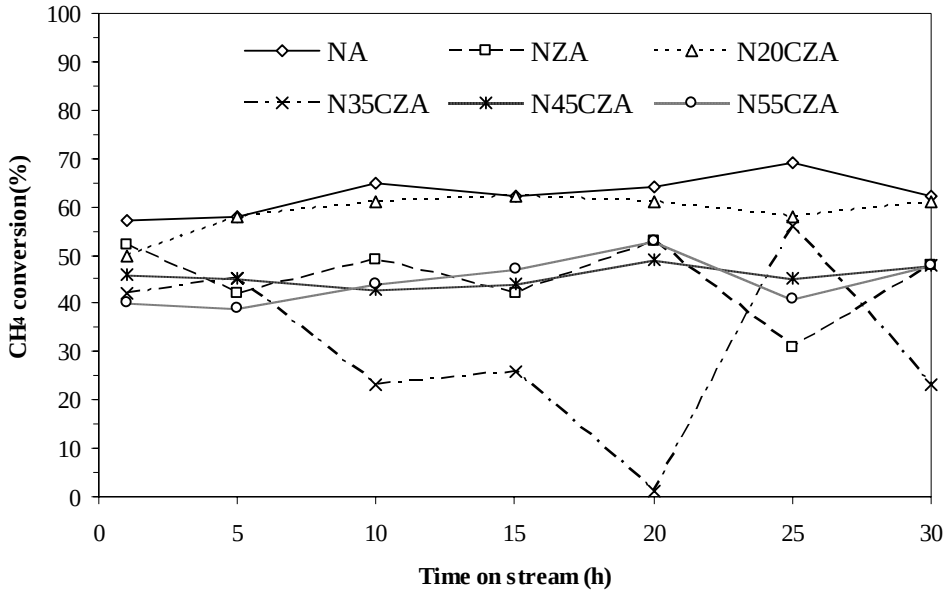

Figure 4.9 – CH_4 conversion with time on stream of unmodified and ($CaO–ZrO_2$)-modified Ni catalysts after steam methane reforming at 600 ^oC, S/C ratio = 1

H_2 yield of the unmodified and ($CaO–ZrO_2$)-modified Ni catalysts with respect to time on stream in the steam methane reforming for 30 h are shown in Fig. 4.10. N55CZA revealed the highest H_2 yield of approximately 35%. The order of decreasing H_2 yield was found to be N55CZA > NA > N45CZA > N20CZA. Nevertheless, NZA and N35CZA indicated unstable characteristics of H_2 yield. Interestingly, although N55CZA provided the lower CH_4 conversion than NA, N55CZA provided the higher H_2 yield. This result is attributed to the enhanced adsorption of water on $CaZrO_{3–\delta}$. Since $CaZrO_{3–\delta}$ lost its oxygen sites, the oxygen atom in the adsorbed might prefer to substitute the oxygen vacancies to maintain its stability [19]. This water adsorption can led to the enhancement of carbon gasification as confirmed by high CO concentration in Fig. 4.11 and then that of water gas shift

reaction as confirmed by high CO_2 concentration in Fig. 4.12. Therefore, $CaZrO_3$ acts as a chemical promoter in N55CZA supplying water molecules onto the active Ni sites.

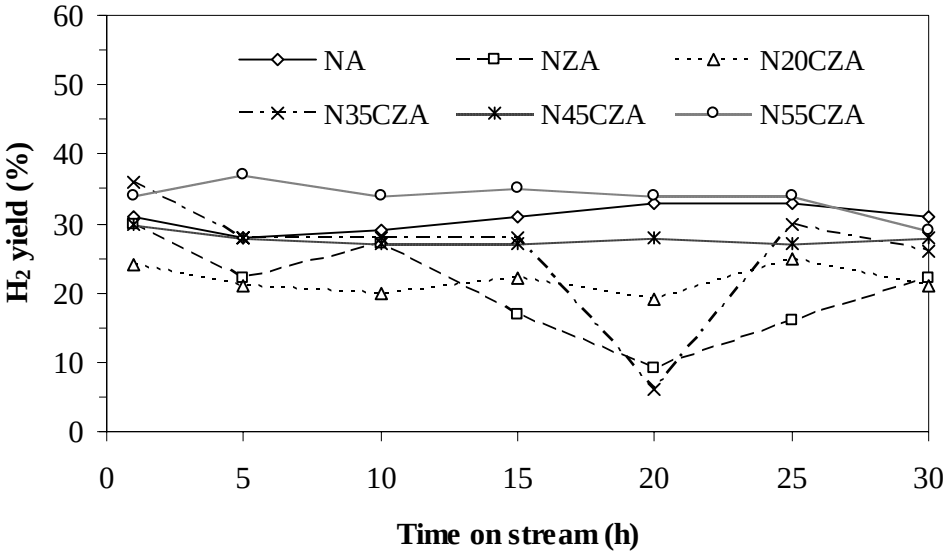

Figure 4.10 – H_2 yield with time on stream of unmodified and ($CaO–ZrO_2$)-modified Ni catalysts after steam methane reforming at 600 ^oC, S/C ratio of 1

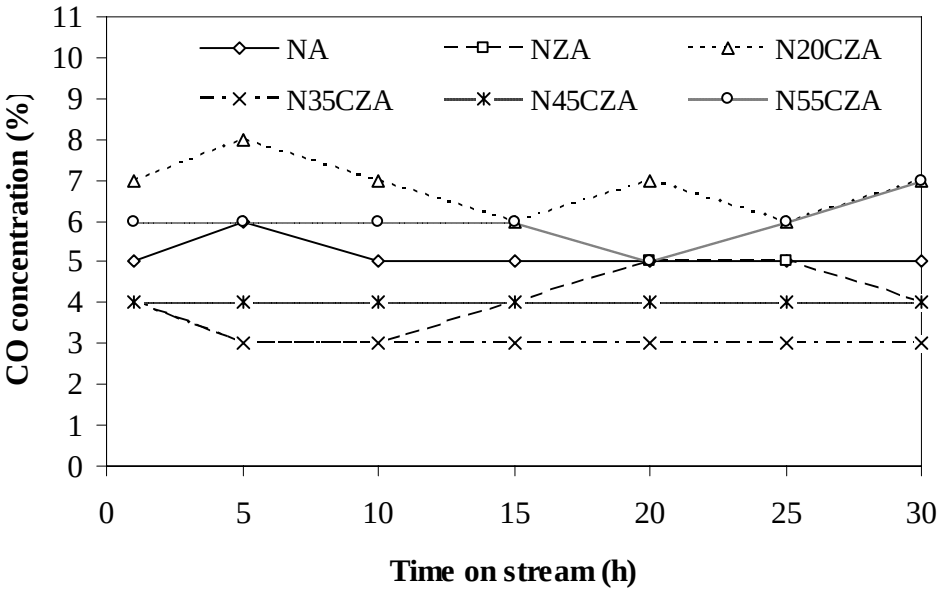

Figure 4.11 – CO concentration in outlet product compositions on dry basis after catalytic testing for 30 h

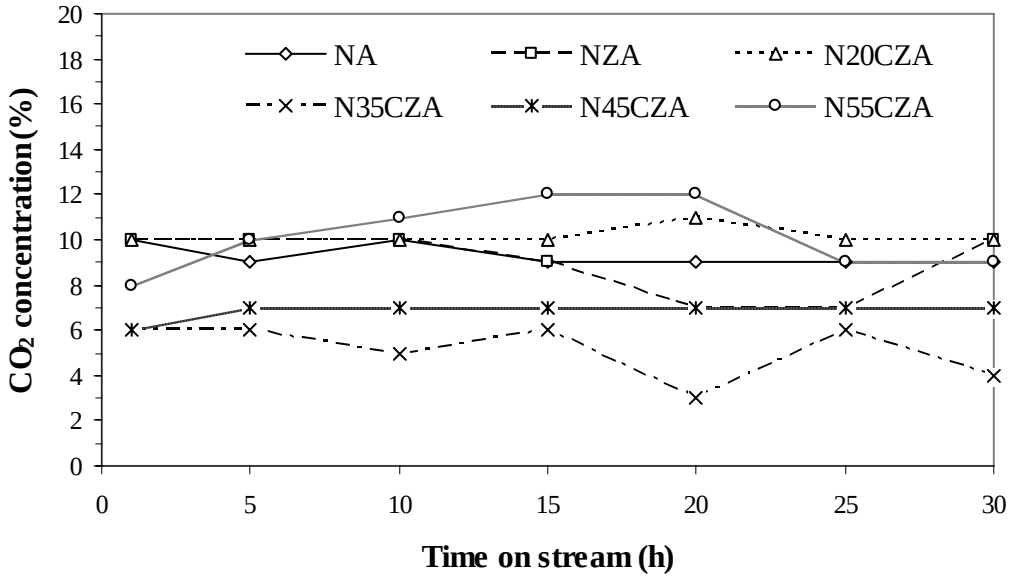

Figure 4.12 – CO_2 concentration in outlet product compositions on dry basis after catalytic testing for 30 h

In the case of N20CZA, although N20CZA showed the high percentage of CH_4 conversion (~58%) and CO_2 concentration (~10%), H_2 yield of only 22% was obtained. $CaZr_4O_9$ in N20CZA was believed to act as a structural promoter, i.e., the improvement of Ni dispersion followed by the strong metal-support interaction (SMSI) in N20CZA leading to the high BET surface area after reduction (Fig. 4.4). This might be responsible for the high CH_4 conversion. However, the facility for water adsorption on $CaZr_4O_9$ was negligible. Therefore, the water adsorption arose only from γ-Al_2O_3 resulting in the low water dissociation on the active Ni sites.

N35CZA showed the lower CH_4 conversion, H_2 yield and CO_2 concentration than N45CZA. Although both catalysts consisted of $CaZr_4O_9$ and $CaZrO_3$ phases, N45CZA contained a higher amount of $CaZrO_3$ than N35CZA as confirmed by the higher reducibility of N45CZA in TPR profiles. Therefore, N45CZA contributed to the higher carbon gasification and water gas shift reaction than N35CZA. This implies

that the existence of $CaZrO_3$ in nickel catalysts improved the activity in steam methane reforming.

TEM images of the spent catalysts in steam methane reforming for 30 h are shown in Fig. 4.13. Table 4.2 shows the amount of carbon deposition on all the spent catalysts. The total amount of carbon in Table 4.2 agreed with the TEM results. NA and N20CZA showed a low total amount of coke (5%) in TGA results corresponding with their TEM images because there was no appearance of whisker carbon. However, NZA, N35CZA, N45CZA and N55CZA showed a considerable amount of whisker carbon. The order of decreasing the total amount of carbon was N35CZA > N45CZA > NZA > N55CZA > NA, N20CZA. NA and N20CZA had the low amount of whisker carbon due to their strong metal-support interaction. This result differed from NZA, N35CZA, N45CZA and N55CZA with weak metal-support interaction. Due to their weak metal-support interaction, Ni particles were pushed away by the carbon deposition and separated from their supports. The carbon was then continuously grown in the form of whiskers or carbon nanotubes [22,23]. In addition, TGA results showed that the total amount of carbon in the spent catalysts containing $CaZrO_3$ (N35CZA, N45CZA and N55CZA) was decreased with increasing amount of $CaZrO_3$ in the modified Ni catalysts. This result is attributed to the increase of water adsorption with increasing $CaZrO_3$, resulting in the increase of carbon gasification and the decrease of carbon formation. The oxidation of nickel appeared only in NA and N20CZA due to the effect of the modified supports.

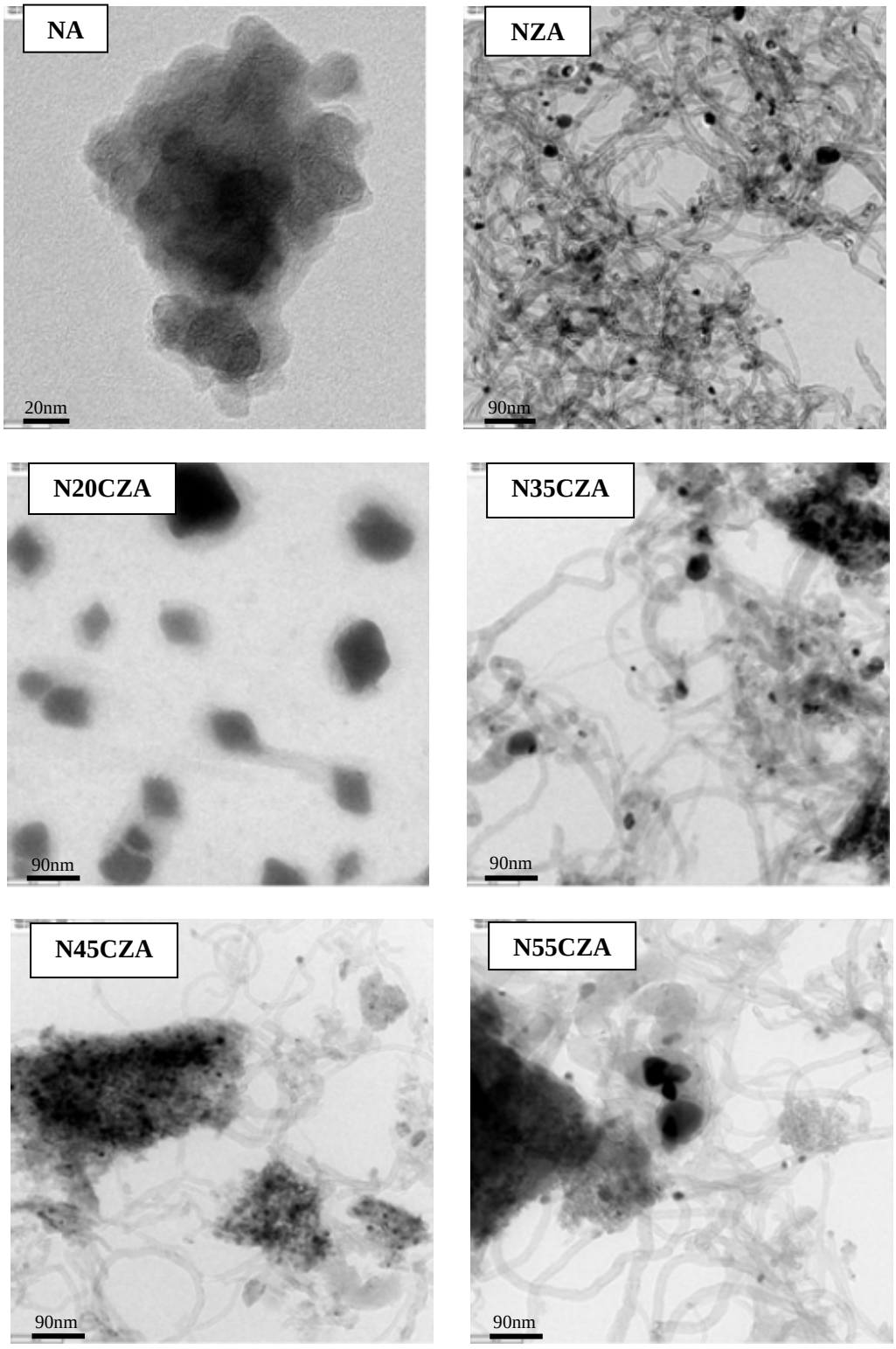

Figure 4.13 – TEM images of spent catalysts after catalytic testing for 30 h

Table 4.2 – Total amount of carbon after catalytic testing and nickel oxidation by TGA

Catalysts	Total amount of carbon ($mg_{carbon}/g_{cat.}$)	Oxidation of nickel (%)
NA	6	0.3
NZA	177	0
N20CZA	4	0.5
N35CZA	181	0
N45CZA	172	0
N55CZA	59	0

The used catalysts with the large amount of whisker carbon as appeared in NZA, N35CZA and N45CZA were found to exhibit unstable activity, i.e., CH_4 conversion and H_2 yield sharply decreased and then increased. This result was not because Ni surface is poisoned by whisker carbon. Instead, whisker carbon completely covered Ni surface leading to the inactive Ni sites for the catalytic reaction. Moreover, the loss of the catalytic activity arose from plugging the catalysts pores by whisker carbon. When the carbon built up to a substantial level, the pressure drop was increased, which mean that the Ni catalysts showed very low activity [6]. In our catalytic testing, when pressure drop was significantly increased, the Ni catalysts powder completely separated each other, which mean that the powder moved into quartz wool. Ultimately, these Ni catalysts were active again, which mean the increase in their activity again because active Ni sites were no longer covered by whisker carbon.

4.2. Comparison between co-impregnation and sequential impregnation

4.2.1 Identification of phases

XRD patterns of all the Ni catalysts after calcination are shown in Fig. 4.14. All the XRD patterns indicated amorphous characteristics of γ-Al_2O_3. In general, γ-Al_2O_3 is transformed into δ-Al_2O_3 at the temperature of about 900 °C [8,24]. Therefore, the phase identification in this work corresponded to the common characteristic of Al_2O_3 powder. All the Ni catalysts clearly showed the existence of NiO phase. XRD detected the existence of ZrO_2 (tetragonal ZrO_2) phase only in NZA (SI) and NCZA (SI); however, no tetragonal ZrO_2 phase was observed in NCZA (CI). The invisible phase of both CaO and ZrO_2 in NCZA (CI) are attributed to the preparation method of co-impregnation leading to the fine dispersion of NiO, CaO, and ZrO_2 on pore wall and surface of γ-Al_2O_3 in NCZA (CI). In addition, XRD is unable to detect the phase of CaO in NCZA (CI) and NCZA (SI).

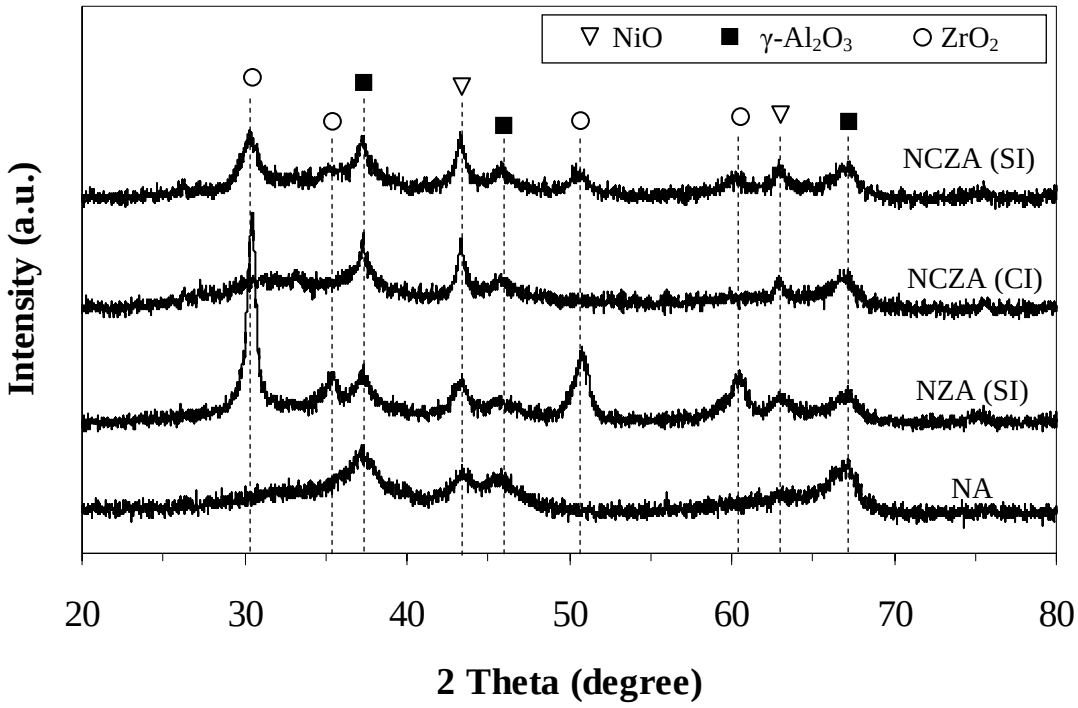

Figure 4.14 – XRD patterns of all the calcined Ni catalysts

Fig. 4.15 exhibits the XRD patterns of all the Ni catalysts after reduction at 650 °C for 1h. All the XRD patterns demonstrated not only the diffraction peaks of metallic Ni, but also small diffraction peaks of NiO phase at 2θ = 43 and 63°. This means that NiO phase converts incompletely into metallic Ni at the reduction temperature of 650 °C. Furthermore, it was noticeable that NiO peak of NZA (SI) at 2θ = 63° was larger than that of the other reduced catalysts. The result implied that it was difficult to reduce NiO phase in NZA (SI). From all the XRD patterns, the results revealed that the types of impregnation method significantly influenced the crystal size and the existing phases in all the Ni catalysts both after calcination and reduction.

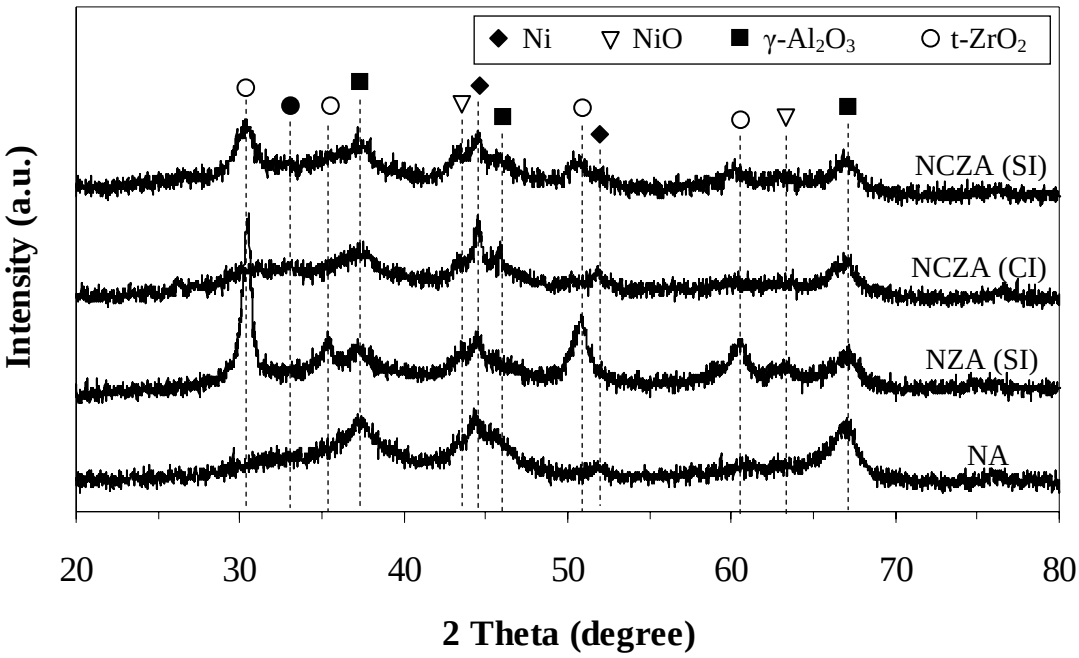

Figure 4.15 – XRD patterns of all the reduced Ni catalysts

4.2.2 Textural characteristics

BET surface area of all the calcined and reduced Ni catalysts is shown in Fig. 4.16. After the calcination, BET surface area of NCZA (CI) was higher than that of NA. However, BET surface area of NZA (SI) and NCZA (SI) was lower than that of NA. The increase in BET surface area of NCZA (CI) was resulted from the suitable dispersion among NiO, CaO, and ZrO_2 during the co-impregnation and drying stages. When the solid state sintering of the oxides occured during the calcination stage, neck and pores among the oxides formed [6]. The mechanisms resulted in the increase in BET surface area of NCZA (CI). In each Ni catalyst, their surface area after reduction was larger than that after calcination. Interestingly, after reduction NCZA (SI) indicated considerable increase in its BET surface area compared to the other Ni catalysts. The percentage increase in BET surface area of all the calcined Ni catalysts

after reduction step was displayed in Table 4.3. Obviously, although the composition of NCZA (CI) was the same as that of NCZA (SI), the percentage increase in BET surface area of NCZA (SI) was almost six times higher than that of NCZA (CI). The significantly higher percentage increase in surface area of NCZA (SI) is attributed to its preparation by sequential impregnation method.

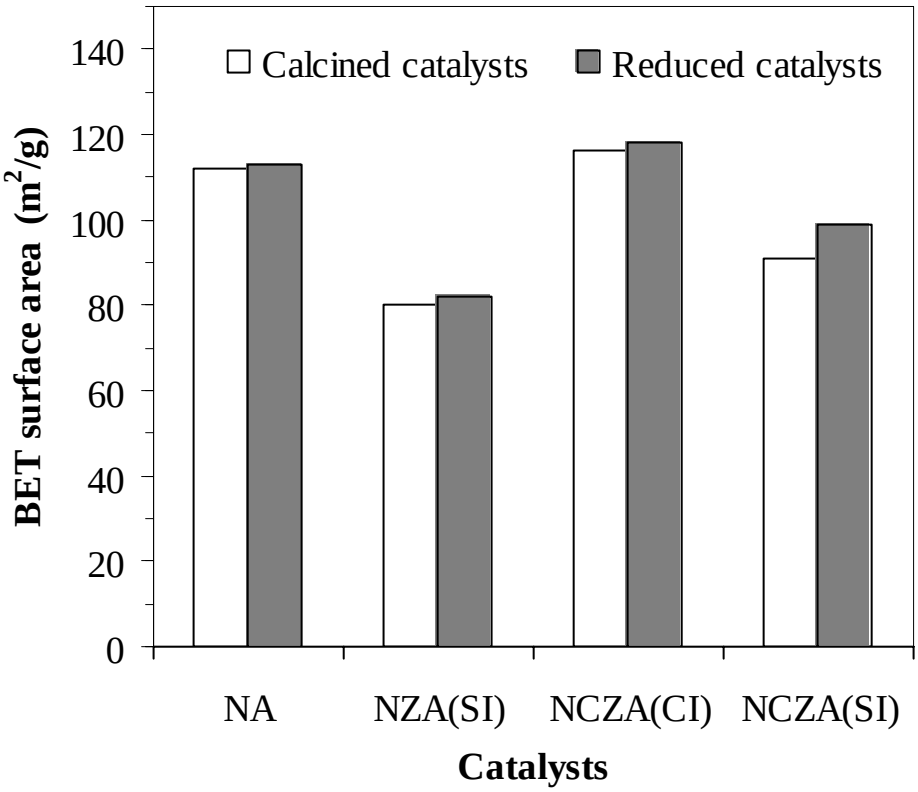

Figure 4.16 – BET surface area of all the calcined and reduced Ni catalysts

The average pore diameter of all the calcined and reduced Ni catalysts was in the range of mesopore (5–50 nm) (Fig. 4.17). The highest average pore diameter (the lowest surface area) was observed in NZA (SI). All the calcined catalysts exhibited the increase in their average pore diameters after the reduction stage, except NCZA (SI). Table 4.3 demonstrates the percentage change of average pore diameters of all

the calcined Ni catalysts after the reduction stage. NCZA (SI) indicated the negative percentage change in average pore diameter (approximately -1), whereas the other Ni catalysts indicated the positive value. The negative change in pore diameter of NCZA (SI) was an evident supporting the high percentage increase in its surface area after the reduction stage.

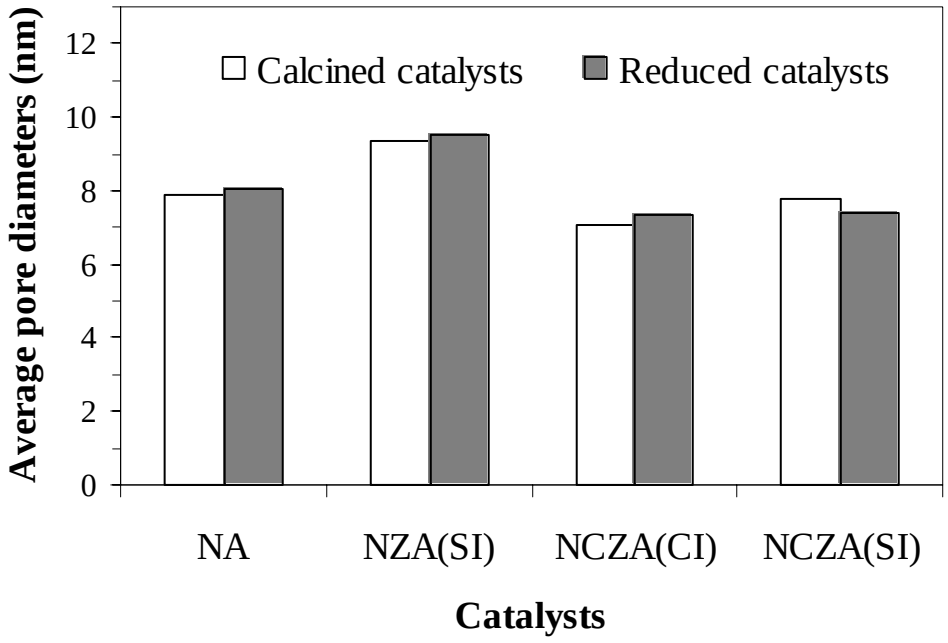

Figure 4.17 – Average pore diameters of all the calcined and reduced Ni catalysts

Table 4.3 – Changes of BET surface area and average pore diameters of all calcined Ni catalysts after reduction stage at 650 °C for 1 h

Catalysts	Surface area change (%)	Pore diameter change (%)
NA	+0.9	+1.02
NZA(SI)	+2.5	+1.02
NCZA(CI)	+1.5	+1.04
NCZA(SI)	+8.5	-0.95

4.2.3 Reducibility of catalysts

TPR profiles of all the Ni catalysts are shown in Fig. 4.18. All the Ni catalysts, except NZA (SI), consumed H_2 in the temperature range of 440–600 °C, which is the range for the reduction of bulk NiO strongly reacting with γ-Al_2O_3 [25]. NZA (SI) did not consume H_2 over performing the TPR experiment. The result is attributed to the preparation method by sequential impregnation of NZA (SI)—that is the first calcination for the ZrO_2 deposition at 850 °C and then the second calcination for the NiO deposition at 600 °C. The sequence of impregnation and then calcination is believed to have major effect on the formation of ZrO_2-Al_2O_3 and NiO-ZrO_2 solid solution on the γ-Al_2O_3 support [25-29]. Both clusters of the solid solution have thermodynamically stable characteristic, resulting in almost unreducible condition of active phases in NZA (SI). The unreducible characteristic of NZA (SI) was in agreement with the larger NiO peak at $2\theta = 63°$ in its XRD pattern. The reduction bands in the range of 600–700° C were observed in only NCZA (CI) and NCZA (SI). The existence of both bands, which show particularly high H_2 uptake, is attributed to the existence of perovskite $CaZrO_3$. When $CaZrO_3$ was reduced under H_2 atmosphere, oxygen vacancies were generated by the reaction between oxygen atoms in the $CaZrO_3$ structure and H_2 molecules, from which led to the formation of H_2O molecules. As a result of the reaction in which consumed considerable amount of H_2, it involved the release of lattice oxygen in $CaZrO_3$ perovskite oxide [17,19,30]. This reduction band is identical to the reduction band in TPR profile of the Ni catalyst containing CaO–ZrO_2 at 0.55 mole ratio of CaO/ZrO_2 in our previous work [31]. In addition, the equal height of both the bands in the TPR profiles of NCZA (CI) and NCZA (SI) implied that both catalysts consisted of the equal amount of $CaZrO_3$.

Thus, although NCZA (CI) and NCZA (SI) were prepared from the different methods of impregnation, both catalysts contained the same phase and equal amount of $CaZrO_3$.

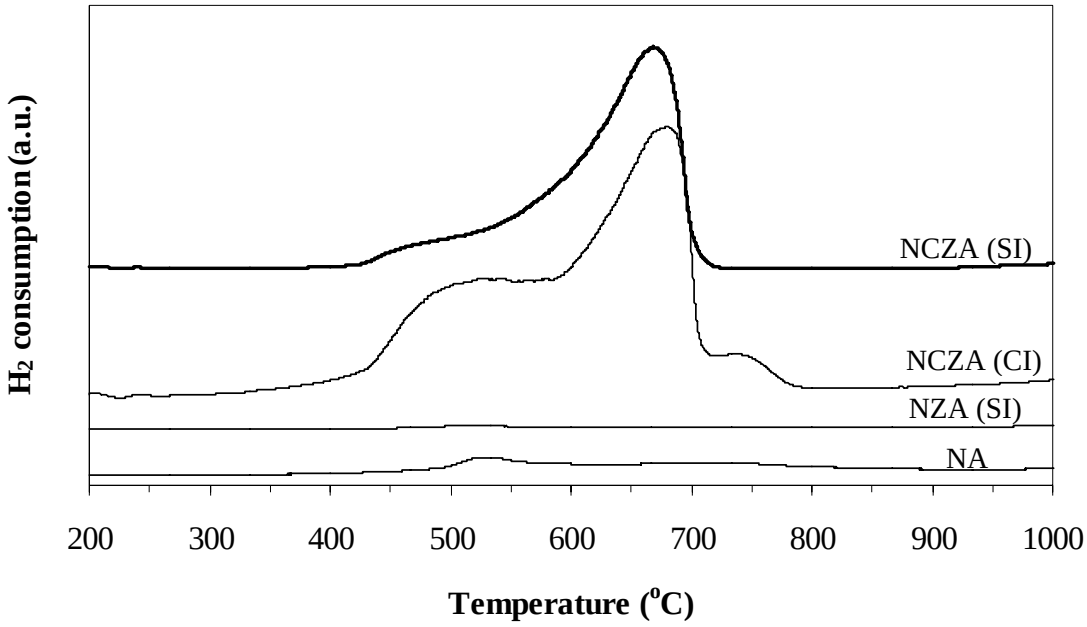

Figure 4.18 – TPR profiles of all the Ni catalysts

It should be noted that TPR experiments provided the strong evidence on the existence of $CaZrO_3$ phase, whereas XRD did not. Moreover, the existence of $CaZrO_3$ phase is confirmed by ZrO_2–CaO phase diagram. The phase diagram, considered at 0.5 mole ratio of CaO/ZrO_2 suggests that CaO reacts with ZrO_2 to form $CaZrO_3$ at temperatures higher than 500 °C. The effects of calcination at 600 °C involved 2 stages of bonding among the oxides within NCZA (CI): (1) initial bonding between the particles of CaO and ZrO_2 becoming $CaZrO_3$ after heating from ~500 °C, (2) subsequent bonding between the particles of $CaZrO_3$ and NiO, and also that of ZrO_2 and NiO. Therefore, it was possible that $CaZrO_3$ with nanometer size, which was below the detection limit of XRD (<5nm), was formed in both the Ni catalysts. The

reduction band in the temperature range of 700–800 °C is attributed to the reduction of NiO specie strongly reacted with ZrO_2 in NCZA (CI).

4.2.4 Relationship between the impregnation methods and structural characterizations

By combining XRD, BET surface area, average pore diameters and TPR results, although both NCZA (CI) and NCZA (SI) had the same composition, the different methods of impregnation led to the distinguishable structural characteristics. NCZA (SI) revealed (1) an additional diffraction peak of ZrO_2, (2) the negative percentage change of pore diameter and (3) the irreducible condition of NiO on ZrO_2. These characteristics of NCZA (SI) are attributed directly to its preparation method by sequential impregnation. For the first impregnation and calcination, the surface of the modified γ-Al_2O_3 consisted of the highly-stable phases of ZrO_2 and $CaZrO_3$ due to the high-temperature calcination (850 °C). The results, therefore, involved the strong peak of ZrO_2 in the XRD pattern and also the smaller pore diameter due to the formation of oxygen vacancies on the surface of $CaZrO_3$. For the second impregnation and calcination, NiO was deposited on some part of ZrO_2 and $CaZrO_3$ particles and on γ-Al_2O_3 surface. The deposition of NiO on the stable, separated ZrO_2 particles offered strong interaction between NiO and ZrO_2 due to the high-temperature calcination leading to the unreducible condition of NiO on ZrO_2 particles.

For NCZA (CI), its structural characteristics resulted from fine dispersion and intimate connection among NiO, CaO, and ZrO_2 particles leading to the existence of nanocomposite of the three phases. Therefore, NCZA (CI) did not show the diffraction peaks of ZrO_2 due to the nanometer-size particles of ZrO_2. The larger pore

diameter after the reduction stage in the nanocomposite catalyst is because NiO and $CaZrO_3$ that contact with each other and were reduced simultaneously released their oxygen atoms and then led to the combination of oxygen vacancies to the larger pores.

4.2.5 Catalytic testing

CH_4 conversion during steam methane reforming over all the Ni catalysts for 30 h is shown in Fig. 4.19. NA indicated the CH_4 conversion between 85 and 98% over 30 h. CH_4 conversion of NCZA (SI) was in the range of 75–95%. CH_4 conversion of NCZA (CI) was low (~55%) at the time on stream of 1 h, increased to 98% and then continue at this level over a period of time, and finally dropped to ~45% at the time on stream of 30 h. NZA (SI) showed the wide fluctuation in CH_4 conversion from 0–98%. Fig. 4.20 exhibits H_2 yield during steam methane reforming over all the Ni catalysts for 30 h. H_2 yield of NA (~65%) was slightly higher than that of NCZA (SI) (~60%). For NCZA (CI), the trend of H_2 yield was similar to that of its CH_4 conversion, i.e., H_2 yield was low (~35%) at the early stage, and then increased to 65% over the subsequent 20 h, and finally dropped to 45%. In the case of NZA (SI), the H_2 yield widely fluctuated from 0–80% similar to its CH_4 conversion.

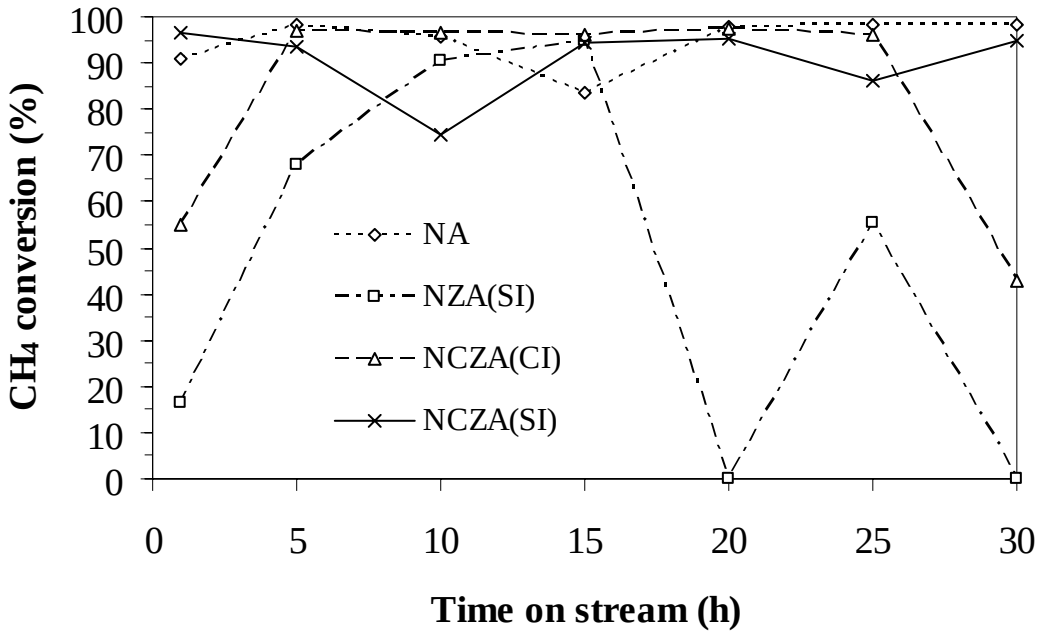

Figure 4.19 – CH4 conversion during steam methane reforming over all the Ni catalysts at 800 °C and S/C ratio of 2 for 30 h

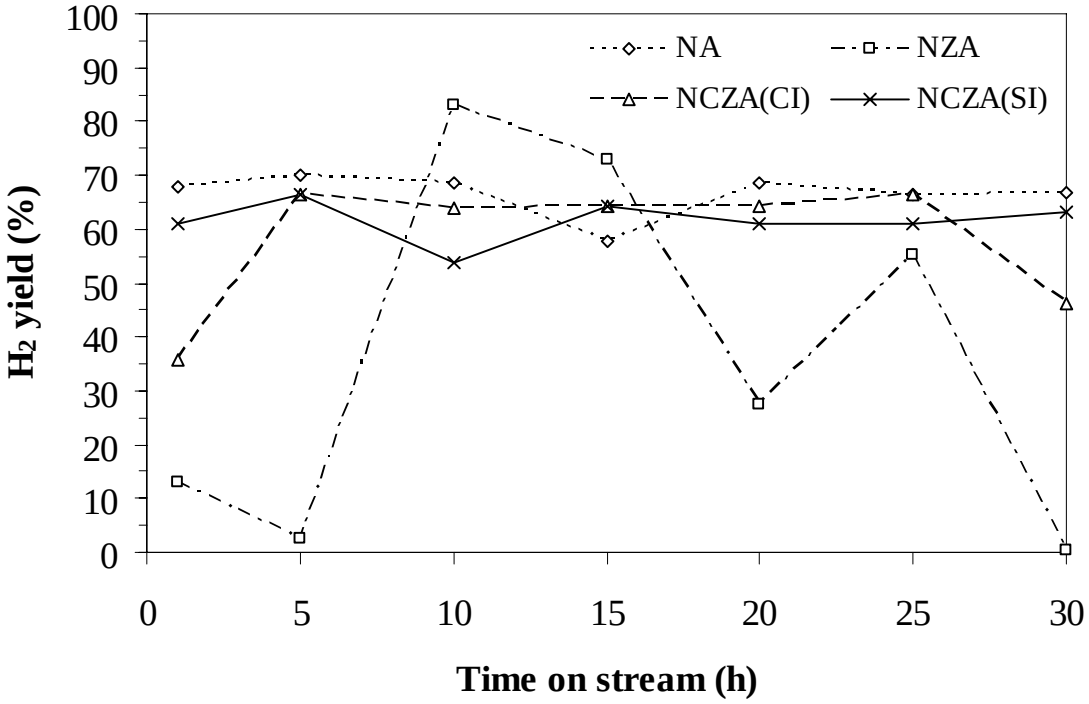

Figure 4.20 – H_2 yield during steam methane reforming over all the Ni catalysts at 800 °C and S/C ratio of 2 for 30 h

Fig. 4.21 and 4.22 demonstrate the CO and CO_2 concentrations, respectively, in the outlet products, obtained from steam methane reforming over all the Ni catalysts. The concentration of both product gases is useful for discussion on the reactions of carbon gasification and water gas shift reaction (WGSR) (Eq. 2.2) and Boudoudard reaction (Eq. 2.5).

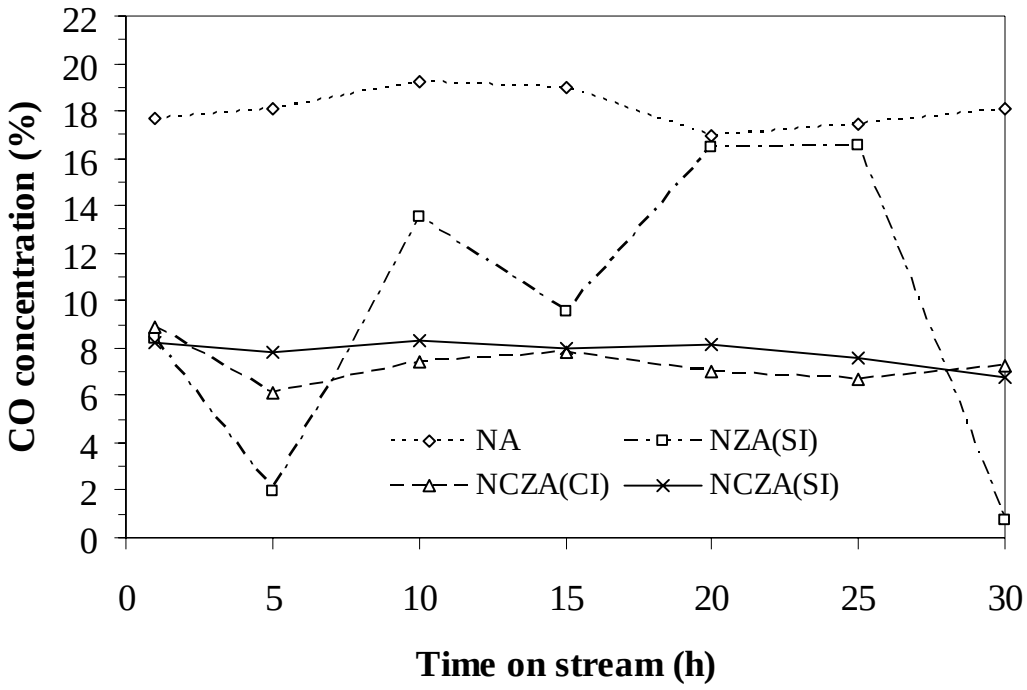

Figure 4.21 – CO concentration in outlet product compositions during steam methane reforming over all the Ni catalysts at 800 °C and S/C ratio of 2 for 30 h

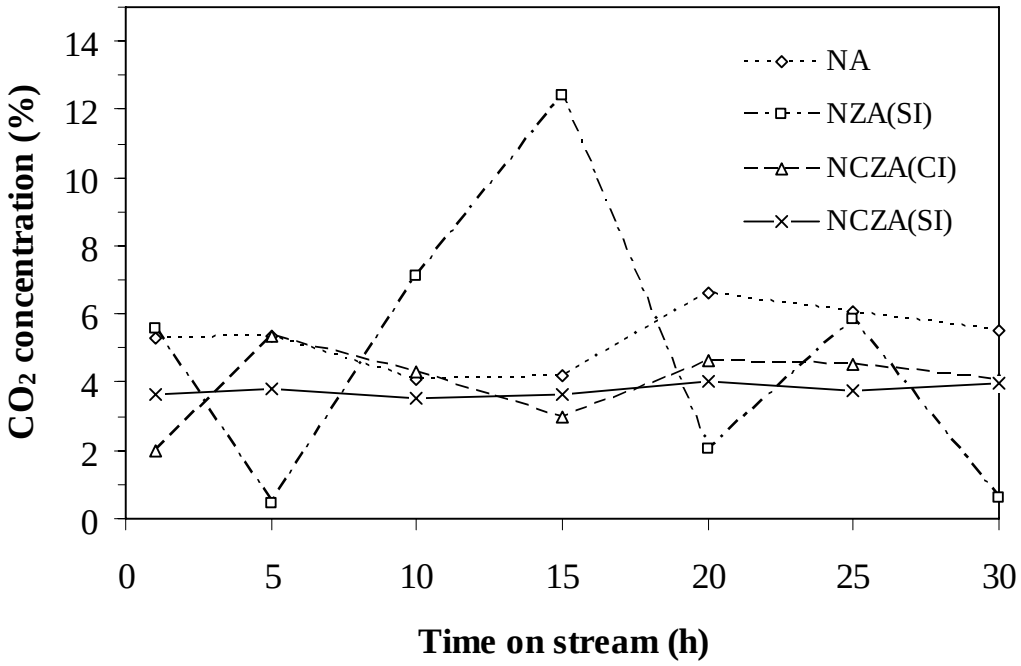

Figure 4.22 – CO_2 concentration in outlet product compositions during steam methane reforming over all the Ni catalysts at 800 °C and S/C ratio of 2 for 30 h

According to Fig. 4.21, NA yielded the highest concentration of CO (17%) over 30 h. The result is attributed to the more, continued existence of Boudouard reaction (Eq. 2.5) on NA. At T ≥730 °C, the backward reaction takes place causing the deposited carbon to react with CO_2 providing the higher CO concentration [32,33]. NCZA (CI) and NCZA (SI) provided rather low CO concentration (6–8%) in contrast to NA. The results suggested that the existence of CaO–ZrO_2 in NCZA (CI) and NCZA (SI) did not facilitate the Boudouard reaction on the surfaces of both catalysts. NZA (SI) showed the wide fluctuation in CO concentration, similar to its fluctuation in CH_4 conversion and H_2 yield. The results of CO_2 concentration revealed that the existence of water gas shift reaction on the surface of all the Ni catalysts was almost the same.

4.2.6 Catalyst deactivation

TEM images of all the spent catalysts are exhibited in Fig. 4.23. After the catalytic testing, the Ni crystal sizes in NA and NZA (SI) were significantly smaller than those of NCZA (CI) and NCZA (SI). The results are attributed to the sintering of both Ni catalysts due to the existence of CaO and ZrO_2. Zou et al. [34] found that the small amount of additives can accelerate and decelerate the sintering and transformation of γ-Al_2O_3. Thus, CaO–ZrO_2 promoter could accelerate the sintering of both Ni catalysts. However, the sintering of both Ni catalysts showed no significant effect on their activity over the period of catalytic testing in this work. NA and NZA (SI) revealed the existence of whisker carbon, whereas NCZA (CI) and NCZA (SI) did not. The non-existence of whisker carbon in NCZA (CI) and NCZA (SI) resulted from the existence of CaO and ZrO_2 in both catalysts leading to strong metal-support interaction (SMSI) between Ni active sites and CaO–ZrO_2 phases and thus inhibited the formation of whisker carbon in steam methane reforming at 800 °C. The morphology of deposited carbon on the spent catalysts is closely examined by HRTEM as shown in Fig. 4.24. HRTEM images with scale bar of 40 and 90 nm exhibited the existence of whisker carbon in NA and NZA (SI). HRTEM images with scale bar of 7 nm revealed the existence of encapsulating carbon in NA, NZA (SI) and NCZA (CI). NCZA (SI) was not affected by the formation of encapsulating carbon due to its structural characteristics. Most Ni active sites deposited on $CaZrO_{3-\delta}$ leading to the continuous supply of water molecules from $CaZrO_{3-\delta}$ sites to the Ni active sites through the connected area between them. The process of facilitation in the supply of water molecules resulted in carbon gasification inhibiting the formation of encapsulating carbon in NCZA (SI). However, although the amount of $CaZrO_{3-\delta}$ in

NCZA (CI) was comparable to that in NCZA (SI) as suggested by TPR results, the considerable amount of encapsulating carbon existed only in NCZA (CI) after catalytic testing. This result implied that the different method of impregnation affect the formation of encapsulating carbon differently and significantly.

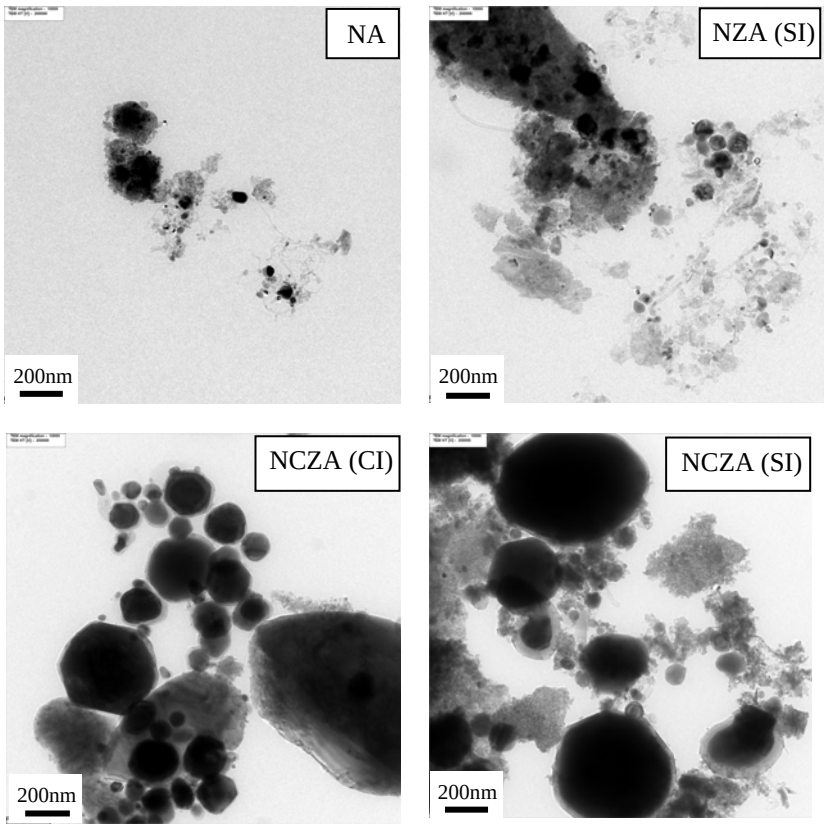

Figure 4.23 – TEM images with 200 nm scale bar of all the spent Ni catalysts

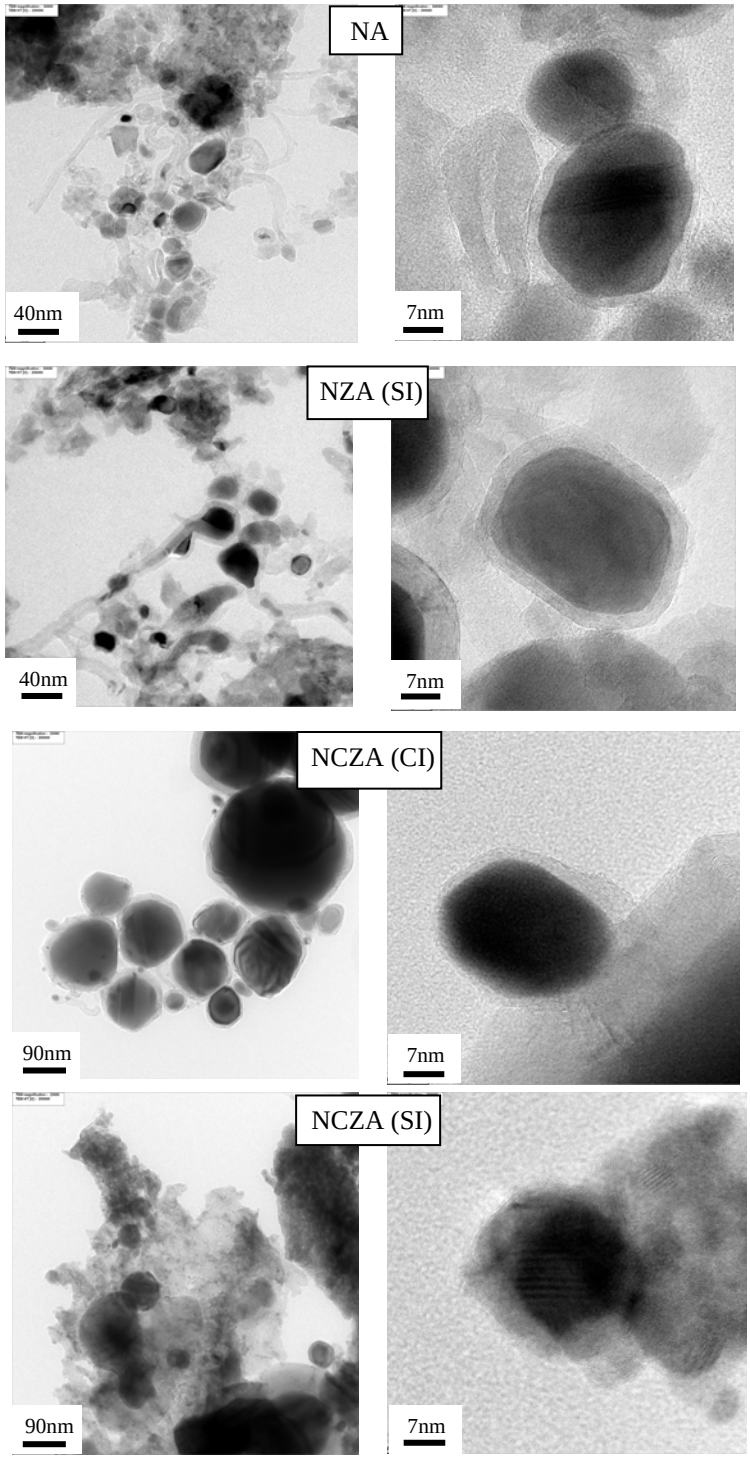

Figure 4.24 – HRTEM images with 7, 40 and 90 nm scale bars of all the spent Ni catalysts

Table 4.4 shows the total amount of carbon in all the spent catalysts using TGA in O_2 atmosphere. The order of increase in the total amount of carbon was NCZA (CI) < NCZA (SI) < NA < NZA (SI). It was noticeable that although NCZA (CI) indicated quite low total amount of carbon, its CH_4 conversion and H_2 yield dramatically dropped at the time on stream of 30 h. The results confirmed that the large amount of encapsulating carbon in NCZA (CI) was a crucial factor in its rapid deactivation [24]. NZA (SI) exhibited the largest amount of deposited carbon due to the more existence of whisker carbon as shown in Fig. 4.23 and 4.24 resulting in the marked fluctuation in the activity of NZA (SI). The reason why whisker carbon led to the fluctuation in activity was clearly explained in our previous work [31].

Table 4.4 – Total amount of carbon after catalytic testing by TGA in O_2 atmosphere

Catalysts	Total amount of carbon (mg_{carbon}/g_{cat})
NA	107
NZA(SI)	123
NCZA(CI)	5
NCZA(SI)	100

4.2.7 Relationship between the impregnation methods and catalyst performance

NCZA (CI) showed the high, steady activity for 30 h of time on stream. However, its activity rapidly dropped due to the higher amount of encapsulating carbon. The existence of encapsulating carbon was because the structural features of Ni–CaO–ZrO_2 nanocomposites (fine dispersion and close contact among NiO, CaO,

and ZrO_2) involved the appropriate characteristics of surface for the adsorption and dissociation of CH_4 molecules; however, these mechanisms competed against the adsorption and dissociation of water molecules on the nanocomposite surface. Since the mechanisms of CH_4 dominated, the carbon was accumulated on the nanocomposites resulting in the formation of encapsulating carbon on Ni–CaO–ZrO_2 nanocomposites.

For NCZA (SI), although its activity was slightly fluctuated, the relatively small amount of carbon with the non-existence of encapsulating carbon was observed. The slight fluctuation in its activity is attributed to the imbalance between carbon deposition and gasification on its surface. In other words, its activity decreases because the carbon deposition rate (CH_4 dissociation) is higher than the carbon gasification rate (the supply of water from $CaZrO_{3-\delta}$ sites to Ni active sites through their connected area). For the range of steady activity, the carbon deposition rate is comparable to the carbon gasification rate.

In comparison with our previous work—the catalyst (N55CZA) was prepared by sequential impregnation at the same composition, except that it was calcined at 600 °C after first impregnation stage for the deposition of CaO–ZrO_2 on γ-Al_2O_3 and examined in steam methane reforming at 600 °C, the performance of N55CZA differed from that of NCZA (SI). N55CZA showed the more existence of whisker carbon, whereas NCZA (SI) hardly revealed that of whisker carbon. In addition, N55CZA provided the higher H_2 yield than NCZA (SI). The different results implied that a reaction rate in steam methane reforming over (CaO–ZrO_2)-modified Ni/γ-Al_2O_3 catalyst calcined at 600 °C differed from that at 800 °C.

4.3 Effect of variation in $CaO–ZrO_2$ loading percentage

4.3.1 Results

4.3.1.1 Phase analysis

XRD patterns of all the Ni catalysts after calcination at 700 °C for 1 h are shown in Fig. 4.25. All the XRD patterns indicated the existence of α-Al_2O_3 and NiO phases. All the ($CaO–ZrO_2$)-modified Ni catalysts revealed $CaZr_4O_9$ peaks at 2θ = 30.5 and 50.5°. The intensity of $CaZr_4O_9$ peaks increased with increasing of $CaO–ZrO_2$ content from 5 to 15 wt%. The $CaZr_4O_9$ peaks showed amorphous characteristic.

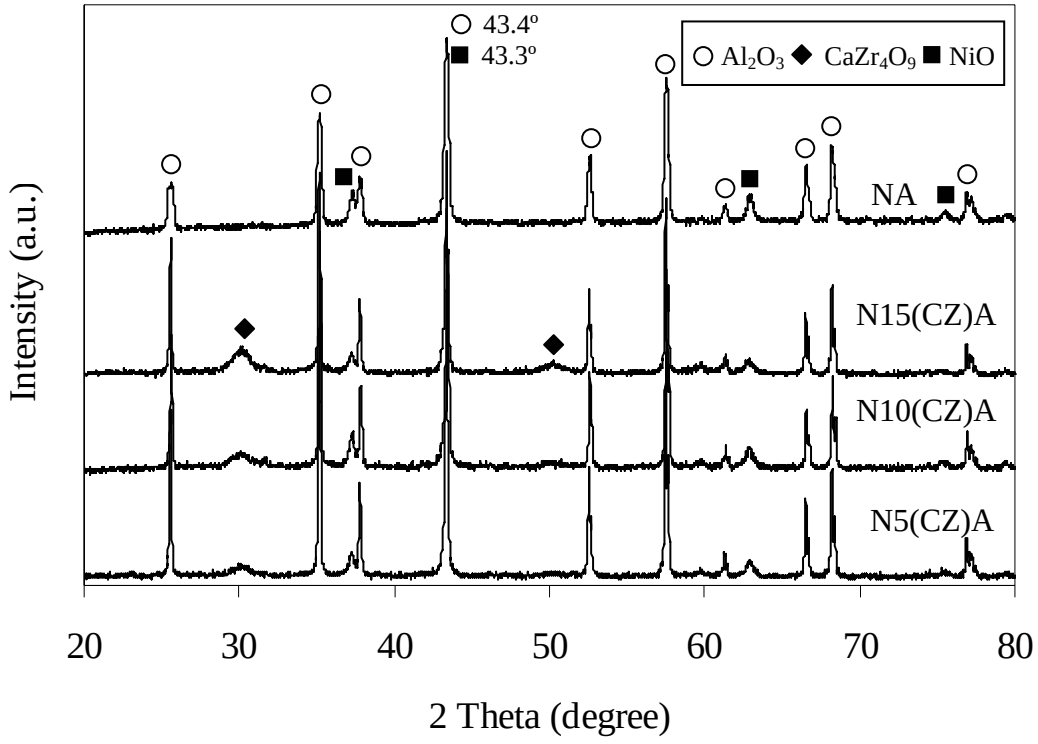

Figure 4.25 – XRD patterns of all the unmodified and modified Ni catalysts after calcination

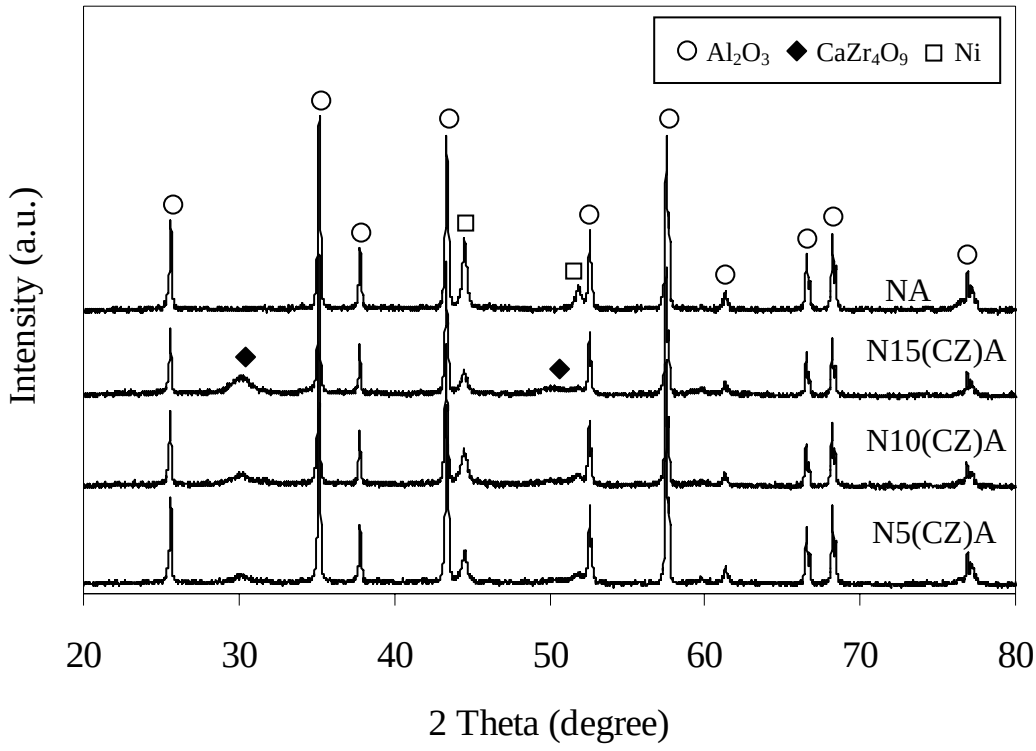

Figure 4.26 – XRD patterns of all the unmodified and unmodified Ni catalysts after reduction

Fig. 4.26 exhibits XRD patterns of all the Ni catalysts after reduction at 700 °C for 1 h. All the XRD patterns showed the phases of metallic Ni and α-Al_2O_3. The intensity of $CaZr_4O_9$ peaks increased with increasing the amount of CaO–ZrO_2 in the same way as the XRD patterns of all the Ni catalysts after calcination. However, we noticed that the intensity of $CaZr_4O_9$ peaks for the reduced Ni catalysts was lower than that for the calcined Ni catalysts. From the observation, it is noteworthy to determine the crystallite sizes of $CaZr_4O_9$ peaks at $2\theta = 30.5°$ for all the modified Ni catalysts both after the calcination and reduction stages. The results of $CaZr_4O_9$ and Ni crystallite sizes calculated from the Scherrer equation (Eq. 3.4) were shown in Table 4.5. In addition, the crystallite sizes of metallic Ni for all the Ni catalysts were indicated in Table 4.5.

Table 4.5 – Crystal sizes of metallic Ni and $CaZr_4O_9$ from calculation by Scherrer equation

Catalysts	Metallic Ni (nm) at 2θ = 44º, plane (111)	$CaZr_4O_9$ (nm) at 2θ = 30.5º		
		After calcination	After reduction	Change of crystal sizes (%)
N5(CZ)A	19	4.3	4.1	-4.7
N10(CZ)A	16	4.6	4.1	-10.9
N15(CZ)A	15	5.6	4.6	-17.9
NA	26	–	–	–

The results exhibited the decrease of metallic Ni crystallite sizes, when the total amount of $CaO–ZrO_2$ increased from 5 to 15 wt% in the modified Ni catalysts. The unmodified Ni catalyst, NA, showed the largest crystallite size of metallic Ni. In addition, when the total amount of $CaO–ZrO_2$ in the modified Ni catalysts both after calcination and reduction increased, the crystallite sizes of $CaZr_4O_9$ increased. The crystallite sizes of $CaZr_4O_9$ in the modified Ni catalysts after calcination were larger than that after reduction.

4.3.1.2 Textural characteristics

BET surface area of all the calcined and reduced Ni catalysts is indicated in Fig. 4.27. Both after calcination and reduction, the surface area of NA was the smallest in comparison to the modified Ni catalysts. After the addition of $CaO–ZrO_2$ into the unmodified Ni catalysts from 5 to15 wt%, the surface areas of

the modified Ni catalysts increased. The surface area of all the calcined Ni catalysts decreased after the reduction stage. The percentage changes of surface area in all the calcined Ni catalysts after the reduction stage were shown in Fig. 4.28. N5(CZ)A with the low total amount of $CaO–ZrO_2$ showed the most negative–percentage change in BET surface area after the reduction stage. When the total amount of $CaO–ZrO_2$ in the modified Ni catalysts increased up to 10 and 15 wt%, the percentage changes being negative in their BET surface areas were almost equal. It is interesting that the percentage changes in the surface areas of N10(CZ)A and N15(CZ)A were almost identical with NA.

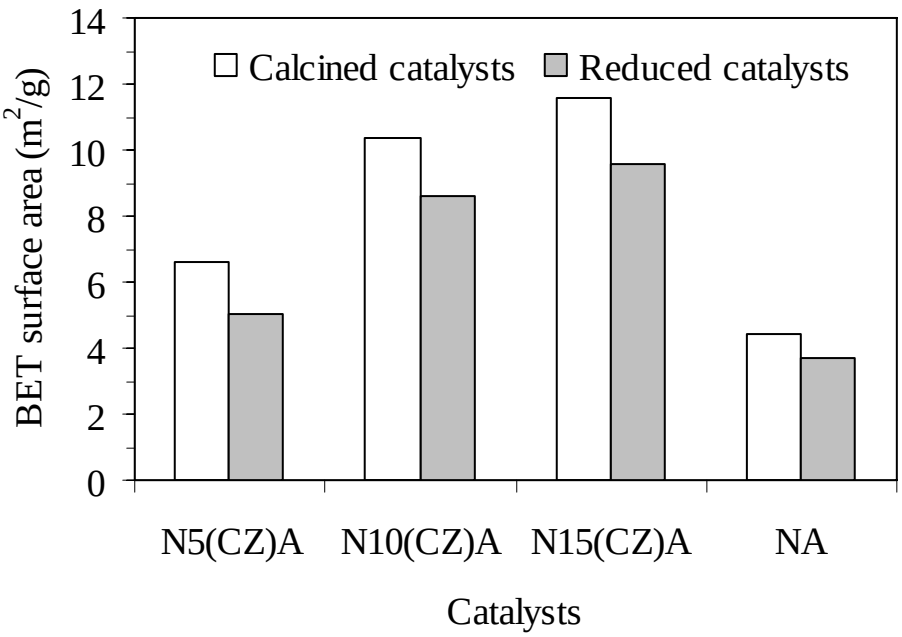

Figure 4.27 – BET surface area of all the calcined and reduced Ni catalysts

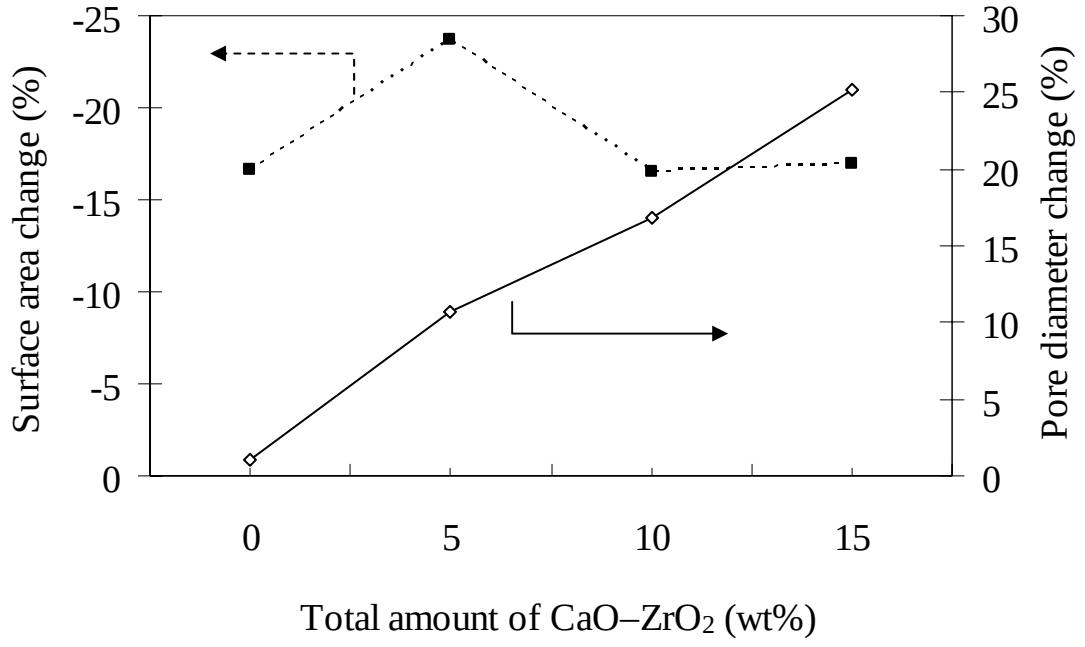

Figure 4.28 – Percentage changes in BET surface area and average pore diameters of all the calcined Ni catalysts after reduction stage at 700 ºC for 1 h

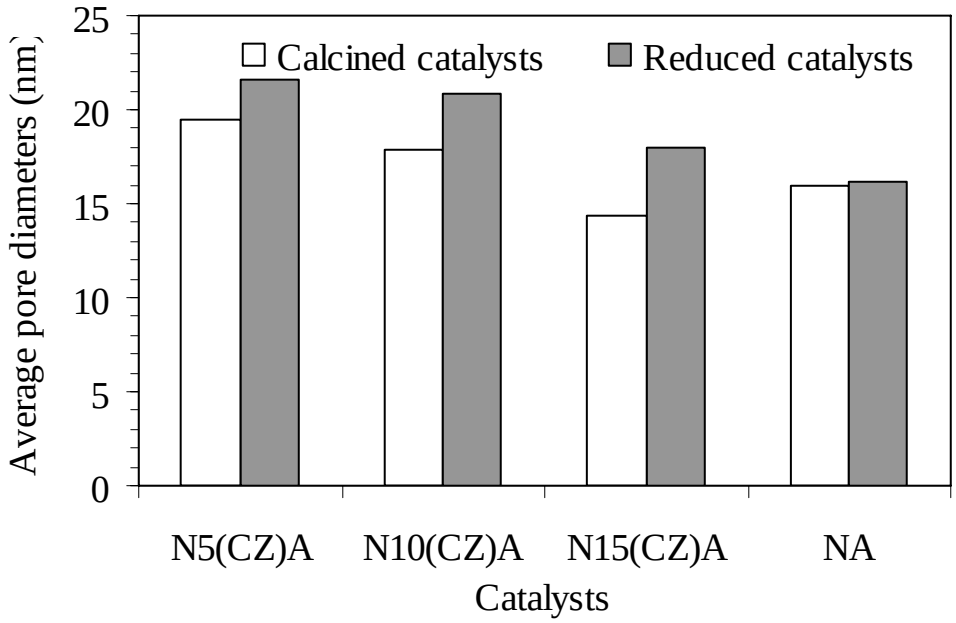

Figure 4.29 – Average pore diameters of all the calcined and reduced Ni catalysts

Fig. 4.29 shows the average pore diameters of all the Ni catalysts after calcination and reduction. The average pore diameters of the modified Ni catalysts were smaller when the total amount of $CaO–ZrO_2$ increased from 5 to 15 wt%. After calcination, N15(CZ)A showed the smallest pore diameter in comparison to the other Ni catalysts. The percentage changes in average pore diameters of all the calcined Ni catalysts after reduction stage were indicated in Fig. 4.28. The average pore diameters of all the calcined Ni catalysts were smaller than those of all the reduced Ni catalysts. The percentage change in average pore diameter of NA was insignificant after the reduction stage. On the other hand, the percentage changes in average pore diameters of the ($CaO–ZrO_2$)-modified Ni catalysts increased with increasing amount of $CaO–ZrO_2$ from 5 to 15 wt%.

4.3.1.3 Temperature–programmed reduction (TPR)

TPR profiles of all the Ni catalysts are indicated in Fig. 4.30. NA consumed H_2 in three ranges of temperature, i.e., 420–580, 580–680 and 680–950 °C. All the ($CaO–ZrO_2$)-modified Ni catalysts showed three–temperature ranges of approximately 420–550, 550–710, and 650–740 °C, depending on the reducibility of each catalyst. It is interesting that the highest H_2 consumption range (~550–710 °C) began at almost the same temperature of 540, 570, and 555 °C for N5(CZ)A, N10(CZ)A, and N15(CZ)A, respectively. In addition, the H_2 consumption finished at the different temperature for each the modified Ni catalyst, i.e., at approximately 650, 700, and 680 °C for N5(CZ)A, N10(CZ)A, and N15(CZ)A, respectively. When the total amount of ($CaO–ZrO_2$) increased from 5 to 15 wt%, the end points of H_2 consumption were extended to the higher temperature. Nevertheless, N15(CZ)A

showed the slightly lower end-temperature than N10(CZ)A. In addition to the lower end-temperature of N15(CZ)A, the highest H_2 consumption was in the temperature range of 420–550 °C.

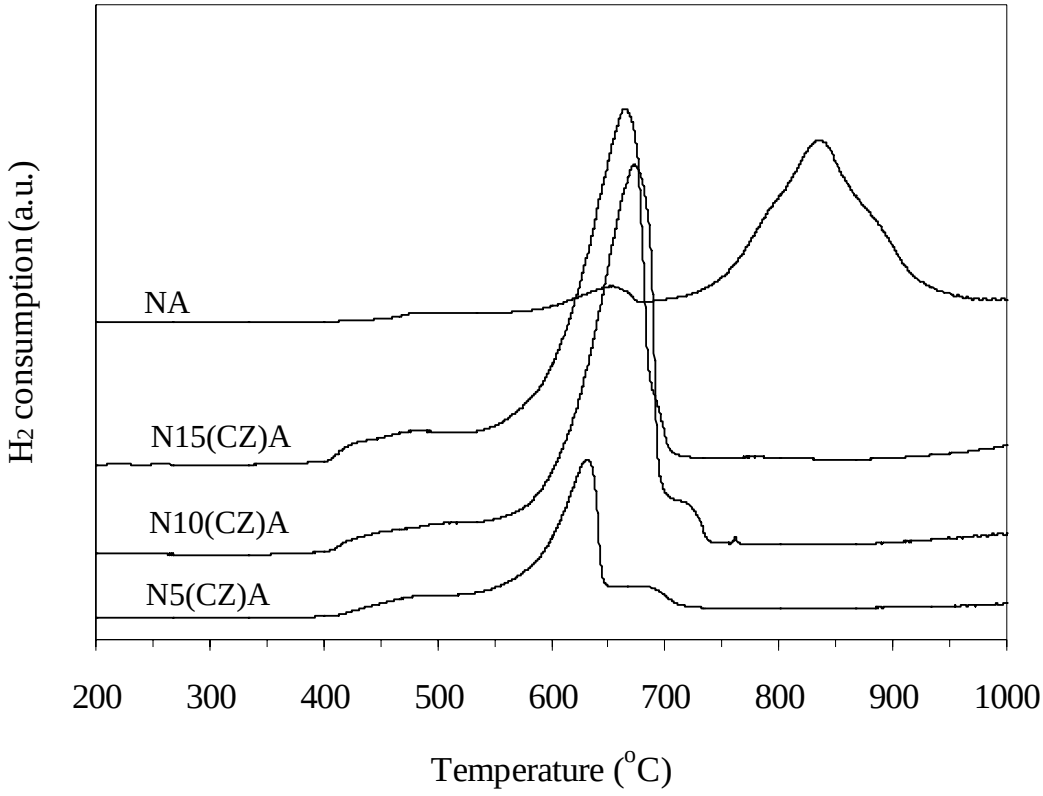

Figure 4.30 – TPR profiles of all the unmodified and modified Ni catalysts

4.3.1.4 Catalytic performance

CH_4 conversion during steam methane reforming over all the Ni catalysts for 30 h is shown in Fig. 4.31. NA and N5(CZ)A showed the wide fluctuation in CH_4 conversion, whereas N10(CZ)A and N15(CZ)A displayed the rather constant conversion of CH_4. N15(CZ)A provided the highest and most continuous conversion of CH_4 (averagely 70%). The fluctuation in CH_4 conversion

decreased when the total amount of $CaO–ZrO_2$ in the modified Ni catalysts increased from 5 to 15 wt%. NA showed the highest fluctuation and lowest conversion of CH_4.

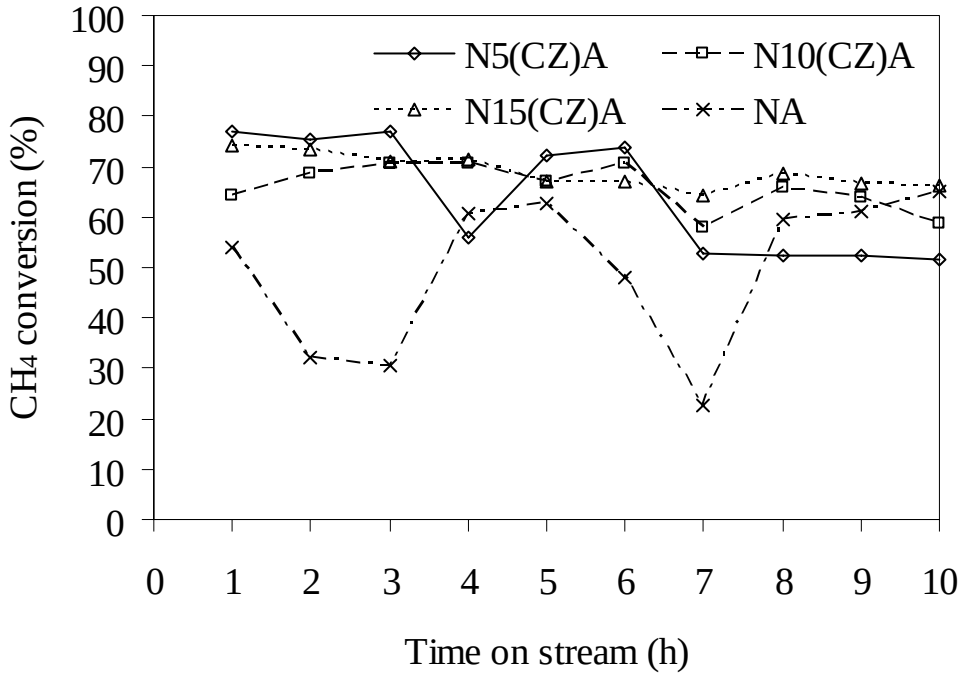

Figure 4.31 – CH_4 conversion during steam methane reforming over all the Ni catalysts at 700 °C and S/C ratio of 2 for 10 h

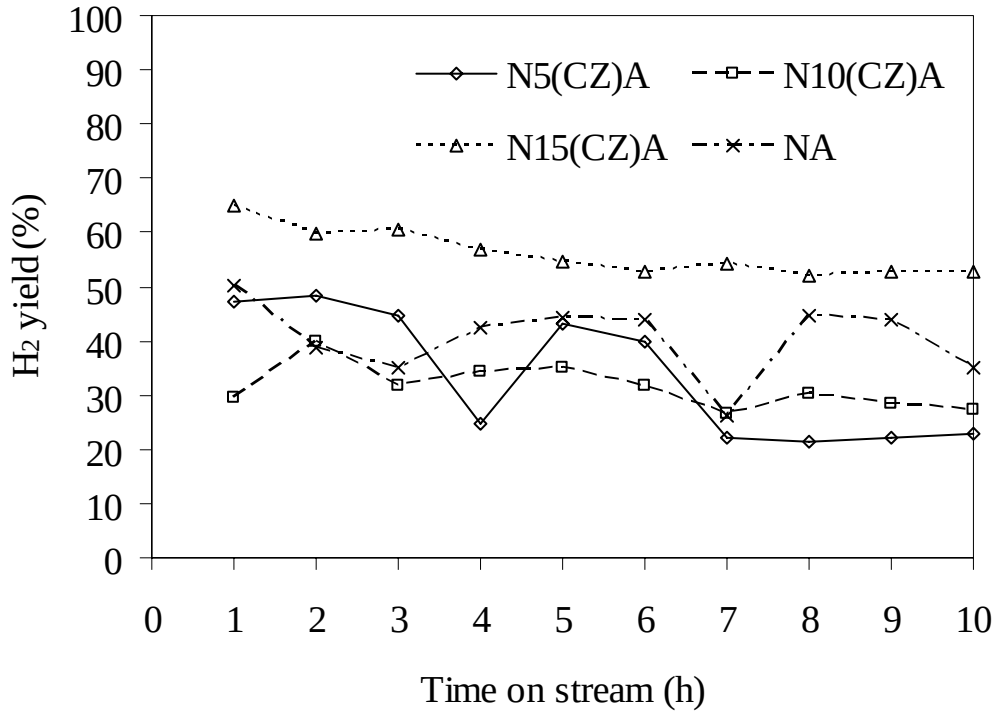

Figure 4.32 – H_2 yield during steam methane reforming over all the Ni catalysts at 700 °C and S/C ratio of 2 for 10 h

H_2 yield during steam methane reforming over all the Ni catalysts for 30 h is displayed in Fig. 4.32. Obviously, N15(CZ)A provided the highest yield of H_2 (~55–65%) in comparison with the other Ni catalysts (~22–50% H_2 yield). NA and N5(CZ)A indicated the high fluctuation in H_2 yield similar to their fluctuation in CH_4 conversion. It is interesting that although the CH_4 conversion of N10(CZ)A was almost identical to that of N15(CZ)A, N10(CZ)A noticeably provided the lower H_2 yield than N15(CZ)A.

Fig. 4.33 shows the CO concentrations in the outlet products during steam methane reforming over all the Ni catalysts. N10(CZ)A and N15(CZ)A provided the high CO concentration (~12%), whereas NA and N5(CZ)A provided low

CO concentration (~4–5%). N15(CZ)A showed the unsteady concentration of CO in contrast to the other Ni catalysts.

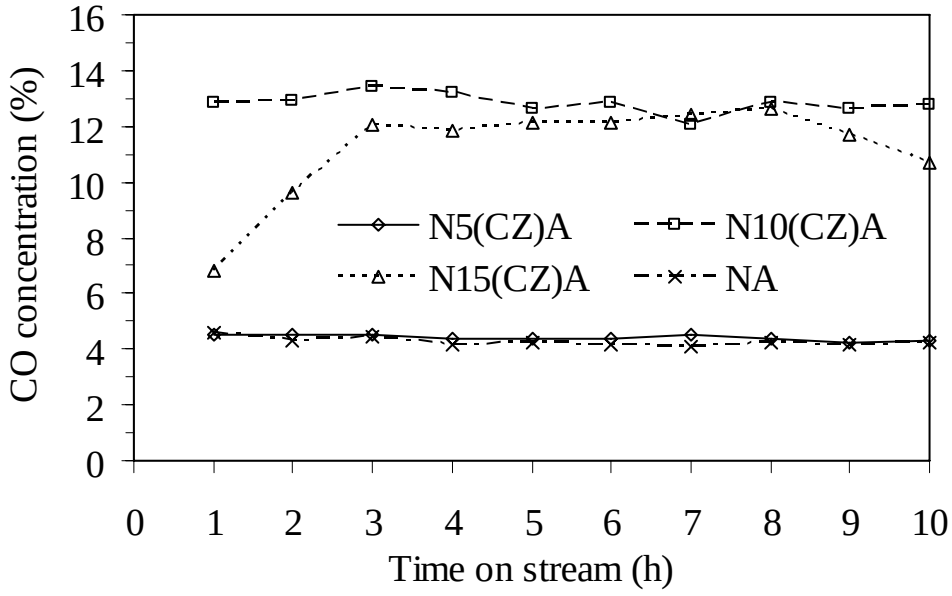

Figure 4.33 – CO concentration in the outlet products during steam methane reforming over all the Ni catalysts at 700 °C and S/C ratio of 2 for 10 h

The concentration of CO_2 in the outlet product compositions during steam methane reforming over all the Ni catalysts is shown in Fig. 4.34. CO_2 concentrations in the outlet products of N10(CZ)A and N15(CZ)A was higher than that of NA and N5(CZ)A, which was similar to the CO concentration results. It is interesting that although CO concentration of NA was identical to that of N5(CZ)A, CO_2 concentration of NA was slightly higher than that of N5(CZ)A. In comparison to N10(CZ)A, N15(CZ)A showed the lower CO concentration, while provided the higher CO_2 concentration.

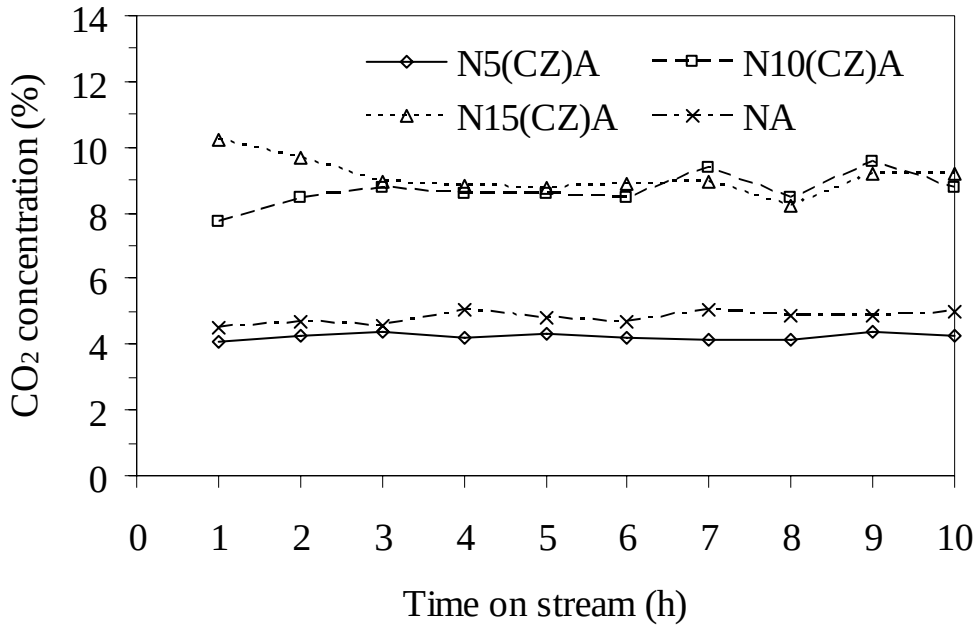

Figure 4.34 – CO_2 concentration in the outlet products during steam methane reforming over all the Ni catalysts at 700 °C and S/C ratio of 2 for 10 h

4.3.1.5 Catalyst deactivation

HRTEM images of all the spent catalysts are shown in Fig. 4.35. The HRTEM images indicated the difference between the unmodified and ($CaO–ZrO_2$)-modified Ni catalysts. The unmodified Ni catalysts, NA, indicated the large particle size of α-Al_2O_3 support. In addition, NA exhibited the existence of large metallic Ni crystallite size, according to the calculation by Scherrer equation. The amount of $CaZrO_3$ nanoparticles was increased with increasing the total amount of $CaO–ZrO_2$. The agglomeration and sizes of calcium zirconate nanoparticles were also increased with increasing $CaO–ZrO_2$ amount.

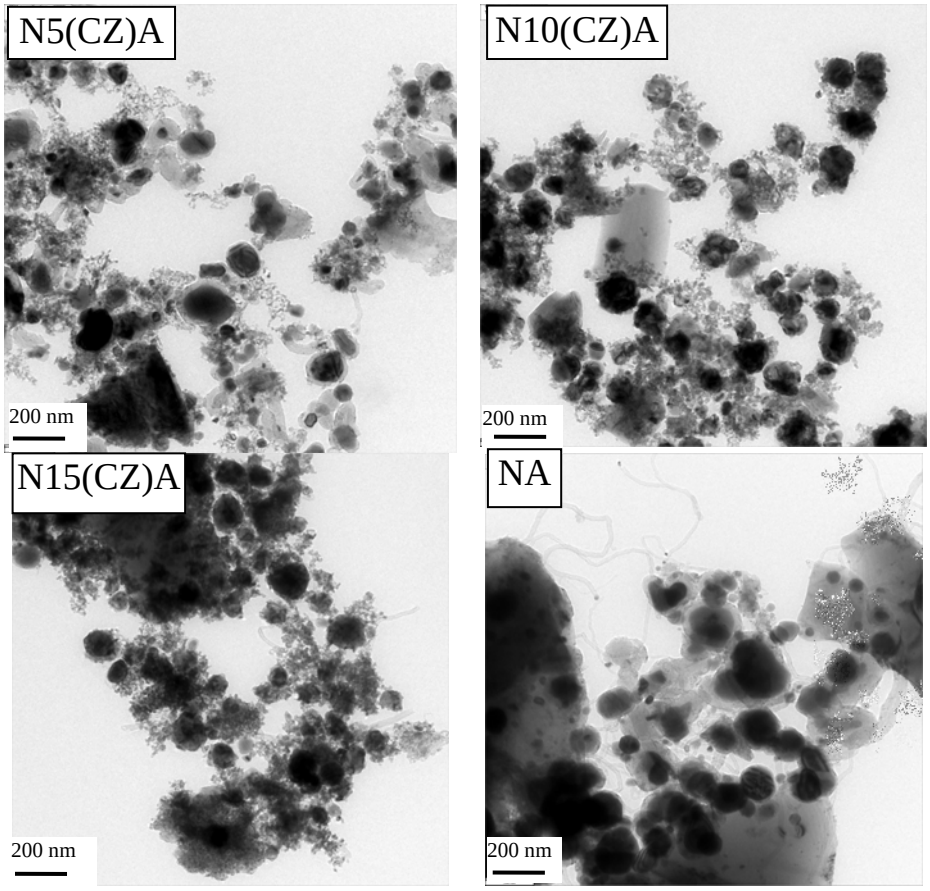

Figure 4.35 – HRTEM images with 200 nm scale bar of all the spent Ni catalysts

Fig. 4.36 shows HRTEM images (7–90 nm scale bars) of all the spent catalysts to observe the morphology of deposited carbon. For the scale bars of 40 and 90 nm, NA (the unmodified catalyst) indicated the more existence of whisker carbon whereas the other catalysts (the modified catalysts) did not indicate the existence. In the case of HRTEM images with 7-nm scale bar, each spent Ni catalyst exhibited the different morphology of deposited carbon. N5(CZ)A revealed the considerable existence of whisker carbon whereas N10(CZ)A did not indicated the existence of any species of deposited carbon. N15(CZ)A showed the existence of encapsulating carbon. NA exhibited the existence of both encapsulating and whisker carbon.

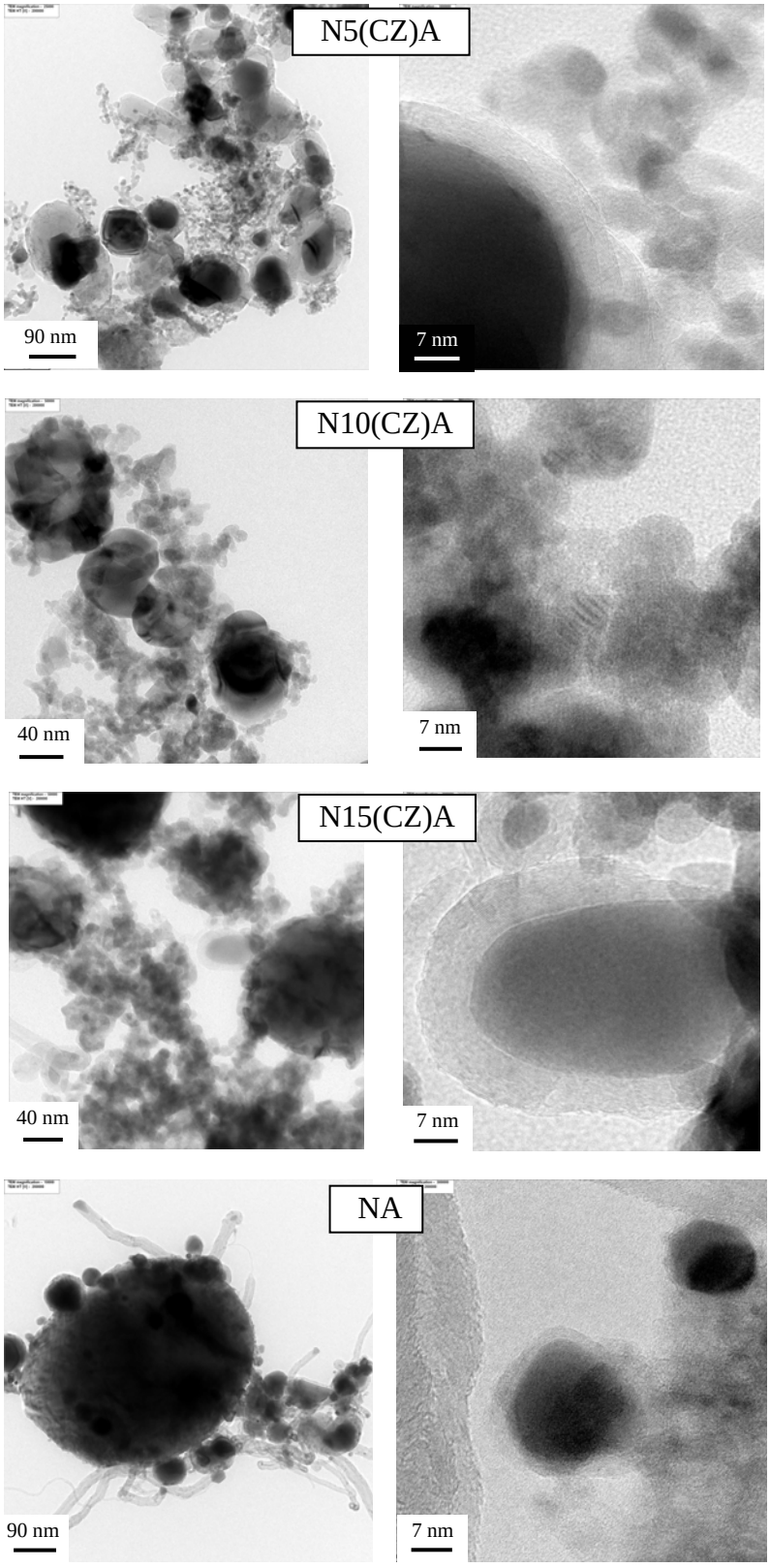

Figure 4.36 – HRTEM images with 7-, 40- and 90-nm scale bars of all the spent Ni catalysts

Table 4.6 indicated the total amount of carbon and nickel oxidation in all the spent catalysts. The order of increase in the total amount of carbon in the spent Ni catalysts was N10(CZ)A ≈ N15(CZ)A < NA < N5(CZ)A. In comparison to NA, N5(CZ)A showed the highest amount of carbon deposition, whereas N10(CZ)A and N15(CZ)A indicated the smaller amount of carbon deposition. In the case of the oxidation of nickel in all the spent catalysts, the order of increasing nickel oxidation of all the spent catalysts was N10(CZ)A < N15(CZ)A < N5(CZ)A < NA.

Table 4.6 – Total amount of carbon and nickel oxidation in all the spent Ni catalysts determined by thermo-gravimetric analysis (TGA) in O_2 atmosphere

Catalysts	Total amount of carbon ($mg_{carbon}/g_{cat.}$)	Oxidation of nickel (%)
N5(CZ)A	32.6	0.34
N10(CZ)A	6.6	0.03
N15(CZ)A	6.9	0.16
NA	13.4	0.37

4.3.2 Discussion

4.3.2.1 Effect of $CaO–ZrO_2$ loading percentage on physico–chemical properties of catalyst

The ($CaO–ZrO_2$)-modified Ni catalysts indicated the increasing sizes of $CaZr_4O_9$ peaks (2θ = 30.5 and 50.3º) when the total amount of $CaO–ZrO_2$ increased from 5 to 15 wt% as shown in Fig. 4.25. In our estimation, the prepared catalysts with 0.5 mole ratio of CaO/ZrO_2 should also exhibit $CaZrO_3$ phase since the

phase diagram of $CaO–ZrO_2$ suggested that $CaZrO_3$ was a stable phase at that composition [16]. The undetectable phase of $CaZrO_3$ by XRD is attributed to its crystallite being under the detection limit of XRD (~3–5nm) [6]. Although XRD was unable to detect $CaZrO_3$ phase, the decreasing size of $CaZr_4O_9$ peak ($2\theta = 30.5^o$) in the modified Ni catalysts after the reduction stage implied that the $CaZrO_3$ phase existed in the modified Ni catalysts. In other words, $CaZr_4O_9$ remained stable under H_2 atmosphere at high temperature; thus, the crystallite of $CaZr_4O_9$ should be unchanged. Since cubic $CaZrO_3$ displays its diffraction line at $2\theta = 31.4$ and 50.7^o which are close to the diffraction line of $CaZr_4O_9$, it is believed that the decreasing sizes of $CaZr_4O_9$ peaks originated from the release of oxygen atoms in $CaZrO_3$ structure during the reduction stage leading to the decrease in size of $CaZr_4O_9$ peaks. In addition to the confirmation of $CaZrO_3$ existence from the decreasing size in $CaZr_4O_9$ diffraction peaks, TPR results (Fig. 4.30) strongly confirmed the existence of $CaZrO_3$ phase. TPR profiles of the modified Ni catalysts showed the clear evidence of H_2 consumption from ~550 to 710 ^oC which is the temperature range of reaction between oxygen atoms in $CaZrO_3$ phase and H_2 molecules to form H_2O molecules. The amount of H_2 consumption in the above temperature range is comparable to that of the modified Ni catalysts in our previous work [31,35]. However, the unmodified catalyst, NA, indicated the consumption of H_2 at the peak temperature of approximately 670 ^oC which was the same temperature rage of $CaZrO_3$ reduction. The H_2 consumption of NA is attributed to the uptake of H_2 by NiO specie strongly reacting with α-Al_2O_3 [36].

From Table 4.5, the crystallite size of the metallic Ni was decreased with increasing total amount of $CaO–ZrO_2$ from 5 to 15 wt%. The decreasing crystallite size of the metallic Ni was resulted from the increase of the $CaO–ZrO_2$

amount in the Ni catalysts leading to the fine dispersion of NiO clusters. In addition, the crystallite size of calcium zirconate ($CaZr_4O_9$, $CaZrO_3$) was increased when the total amount of $CaO–ZrO_2$ increased (the meaning of calcium zirconate after this explanation covered the phases of $CaZr_4O_9$ and $CaZrO_3$). The result may be attributed to the occurrence of solid state sintering of the nearby calcium zirconate particles.

The percentage change of the $CaZr_4O_9$ crystallite size was increased from -4.7 to -17.9% with increasing $CaO–ZrO_2$ amount. The negative increase confirmed the increase of the oxygen vacancies with increasing $CaO–ZrO_2$ in the modified Ni catalysts. The unmodified Ni catalysts (NA) showed the largest crystallite size of metallic Ni due to the low surface area of unmodified α-Al_2O_3 support (7.85 m^2/g). The small area with low porosity of α-Al_2O_3 caused the non-uniformity in NiO dispersion and larger Ni crystallite.

XRD and TPR results proved that the ($CaO–ZrO_2$)-modified Ni catalysts at 0.5 mole ratio of CaO/ZrO_2 consisted of the co-existence of $CaZr_4O_9$ and $CaZrO_3$ particles. The co-existence of two phases differed from the phase diagram of $CaO–ZrO_2$ suggesting that only $CaZrO_3$ would be formed at 0.5 mole ratio of CaO/ZrO_2. The discrepancy is attributed to the intrinsic character of impregnation method that is unable to uniformly disperse CaO and ZrO_2 particles on α-Al_2O_3 surface [6]. Therefore, the impregnation process created the two phases of $CaZr_4O_9$ and $CaZrO_3$ corresponding to the two phases demonstrating on left side of 50 mole % CaO of the phase diagram [16].

Considering the surface area of all the prepared Ni catalysts, their surface area increased when the total amount of $CaO–ZrO_2$ increased. The result is attributed to the increasing formation of calcium zirconate nanoparticles ($CaZr_4O_9$ and $CaZrO_3$) when the $CaO–ZrO_2$ amount increased. The increasing formation leads to the

increase in the surface areas of the modified Ni catalysts. Interestingly, after the reduction stage the surface area of all the Ni catalysts in this work decreased whereas that in our previous work increased [31]. The different results are attributed to the phase of Al_2O_3 support between α phase with no porosity and γ phase with high porosity. The results mean that although the Ni catalysts were prepared by the same method of sequential impregnation, the formed phases of metallic Ni and CaO–ZrO_2 promoter were deposited and/or dispersed in the significantly different ways on the surface of α- and γ-Al_2O_3. In the case of α-Al_2O_3 support, since there is almost no pore in α-Al_2O_3, all the calcium zirconate nanoparticles were formed individually and dispersed together with α-Al_2O_3. The features of co-existence of these phases are responsible for the deposition of NiO clusters on calcium zirconate and α-Al_2O_3 particles after the stages of impregnation and then calcination of the Ni catalyst. During the reduction stage, oxygen atoms at the deposited NiO clusters and the $CaZrO_3$ surface reacted with H_2 molecules leading to the release of the reacting oxygen atoms in the form of H_2O molecules. The release of oxygen atoms created the large amount of oxygen vacancies and thus large pores owing to the combination of oxygen vacancies. The formation of large pores resulted in the decrease in the surface area of the calcined Ni catalysts.

In the case of using γ-Al_2O_3 support, it is believed that the CaO reacted with ZrO_2 to form calcium zirconate nanoparticles and dispersed in the pores of γ-Al_2O_3 support [31]. The dispersion of calcium zirconate in pores involved the deposition of NiO clusters on the surface of calcium zirconate in the pores and at the wall of pores after the calcination stage. When all the Ni/γ-Al_2O_3 catalysts were reduced, oxygen atoms at the surface of the deposited NiO clusters and the $CaZrO_3$ particles reacted with H_2 molecules leading to the release of oxygen atoms.

Consequently, only some parts of the NiO clusters and the $CaZrO_3$ particles were exposed H_2 gas during the reduction stage since the parts attached to the walls of pores were unexposed to H_2 gas. The results led to the formation of nanopores involving the increase in the surface area of all the Ni/γ-Al_2O_3 catalysts.

Fig. 4.29 displays the increase in percentage change of pore diameters of the calcined Ni catalysts when the CaO–ZrO_2 amount increases from 5 to 15 wt%. The results implied that the more existence of $CaZrO_3$ particles led to the increasing formation of oxygen vacancies. The increasing pore diameters are in agreement with the percentage change in $CaZr_4O_9$ crystallite sizes — calcium zirconate crystallite sizes — as shown in Table 4.5.

Obviously, when the CaO–ZrO_2 amount increased, the percentage changes in the pore diameters of all the Ni catalysts increased linearly, while the percentage changes in their surface area were non-linear. N5(CZ)A had the percentage change in surface area of - 25% during the reduction stage. The result is attributed to two key factors: (1) the low total amount of CaO–ZrO_2 (5 wt%), and (2) the catalyst reduction at 700 °C for 1 h. In the case of the first factor, the amount of the formed calcium zirconate particles was quite low at 5 wt % CaO–ZrO_2; consequently, most of NiO clusters were deposited on α-Al_2O_3 surface resulting in the low dispersion and thus large size of NiO clusters. For the latter factor, three oxides in N5(CZ)A were reduced at 700 °C for 1 h (Fig. 4.30): (1) NiO at bulk (400–550 °C), (2) $CaZrO_3$ (550–650 °C), and (3) NiO strongly reacting with α-Al_2O_3 (650–720 °C). The amount of reduced NiO in N5(CZ)A was higher than N10(CZ)A and N15(CZ)A. The highest amount of NiO reduced at 650–720 °C generated the large amount of pores resulting in the decrease in the surface area of N5(CZ)A at -25%.

According to the results of percentage changes in the surface area and pore diameters during the reduction stage, they implied that the $CaO–ZrO_2$ amount in the Ni catalysts significantly influenced their characteristics: (1) the phases of oxide which were formed, (2) the amount of each oxide which was reduced, and the reduction temperature range of each oxide.

TPR profiles (Fig. 4.30) revealed the reduced oxides and the amount of reduced oxides. NA exhibited three–reduction bands at 420–580, 580–680, and 680–950 °C corresponding to the reduction of bulk NiO, NiO strongly interacting with α-Al_2O_3, and $NiAl_2O_4$, respectively [37,38]. It is interesting that $NiAl_2O_4$ phase was undetected by XRD, whereas it was detected by TPR. The limited capability for detecting $NiAl_2O_4$ is attributed to the nanometer crystallites of $NiAl_2O_4$ being in the detection limit of XRD (<3–5 nm). The ($CaO–ZrO_2$)-modified Ni catalysts indicated three–reduction bands approximately at 420–550, 550–710, and 650–740 °C which are the reduction bands of bulk NiO, $CaZrO_3$, and NiO strongly interacting with α-Al_2O_3, respectively [21,31,35]. The TPR profiles of all the ($CaO–ZrO_2$)-modified Ni catalysts did not show the reduction band of $NiAl_2O_4$. The results implied that the existence of calcium zirconate in the modified Ni catalysts inhibited the formation of $NiAl_2O_4$ phase. The increasing amount of H_2 molecules were consumed by bulk NiO as the $CaO–ZrO_2$ amount increased. The increasing consumption of H_2 molecules resulted from the small and well-dispersed NiO clusters on the calcium zirconate particles leading to the easier and larger amount of reduction. Therefore, the addition of $CaO–ZrO_2$ to the Ni catalysts can enhances the structural characteristics, for example surface area and pore diameters, of the Ni catalysts by the formation of calcium zirconate.

When the $CaO–ZrO_2$ amount in the Ni catalysts increased, the starting and finishing temperatures of H_2 consumption showed the uncertain behavior. When the $CaO–ZrO_2$ amount in the Ni catalysts increased from 5 to 10 wt%, the starting temperature of H_2 consumption shifted from 540 to 570 °C and the finishing temperature of that shifted from 650 to 700 °C. The noticeable shift in temperatures is directly related to the increase in the $CaZrO_3$ crystallite sizes from 4.3 to 4.6 nm (Table 4.5) resulting from the increase in the $CaO–ZrO_2$ amount in the Ni catalysts. In other words, the increasing $CaZrO_3$ crystallite size leads to the higher stability and the shift of H_2 consumption to the higher temperature range. The amounts of H_2 consumption of $CaZrO_3$ were also increased as the $CaO–ZrO_2$ amount increased from 5 to 10 wt%. The results were related to the increasing formation of $CaZrO_3$ particles with increasing $CaO–ZrO_2$ as confirmed by HRTEM images (Fig. 4.35 and 4.36).

However, the starting and finishing temperatures decreased to 555 and 680 °C, respectively, when the $CaO–ZrO_2$ amount in the Ni catalyst increased up to 15 wt%. The results are attributed to the stability of large $CaZrO_3$ particle size. Table 4.5 shows that $CaZr_4O_9$ crystallite of N15(CZ)A (5.6 nm) was larger than that of N10(CZ)A and N15(CZ)A (4.6 and 4.3 nm, respectively). Since H_2 molecules reacted with the $CaZrO_3$ particles only on the surface during the reduction process, the oxygen vacancies were formed only at the surface of large $CaZrO_3$ particles, but in every part of small $CaZrO_3$ particles. Therefore, when the $CaO–ZrO_2$ amount increased to 15 wt% (N15(CZ)A), the formation of oxygen vacancies occurred only at the surface of $CaZrO_3$ particles. The results explained the shift of H_2 consumption peak to the lower temperature range and lower H_2–consumption peak of $CaZrO_3$ in N15(CZ)A, compared to N10(CZ)A. Interestingly, the TPR profiles (Fig. 4.30) indicate the decreasing amount of NiO strongly interacting with α-Al_2O_3 with

increasing the $CaO–ZrO_2$ amount. The results implied that the modification of α-Al_2O_3 surface with $CaO–ZrO_2$ prevented the strong interaction between NiO and α-Al_2O_3. The TPR results confirmed that the amount and size of CaZrO3–perovskite particles strongly influenced the behavior of reduction of the modified Ni catalysts.

4.3.2.2 Effect of $CaO–ZrO_2$ loading percentage on catalyst performance

The wide fluctuation in CH_4 conversion of NA and N5(CZ)A (Fig.4.31) are attributed to the more existence of filamentous (whisker) carbon as shown in Fig. 4.35 and 4.36. The existence of filamentous carbon was the major cause of plugging in reactor resulting in pressure drop (the dramatic drop in outlet flow rate). As a result of the dramatic drop, CH_4 conversion, which was obtained from the calculation of eq. (3.3), was also decreased significantly. It should be noted that the amount of Ni catalysts used in this work was low enough (100 mg) to make its inlet pressure increased until the particles of Ni catalysts separated. As a result of the separation of catalyst particles, the filamentous carbon no longer covered the Ni active sites and returned to be active in the SMR reaction. The wide fluctuation in this work was the same as that in our previous work [31,35]. The less fluctuation in CH_4 conversion and higher CH4 conversion were observed with increasing the $CaO–ZrO_2$ amount from 5 to 15 wt%. The enhancement in catalyst performance is attributed to the crystallite of metallic Ni, i.e., the increasing conversion and narrower fluctuation of CH_4 resulted from the decrease in metallic Ni crystallites from 19 to 15 nm as shown in Table 4.5 [39]. The small crystallites of metallic Ni provided the higher number of Ni active sites leading to the strong possibility of CH_4 dissociation.

Furthermore, the small crystallites mean the existence of strong metal–support interaction (SMSI) between Ni and the ($CaO–ZrO_2$)-modified α-Al_2O_3 support leading to the inhibition of carbon–filament formation [40,41].

For the unmodified Ni catalyst (NA), its low CH_4 conversion and wide CH_4 fluctuation are attributed to its large crystallite of metallic Ni (26 nm). The large crystallite resulted in (1) the small amount of Ni active sites (low CH_4 conversion) and (2) the weak metal–support interaction resulting in the formation of filamentous carbon [39,42,44].

It is noticeable that N15(CZ)A provided the higher H_2 yield than the other Ni catalysts, although its CH_4 conversion was comparable to N5(CZ)A and N10(CZ)A. When the $CaO–ZrO_2$ amount rose up to 15 wt%, the formation of calcium zirconate particles offered the cooperative features: (1) the considerable amount of oxygen vacancies existing at the surface of particles, and (2) the continued existence of neck and pores between each the particle. Both the cooperative features significantly enhanced the adsorption of H_2O molecules, and continuously transported the H_2O molecules towards their nearby Ni active sites. The results involved the large dissociation of H_2O molecules leading to the high H_2 yield of N15(CZ)A.

The CO and CO_2 concentration are in connection with water gas shift reaction (WGSR), as shown in Eq. 2.2, occurring on the surface of each the Ni catalyst. N10(CZ)A and N15(CZ)A provided the higher CO concentration than NA and N5(CZ)A due to the difference in the carbon gasification rate on each individual Ni catalyst. Since N10(CZ)A and N15(CZ)A contained the $CaO–ZrO_2$ amount of 10 and 15 wt%, respectively enabling NiO clusters to well disperse on the $CaO–ZrO_2$) particles, the Ni crystallite sizes were decreased to 16 and 15 nm, respectively (Table 4.5). The decreasing Ni crystallite sizes provided the higher Ni active sites facilitating

the reaction of carbon gasification. In comparison to NA and N5(CZ)A, they both have larger Ni crystallites (26 and 19 nm, respectively) implying the smaller number of Ni active sites for the gasification of carbon [22,23].

The results of CO_2 concentration during SMR over each the Ni catalyst were similar to the results of CO concentration—N10(CZ)A and N15(CZ)A provided the higher CO_2 concentration than NA and N5(CZ)A. The higher CO_2 concentration resulted from the more existence of WGSR on N10(CZ)A and N15(CZ)A, compared to NA and N5(CZ)A due to the cooperative effects of the small Ni crystallites and the well–dispersed $CaZrO_3$ particles. Both of the effects led to the high adsorption of H_2O molecules and the continued transportation of H_2O molecules from $CaZrO_3$ particles to Ni active sites. The mechanisms involved the more, continued existence of WGSR on both Ni catalysts.

Fig. 4.35 and 4.36 exhibit the HRTEM images of spent catalysts revealing the existence of metallic Ni, calcium zirconate particles, and α-Al_2O_3 particles. In addition, the HRTEM images indicated the existence of two carbon species resulting in the catalyst deactivation: filamentous and encapsulating carbon.

Notably, the unmodified Ni catalyst (NA) showed the rather large crystallites of metallic Ni and considerable variation in their sizes, compared to the ($CaO–ZrO_2$)-modified Ni catalysts. NA revealed the more existence of both filamentous and encapsulating carbon. The more existence of two carbon species in NA is in agreement with the total amount of carbon in NA (32.6 mg_{carbon}), examined by TGA (Table 4.6). The large amount of carbon in NA originated from the continued growth of filamentous carbon because the large Ni crystallite had the weak metal–support interaction supporting the initial formation of filamentous carbon [22,23,44]. In the case of ($CaO–ZrO_2$)-modified Ni catalysts, the total amount of carbon was

about 32.6, 6.6 and 6.9 mg_{carbon} for the $CaO–ZrO_2$ amount of 5, 10 and 15 wt%, respectively. The results revealed that the loading percentage of $CaO–ZrO_2$ in the Ni catalysts strongly influenced the formation and amount of deposited carbon. Interestingly, N10(CZ)A did not show the existence of encapsulating carbon. Furthermore, N10(CZ)A yielded the lowest total amount of carbon after catalytic testing in SMR for 10 h (6.6 mg) and its percentage of Ni oxidation was the lowest (0.03%) as shown in Table 4.6. The results indicated that N10(CZ)A had the highest stability in SMR for 10 h compared to the other Ni catalysts. The stability of N10(CZ)A resulted from the appropriate size and amount of calcium zirconate particles, leading to the SMSI and then the inhibition of filamentous–carbon formation. Moreover, the SMSI characteristic of N10(CZ)A was confirmed by the large amount of NiO species strongly interacting with α-Al_2O_3 support as shown in its TPR profile (Fig. 4.30).

CHAPTER V

CONCLUSIONS

We concluded our research works following the three-main parts of the experiments.

5.1 Effect of variation in $CaO–ZrO_2$ molar ratio

CaO and ZrO_2 at different mole ratios in the Ni catalysts reacted and formed different phases, i.e., monoclinic solid solution ZrO_2, $CaZr_4O_9$, $CaZrO_3$, and CaO. These phases of $CaO–ZrO_2$ were contained in the Ni catalysts by sequential impregnation and calcination at 600°C. These $CaO–ZrO_2$ phases were dispersed both in pores and on the outside surface of γ-Al_2O_3 and then covered by Ni particles. The surface structure of the Ni catalysts supported on ($CaO–ZrO_2$)-modified γ-Al_2O_3 showed the different and complex results of BET surface area, catalytic activity, and deactivation.

The Ni catalysts with monoclinic solid solution ZrO_2 (NZA) showed the large amount of whisker carbon leading to the unsteady activity. $CaZr_4O_9$ contained in N20CZA contributed to high surface area after reduction, high CH_4 conversion, and low amount of whisker carbon, however, N20CZA provided low H_2 yield due to low water adsorption of $CaZr_4O_9$. $CaZrO_3$ contained in N35CZA, N45CZA and N55CZA showed the existence of whisker carbon. Nevertheless, N55CZA provided the highest H_2 yield due to the high water adsorption on $CaZrO_{3-\delta}$ leading to the high carbon gasification and water gas shift reaction.

$CaZrO_3$ prepared from CaO/ZrO_2 mole ratio at 0.55 played a positive role for steam methane reforming because its oxygen vacancies strongly favored the water adsorption. The amount of oxygen vacancies in $CaZrO_3$ significantly influenced the activity and stability of the supported Ni catalysts. Another useful feature of $CaZrO_3$ is that it is a perovskite oxide prepared at lower temperature (>500 °C) with nanometer size compared to other perovskite-type oxides [45].

However, whisker carbon arising from $CaZrO_3$-modified Ni catalysts is unable to be accepted. Therefore, further experiments on compositions and the conditions of catalyst preparation should be conducted into elimination of whisker carbon and improving CH_4 conversion. In addition, $CaZrO_3$ can be used as a promoter of catalysts for other reactions needing water as a reactant such as water gas shift reaction or steam reforming of hydrocarbons.

5.2 Comparison between co-impregnation and sequential impregnation

The methods of impregnation, i.e. co-impregnation and sequential impregnation, had the significant effects on both the structural characteristics and catalytic reactions of the ($CaO–ZrO_2$)-modified Ni/γ-Al_2O_3 catalyst in steam methane reforming. The stages of catalyst preparation not only directly influenced the forming phases, BET surface area, average pore diameter, and the reduced species, but also affected reaction mechanisms on the modified Ni catalysts leading to the major difference in activity and stability of the prepared Ni catalysts. The co-impregnation-prepared catalyst, NCZA (CI), exhibited the slightly higher activity than the sequential impregnation-prepared catalyst, NCZA (SI). However, the sequential impregnation-prepared catalyst offered the higher stability than the co-impregnation-

prepared catalyst over time on stream of 30 h because it possessed the appropriate structural characteristics for the continuous supply of water from $CaZrO_{3-\delta}$ sites to Ni active sites. It can also suppress the formation of encapsulating carbon, in contrast to NCZA (CI), in which indicated the more existence of encapsulating carbon. As a conclusion, the activity and stability of the ($CaO–ZrO_2$)-modified Ni/γ-Al_2O_3 catalysts in steam methane reforming depended not only on the chemical compositions, but also the structural characteristics to satisfy the requirement for reaction mechanisms in steam methane reforming, which were determined by the methods of preparation.

5.3 Effect of variation in $CaO–ZrO_2$ loading percentage

The variation in loading percentage of CaO-ZrO_2 amount contained in Ni/α-Al_2O_3 catalysts significantly influenced the structural characteristics and thus the performance of the modified Ni catalysts. When the total amount of $CaO–ZrO_2$ in Ni/α-Al_2O_3 catalysts increased from 0 to 15 wt%, the structural characteristics of the modified Ni catalysts were changed to the direction of decreasing in the Ni crystallite sizes, and increasing in the amount of $CaZrO_3$ nanoparticles, the BET surface area, and the amount of reduced bulk NiO. In addition, when the total amount of $CaO–ZrO_2$ increased, the amount of H_2 yield, CO concentration (carbon gasification), and CO_2 concentration (water gas shift reaction) increased, whereas the total amount of carbon deposition decreased. The results of improved structural characteristics are attributed to the more existence of $CaZrO_3$ particles supporting the Ni dispersion uniformly on most $CaZrO_3$ particles. In other words, nanometer–sized Ni metal was deposited on $CaZrO_3$ surface. The interaction between Ni metal and $CaZrO_3$ support was stronger—strong metal–support interaction (SMSI) with the smaller deposited–Ni–

metal sizes. The key features of such co-existence led to the adsorption of H_2O molecules and then transport of H_2O molecules from the large amount of oxygen vacancies on the $CaZrO_3$ surface after reduction stage to the nearest Ni active sites. The more existence of H_2O molecules on the modified Ni catalysts enhanced the existence of reactions of H_2O dissociation, carbon gasification, and water gas shift reaction involving CO_2 gas providing additional H_2 gas. Therefore, the modified Ni catalyst with up to 15 wt% CaO–ZrO_2 provided the high H_2 yield. In the case of the stability of the modified Ni catalysts, when the total amount of CaO–ZrO_2 increased, the small amount of carbon deposition was formed due to the more existence of carbon gasification on their catalyst surface and the SMSI in the catalyst hindering the formation of filamentous carbon. Therefore, the Ni/α-Al_2O_3 catalyst modified with 15 wt% CaO–ZrO_2 and prepared by sequential impregnation proved to provide the higher activity and stability than the unmodified Ni catalyst.

REFERENCES

[1] Joensen, F., and Rostrup-Nielsen, J. R. Conversion of hydrocarbons and alcohols for fuel cells, J Power Sources 105 (2002): 195–201.

[2] Zhang, Q., Li, Y., and Xu, B. Reforming of methane and coaled methane over nanocomposite Ni/ZrO_2 catalyst. Catal. Today 98 (2004): 601–605.

[3] Effendi, A., Zhang, Z., Hellgardt, K., Honda K., and Yoshida T. Steam reforming of a clean model biogas over Ni/Al_2O_3 in fluidized- and fixed-bed reactors. Catal. Today 77 (2002): 181–189.

[4] Takeguchi T., et al. Study on steam reforming of CH_4 and C_2 hydrocarbons and carbon deposition on Ni-YSZ cermets, J Power Sources 112 (2002): 588–595.

[5] Richardson, J. T., Scates, R. M., and Twigg, M. V. X-ray diffraction study of the hydrogen reduction of NiO/α-Al_2O_3 steam reforming catalysts. Appl Catal A 267 (2004): 35–46.

[6] Bartholomew, C. H., and Farrauto, R. J. Fundamentals of industrial catalystic processes. 2nd ed. New Jersey: John Wiley & Sons, Inc; 2006.

[7] Chary, K. V. R., Rao, P. V. R., and Rao V. V. Catalytic functionallites of nickel supported on different polymorphs of alumina. Catal Commun 9 (2008): 886–893.

[8] Takeguchi, T., Furukawa, S.-N., Inoue, M., and Eguchi, K. Autothermal reforming of methane over Ni catalysts supported over CaO-CeO2-ZrO2 solid solution. Appl Catal A 240 (2003): 223–233.

[9] Seo, J. G., Youn, M. H., Jung, J. C., Cho, K. M., Park, S. and Song I. K. Preparation of Ni/Al_2O_3-ZrO_2 catalysts and their application to hydrogen

production by steam reforming of LNG: Effect of ZrO_2 content grafted on Al_2O_3. Catal Today 133 (2008): 130–135.

[10] Dias, K., Garcia, V., and Matos J. Activated carbon supported Ni-Ca: Influence of reaction parameters on activity and stability of catalyst on methane reformation, Fuel 86 (2007): 1337–1344.

[11] Choudhary, V. R., and Rajput, A. M. Simultaneous carbon dioxide and steam reforming of methane to syngas over NiO-CaO catalyst. Ind Eng Chem Res 35 (1996): 3934–3939.

[12] Rostrup-Nielsen, J. R. New aspects of syngas production and use. Catal. Today 63 (2000): 159–164.

[13] Sehested, J. Four challenges for nickel steam-reforming catalysts. Catal. Today 111 (2006): 103–110.

[14] Zhdanov, V. P., and Kasemo, B. Simulations of the reaction kinetics on nanometer supported catalyst particles. Surf. Sci. Rep 39 (2000): 25–104.

[15] Kingery, W.D., Bowen, H. K., and Uhlmann D. R. Introduction to ceramics. 2nd ed. Singapore: John Wiley & Sons, Inc; 1976.

[16] Stubican, V. S., and Ray, S. P. Phase equilibria and ordering in the system ZrO_2-CaO. J Am Ceram Soc 60 (1977): 534–537.

[17] Pawelec B., and Fierro, J. L. G. Handbook of thermal analysis and calorimetry: Applications to inorganic and miscellaneous materials. In: Brown ME, Gallagher PK, editors. Applications of thermal analysis in the preparation of catalysts and in catalysis, Amsterdam: Elsevier B.V.; 2003, p. 119–190.

[18] Seyfi B., Baghalha M., and Kazemian H. Modified $LaCoO_3$ nano-perovskite catalysts for the environmental application of automotive CO oxidation. Chem Eng J 148 (2009): 306–311.

[19] Urasaki, K., Sekine, Y., Kavabe S., Kikuchi E., and Matsukata M. Catalytic activities and coking resistance of Ni/peroskites in steam reforming of methane. Appl Catal A 286 (2005): 23–29.

[20] Youn, M. H., Seo, J. G., Kim, P., and Song, I. K. Role and effect of molybdenum on the performance of Ni-Mo/γ-Al_2O_3 catalysts in the hydrogen production by auto-thermal reforming of ethanol. J Mol Catal A 261 (2007): 276–281.

[21] Seo, J. G., Youn, M. H., and Song, I. K. Hydrogen production by steam reforming of liquefied natural gas (LNG) over nickel catalyst supported on mesoporous alumina prepared by a non-ionic surfactant-templating method. Int J Hydrogen Energy 34 (2009): 1809–1817.

[22] Snoeck, J- W., Froment, G. F., and Fowles M. Kinetic study of the carbon filament formation by methane cracking on a nickel catalyst. J catal 169 (1997):250–262.

[23] Snoeck, J-W., Froment, G. F., and Fowles M. Filamentous carbon formation and gasification: Thermodynamics, driving force, nucleation, and steady-state growth. J catal 169 (1997): 240–249.

[24] Rostrup-Nielsen, J. R., Sehested, J., and Nørskov, J. R. Hydrogen and synthesis gas by steam- and CO_2 reforming. Adv Catal 47 (2002): 65–139.

[25] Hong, J. S., Torre, S. D. D. L., Miyamoto, K., Miyamoto H., and Gao, L. Crystalization of Al_2O_3/ZrO_2 solid solution powders prepared by coprecipitation. Mater Lett 37 (1998): 6–9.

[26] Moreau, S., Gervais, M., and Douy, A. Formation of metastable solid solution in the ZrO_2-rich part of the system ZrO_2–Al_2O_3. Solid State Ionics 101–103 (1997): 625–631.

[27] Dominguez, J. M., Hernandez, J. L., and Sandoval, G. Surface and catalytic properties of Al_2O_3-ZrO_2 solid solutions prepared by sol-gel methods. Appl Catal A 197 (2000): 119–130.

[28] Zeng, H. C., Lin J.., Teo, W. K., Loh, F. C., and Tan, K. L. Surface Ni^{2+} diffusion in sol-gel-derived tetragonal and monoclinic ZrO_2 matrices. J Non-Cryst Solids 181 (1995): 49–57.

[29] Bose, A. C., Ramamoorthy, R. and Ramasamy, S. Formability of metastable tetragonal solid solution in nanocrystalline NiO-ZrO_2 powders. Mater Lett 44 (2000): 203–207.

[30] Pea, M. A., and Fierro, J. L. G. Chemical structures and performance of perovskite oxides. Chem Rev 101 (2001): 1981–2017.

[31] Lertwittayanon, K., Atong, D., Aungkavattana, P., Wasanapiarnpong, T., Wada, S., and Sricharoenchaikul, V. Effect of CaO-ZrO_2 addition to Ni supported on γ-Al_2O_3 by sequential impregnation in steam methane reforming. Int J Hydrogen Energy 35 (2010): 12277-12283.

[32] Snoeck, J. W., Froment, G. F., and Fowles, M. Steam/CO_2 reforming of methane. Carbon filament formation by the Boudouard reaction and gasification by CO_2, by H_2, and by steam: Kinetic study. Ind Eng Chem Res 41 (2002): 4252–4265.

[33] Gozzi, D., Latini, A., and Lazzarini, L. Chemical differentiation of carbon nanotubes in a carbonaceous matrix. Chem Mater 20 (2008): 4126-4134.

[34] Zou, H., Ge, X., and Shen, J. Surface acidity and basicity of γ-Al_2O_3 doped with K^+ and La^{3+} and calcined at elevated temperatures. Thermochim Acta 397 (2003): 81-86.

[35] Lertwittayanon, K., Atong, D., Aungkavattana, P., Wasanapiarnpong, T., and Sricharoenchaikul, V. Steam reforming of methane over ($CaO–ZrO_2$)-modified Ni/γ-Al_2O_3 catalyst prepared by co-impregnation and sequential impregnation. (submitted).

[36] Seo, J. G., Youn, M. H., Park, S., and Song, I. K. Effect of calcination temperature of mesoporous alumina xerogel (AX) supports on hydrogen production by steam reforming of liquefied natural gas natural gas (LNG) over Ni/AX catalysts. Int J Hydrogen Energy 33 (2008): 7427–7434.

[37] Seo, J. G., Youn, M. H., Cho, K. M., Park S., and Song, I. K. Hydrogen production by steam reforming of liquefied natural gas over a nickel catalyst supported on mesoporous alumina xerogel. J Power Sources 173 (2007): 943–949.

[38] Li, G., Hu, L., and Hill, J. M. Comparison of reducibility and stability of alumina–supported Ni catalysts prepared impregnation and co-impregnation. Appl Catal A 301 (2006): 16–24.

[39] Christensen, K. O., Chen, D., Lødeng, R, and Holmen, A. Effect of supports and Ni crystal size on carbon formation and sintering during steam methane reforming. Appl Catal A 314 (2006): 9–22.

[40] Chen, D. et al. Synthesis of carbon nanofibers: effects of Ni crystal size during methane decomposition. J Catal 229 (2005): 82–96.

[41] Rui, W., Xuebin, L., Yanxin, C., Wenzhao L., and Hengyong, X. Effect of metal–support interaction on coking resistance of Rh-based catalysts in CH_4/CO_2 reforming. Chin J Catal 28 (2007): 865–869.

[42] Bengaard, H. S. et al. Steam reforming and graphite formation on Ni catalysts. J Catal 209 (2002): 365–384.

[43] Goula, M. A., Lemonidou, A. A., and Efstathiou, A. M. Characterization of carbonaceous species formed during reforming of CH_4 with CO_2 over Ni/CaO–Al_2O_3 catalysts studied by various transient techniques. J Catal 161 (1996): 626–640.

[44] Jeong, N., and Lee, J. Growth of filamentous carbon by decomposition of ethanol on nickel foam: influence of synthesis conditions and catalytic nanoparticles on growth yield and mechanism. J Catal 260 (2008): 217–226.

[45] Xiulan, C., and Yuan, L. New methods to prepare ultrafine particles of some perovskite-type oxides. Chem Eng J 78 (2000): 205-209.

BIOGRAPHY

Mr. Kowit Lertwittayanon was born in Nakornsrithammarat province on Feb 23, 1976. He received vocational diploma in electronics from Rajamongala Institute of Technology, northbangkok campus. He finished his bachelor's degree in ceramic engineering from Suranaree University of Technology. Later, he worked for 5 years relating to ceramic glazes, binder, and ceramic pigment (stain). He studied in master's degree in ceramic technology at Chulalongkorn University. He has continued studying doctoral degree in materials science at Chulalongkorn University. After he finishes doing his doctoral research work, he will work at Prince of Songkla University and held the position of lecturer in Materials Science and Technology department.

JOURNAL CONTRIBUTIONS

1. Lertwittayanon K.; Atong D.; Aungkavattana P.; Wasanapiarnpong T.; Wada S.; Sricharoenchaikul V. Effect of CaO-ZrO_2 addition to Ni supported on γ-Al_2O_3 by sequential impregnation in steam methane reforming. Int J Hydrogen Energy 35 (2010): 12277-12283. (Impact factor of 2009: 3.945)

2. Lertwittayanon K.; Atong D.; Aungkavattana P.; Wasanapiarnpong T.; Sricharoenchaikul V. Steam reforming of methane over (CaO–ZrO_2)-modified Ni/γ-Al_2O_3 catalyst prepared by co-impregnation and sequential impregnation. (In preparation).

3. Lertwittayanon K.; Atong D.; Aungkavattana P.; Wasanapiarnpong T.; Sricharoenchaikul V. Hydrogen production from steam reforming of methane over ($CaO–ZrO_2$)-modified Ni/α-Al_2O_3 catalyst prepared by sequential impregnation: Effect of $CaO–ZrO_2$ loading percentage. (In preparation).

PROCEEDINGS CONTRIBUTIONS

1. Kowit Lertwittaynon, Shigetaka Wada, Thanakorn Wasanapiarnpong*, Viboon Sricharoenchaikul, Pavadee Aungkavattana, Duangduen Atong. Hydrogen production via steam methane reforming: Promoting effect of $CaO–ZrO_2$ addition to Ni/γ-Al_2O_3. The 2nd Thammasat University International Conference on Chemcial, Environmental and Energy Engineering (TU-ChEEE 2009). 3–4 March 2009, Swissötel Le concorde, Bangkok, Thailand.

2. Kowit Lertwittaynon, Shigetaka Wada, Thanakorn Wasanapiarnpong*, Viboon Sricharoenchaikul, Duangduen Atong, Pavadee Aungkavattana. Temprature–programmed Reduction (TPR) of Ni/$CaO–ZrO_2$/γ-Al_2O_3 catalyst using thermogravimeric analysis (TGA) in H_2 atmosphere. Asian conference on thermal analysis and applications 2009 (ASTA 2009). 17–18 December 2009, Pullman Bangkok King Power, Bangkok, Thailand.

PATENT

1. Kowit Lertwittaynon, Viboon Sricharoenchaikul, Duangduen Atong, Pavadee Aungkavattana, Shigetaka Wada, Thanakorn Wasanapiarnpong. Hydrogen production by steam methane reforming over Ni/$CaO–ZrO_2$/Al_2O_3 catalyst. (Patent pending in Thailand, 2010)